PARTE III:
Compendio de publicaciones.

LISTA DE PUBLICACIONES

ARTÍCULOS
(revistas arbitradas incluidas en el JCR)

Millán, M. S., **Valencia, E.**, Corbalán, M., "3CCD Camera's capability for measuring color differences: experiment in the nearly neutral region", *App. Opt.* **43**(36), 6523-6535 (2004).

Valencia, E., Millán, M. S., "Small color differences in the very pale and dark grayish regions measured by camera", *J. Imaging Sci. Technol.* **49**(6), 605-619 (2005).

Millán, M. S., **Valencia, E.**, "Color image sharpening inspired by human vision models", *App. Opt.* **45**(29), 7684-7697 (2006).

ARTÍCULOS
(revistas arbitradas no incluidas en el JCR y otras de divulgación tecnológica)

Valencia, E., Millán, M. S., "Diferencias de color entre dos ejemplares del atlas de color Munsell", *Opt. Pura y Apl.* **38**(2), 57-65 (2005).

Millán, M. S., Pérez-Cabré, E., Abril, H., **Valencia, E.**, "Evaluación objetiva de la hiperemia de la conjuntiva tarsal superior mediante análisis de imagen. Ensayo preliminar", *Revista Española de Contactología* **12**, 9-15 (2005).

ACTAS EN CONGRESOS

(publicados como capítulos de libros de amplia difusión que alcanzan círculos comerciales)

Millán, M. S., **Valencia, E.**, Corbalán, M. "Evaluation of color differences in nearly neutral Munsell chips by a 3CCD color camera" en *Electronic Imaging (Science and Technology) - Color Imaging IX,* Proc. SPIE - IS&T **5293**, ISBN: 0-8194-5196-7, 169-179, San José de California, USA, 2004.

Millán, M. S., **Valencia, E.** "Camera´s performance in measuring small colour differences in the nearly neutral region" en Proc. IS&T, *CGIV 2004, the 2nd European Conference on Colour in Graphics, Imaging, and Vision*, ISBN: 0-89208-250-X, 469-474, Aachen, Germany, 2004.

Valencia, E., Millán, M. S. "Measuring small color differences in the nearly neutral region by 3CCD camera" en *The Iberoamerican Meeting on Optics and 8th Latin American Meeting on Optics, Lasers, and Their Applications RIAO-OPTILAS 2004,* Proc. SPIE **5622**, ISBN: 0-8194-5575-X, Marcano O., A., Paz, J. L. ed., 1253-1258, Isla Margarita, Venezuela, 2004.

Millán, M. S., **Valencia, E.** "Laplacian filter based on color difference for image enhancement" en *The Iberoamerican Meeting on Optics and 8th Latin American Meeting on Optics, Lasers, and Their Applications RIAO-OPTILAS 2004,* Proc. SPIE **5622**, ISBN: 0-8194-5575-X, Marcano O., A., Paz, J. L. ed., 1259-1264, Isla Margarita, Venezuela, 2004.

Millán, M. S., **Valencia, E.**, Corbalán, M., Gastón, G. "A comparison of a multi-layer silicon sensor camera and a 3CCD camera for measuring small colour differences" en *10th Congress of the International Colour Association – AIC Colour 05,* ISBN: 84-609-5162-6, 299-302, Granada, España, 2005.

Valencia, E., Millán, M. S. "Color referred to a patch of a standard chart: differences between individual collections" en *10th Congress of the International Colour Association – AIC Colour 05,* ISBN: 84-609-5162-6, 1111-1114, Granada, España, 2005.

Millán, M. S., **Valencia, E.** "Color image sharpening using color difference based operators" en *10th Congress of the International Colour Association – AIC Colour 05,* ISBN: 84-609-5162-6, 1055-1058, Granada, España, 2005.

Pérez-Cabré, E., Millán, M. S., Abril, H. C., **Valencia, E.** "Colour image analysis for papillary conjunctivitis assessment" en *10th Congress of the International Colour Association – AIC Colour 05,* ISBN: 84-609-5162-6, 1047-1050, Granada, España, 2005.

Pérez-Cabré, E., Millán, M. S., Abril, H. C., **Valencia, E.** "Image analysis of contact lens grading scales for objective grade assignment of ocular complications" en *Opto-Ireland 2005: Photonic Engineering,* Proc. SPIE **5827**, ISBN: 0-8194-5812-0, Bowe, B. W., Byrne, G., Flanagan, A. J., Glynn, T. J., Magee, J., O'Connor, G. M., O'Dowd, R. F., O'Sullivan, G. D., Sheridan, J. T. ed., 418-427, Dublin, Irlanda, 2005.

Millán, M. S., **Valencia, E.** "Image sharpening based on spatiochromatic properties of the human vision system" en Proc. IS&T, *CGIV-2006, the 3rd European Conference on Colour in Graphics, Imaging, and Vision*, ISBN: 0-89208-262-3, Leeds, United Kingdom, 2006.

Valencia, E., Millán, M. S. "Color image analysis of the optic disc to assist diagnosis of glaucoma risk and evolution" en Proc. IS&T, *CGIV 2006, the 3rd European Conference on Colour in Graphics, Imaging, and Vision*, ISBN: 0-89208-262-3, Leeds, United Kingdom, 2006.

Valencia, E., Millán, M. S., Kotynski, R. "Cup to disc ratio of the optic disc by image analysis to assist diagnosis of glaucoma risk and evolution" en *5th. International Workshop on Information Optics,* AIP **CP860**, ISBN: 978-0-7354-0356-7, Cristóbal, G., Javidi, B., Vallmitjama, S. ed., 290-299, Toledo, España, 2006.

ACTAS EN CONGRESOS NACIONALES

(publicados como capítulos de libros de amplia difusión que alcanzan círculos comerciales)

Millán, M. S., **Valencia, E.**, Corbalán, M. "Análisis comparado de las diferencias de color en muestras Munsell casi neutras medidas con una cámara 3CCD" en *7 Reunion Nacional de Óptica - 7RNO,* ISBN: 84-8102-348-5, Santander, España, 2003.

Millán, M. S., **Valencia, E.**, Pérez-Cabré, E., Abril, H., Gil, M. A. "Procesado de imagen en color con aplicaciones a la imagen oftálmica" en *8 Reunión Nacional de Óptica - 8RNO,* Alicante, España, 2006.

3CCD Camera's capability for measuring color differences: experiment in the nearly neutral region

App. Opt. **43**(36), 6523-6535 (2004).

3CCD camera's capability for measuring color differences: experiment in the nearly neutral region

María S. Millán, Edison Valencia, and Montse Corbalán

A method to assess the discrimination capability of a camera to measure small color differences is proposed. The method helps to fix the working conditions of the camera and analyzes the reliability of the measurements through comparison with a reference instrument. Attention is paid to the camera's performance in the nearly neutral region of color space. The color differences are calculated using the Commission Internationale de l'Eclairage $L^*a^*b^*$ (CIELAB) ΔE_{ab}^* and CIE 2000 color-difference formula metrics. The Sony DX-9100P 3CCD camera results are very close to those obtained by the Photo Research PR-715 spectroradiometer. Their absolute discrepancy is lower than the suprathreshold of visual discrimination (0.887 CIELAB unit).

OCIS codes: 040.0040, 040.1490, 120.5240, 330.0030, 330.1710.

1. Introduction

During the past decade, color-imaging devices such as cameras and scanners have achieved an increasing relevance in color data acquisition of spatially variant scenes. These devices, as well as display and hard-copy systems, are based on color management and technology. A color camera can be a component integrated in a versatile computer-vision system, not necessarily complex or too expensive, that permits a great variety of tasks in image featuring and inspection with a good trade-off between image quality and measurement capability of color. Computer-vision systems are easily adaptable to a large number of products and configurations, and hereby they are highly appreciated for industrial applications.

Several techniques for camera characterization orientated to colorimetric purposes have already been described in the literature.[1–4] They focus on two aspects: the three spectral-sensitivity functions of the sensors for the red-green-blue (RGB) channels, and a linearization function that depends on the stimulus intensity. A camera model widely used over a variety of computer-vision systems[1–3] considers that, given the sensor, all nonlinear behavior is independent of wavelength. The three sensor response functions can be seen as a set of color-scanning filters for which a measure of goodness, in terms of similarity to the human color-matching functions, can be determined.[5]

The camera characterization allows one to predict an acceptable acquisition and record the color content of the image with enough covering of luminance, hue, and chroma scales. The RGB color components provided by a camera lead to a device-dependent representation of color. For this reason, in color management and in colorimetric applications, a transformation that defines a mapping between the camera RGB signals and a device-independent representation, such as standard Commission Internationale de l'Eclairage (CIE) 1931 *XYZ*, is necessary. There is some previous work concerning a linear transformation from the R, G, B components given by the camera to the *X*, *Y*, *Z* tristimulus values.[6–8] Hong *et al.*[4] carried out a study for the colorimetric characterization of digital cameras based on a polynomial modeling. Once the *XYZ* tristimulus values are obtained, the Commission Internationale de l'Eclairage $L^*a^*b^*$ (CIELAB) coordinates, as well as the values of hue h_{ab} and chroma C_{ab}^*, can be derived from them.[9,10]

As far as we know, less effort has been devoted to exploit the discrimination capability of color cameras in the measurement of color differences. A possible reason could be the existence of a number of instruments (colorimeters, spectrophotometers, spectrora-

M. S. Millán (millan@oo.upc.es) and E. Valencia (edison@oo.upc.es) are with Departamento de Optica y Optometría, 37 Violinista Vellsolà, Universidad Politécnica de Cataluña, 08222 Terrassa Barcelona, Spain. M. Corbalán is with Departamento de Ingeniería Electrónica, Universidad Politecnica de Cataluña, Manresa Barcelona 08240, Spain.

Received 15 December 2003; revised manuscript received 4 June 2004; accepted 22 July 2004.

0003-6935/04/366523-13$15.00/0

diometers) capable of measuring highly precise color differences. These instruments, however, measure color in an integration area of the sample with limited flexibility in configuration, dimensions, and sample scanning. These conditions cannot be easily modified in general, even when using expensive and sophisticated instruments.

In this paper, we deal with the measurement of color differences by a 3CCD camera. We propose a method to assess the discrimination capability of a camera to measure small color differences. We also are concerned with the reliability of the camera in comparison with a reference instrument (a spectroradiometer). We focus our attention on the camera's performance in the nearly neutral region of color space for three reasons. First, it represents a challenge for the instrument, since the nearly neutral colors entail a similar stimulation of the three (red, green, and blue) sensitive channels of the camera, and the differences between these colors involve small variations on a high nearly constant background signal. Second, most of the colors contained in real and natural scenes have low chroma, and, third, the nearly neutral color region draws industrial attention, particularly related to materials for painting, clothing, or decorating.

The method proposed has two stages. In the first stage, we determine the appropriate working conditions of the acquisition system and try to adjust the gain and offset controls to obtain the camera response closest to the reference-instrument response in the CIELAB system for an achromatic grade. In the second stage of the method, we select a set of samples of very pale colors from the nearly neutral matte Munsell collection, regularly distributed in the hue circle. A large number of color differences between pairs of nearest-neighbor chips are separately evaluated by both the camera and the reference instrument according to the CIELAB[9,10] and the more recent CIE 2000 color-difference formula (CIEDE-2000)[11] metrics, which includes a term to improve performance of low-chroma colors.[12] The comparison of the results gives the discrepancy between the two systems. This discrepancy is used to test the reliability of the camera's performance.

We have applied the method to the Sony DX-9100P 3CCD camera that is compared with the Photo Research PR-715 spectroradiometer as a reference instrument. The results are discussed and the conclusions outlined in the last sections of this paper.

2. Method

The method described in this section explores the discrimination capability of a color camera in order to determine if it can be used to measure small color differences with a certain reliability. The camera performance is compared with a reference instrument, a spectroradiometer, that is assumed to be calibrated and high quality. The method has two stages. In the first stage, we determine the appropriate working conditions of the acquisition system. In the second stage, we evaluate the discrepancy in the small color differences measured by the camera in comparison to the same color differences measured by a reference instrument. The test consists of an assortment of Munsell chips distributed in the hue circle and belonging to the nearly neutral region.

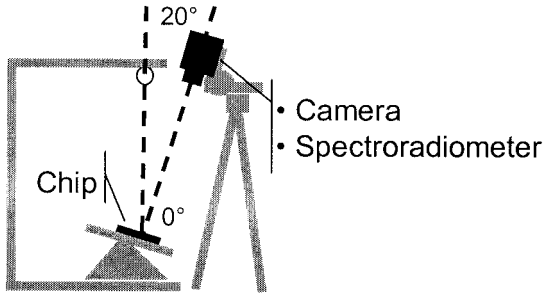

Fig. 1. Scheme of the booth and the illumination–observation geometry used to measure with either the camera or the spectroradiometer.

A. Working Conditions of the Acquisition System

A camera-based color-imaging acquisition system consists of a camera (often 3CCD), a frame grabber, a personal computer, and a given lighting–viewing configuration. We compare the camera and the reference instrument in the same illumination–observation conditions (Fig. 1): We use an observation booth with a given illuminating light source (fluorescent lamps to build a D65 simulator are often used in booths) and a given illumination–observation geometry for which the scene is captured away from specular reflections. The field of view of the camera is fully occupied by a single Munsell matte chip ($\approx$3.5 cm^2). When using the standard 45° illumination, some image artifacts or noise caused by a shading effect on the rough surface are observed. Since the samples are matte, the choice of the illumination geometry is not critical. Thus to reduce noise, we consider a 20° illumination from the surface normal for all the measurements. Regarding the observation, the camera is placed in front of the sample, in the direction perpendicular to the sample surface. A frontal viewing is preferable to a slant viewing because it reduces focus errors and geometrical distortions produced by perspective that could be important for future applications to spatially variant images. Normal observation is also considered for the reference instrument.

The characterization of a 3CCD camera requires the spectral sensitivity curves of the sensors. There are various methods described in the literature to estimate them. A conceptually simple method is based on stimulating the camera with very narrow-band illumination produced by a monochrometer.[2] The sophisticated equipment necessary to implement this technique motivated several researchers to obtain other procedures based on the camera responses to a number of inputs with known spectral distribution. In this line, the characterization method proposed by Barnard and Funt[3] is based on an optimized procedure that jointly fits the small nonlinearity in the camera response with the sensor response func-

tions. The three spectral-sensitivity functions are a set of color-scanning filters for which the measure of goodness, ν, defined in Ref. 5, can be determined. The ν factor is used to characterize input devices, such as cameras or scanners, and indicates the similarity of the set of the device spectral sensitivities to human color-matching functions so that $\nu \approx 1$ means a perfect fit. According to Berns and Reiman,[13] values of the ν factor >0.9 are desirable for colorimetric purposes. Relatively good results can be obtained, however, using input devices with lower values of the ν factor in color-management processes.[13]

Taking into account the spectral-response curves of the camera sensors, Simpson and Jansen[7] described a procedure to calculate the 3×3 matrix coefficients of the linear transformation to obtain the *XYZ* tristimulus values from the RGB components given by the camera for each pixel. We have used this procedure in previous works,[8,14] but taking into account the particular spectral radiant power distribution of the illuminating light source in the calculation of the coefficients of the linear transformation. Once the linear transformation is defined for a given camera and a given light source, the tristimulus values *XYZ* of a uniform color sample can be derived from the RGB components provided by the camera. The CIELAB coordinates $L^*a^*b^*$ (CIE 1976) can be calculated using the standard formulas given in Refs. 9 and 10. Other useful magnitudes of the CIELAB system are chroma C_{ab}^* and hue h_{ab}, which correspond to the polar coordinates of this cylindrical representation system, for which the luminance L^* gives the axis.

In the next step, and provided the camera is used with its gamma function disabled, we analyze their linearity over the operating range and try to obtain the most linear response by adjusting the gain and offset controls. This analysis is carried out, for instance, by stimulating the camera with a scale of achromatic stimuli. Barnard and Funt[3] and Vora *et al.*[1] consider this linearization as a function associated with each RGB channel. However, in our method, we propose to measure the $L^*a^*b^*$ coordinates of an achromatic scale of Munsell neutral matte chips, with variant luminance (Munsell value), by the reference instrument and, separately, by the camera. A representation of L^* measured by each instrument versus sample luminance allows the comparison between both instrument's performances and thereby to adjust the camera linearized response to that of the reference instrument as much as possible.

The analysis of either a^*, b^* or C_{ab}^*, h_{ab} values measured by both instruments for the neutral scale of chips is also interesting. Provided the set of neutral chips and the reference instrument's response are consistent with achromacy, the values of a^*, b^* and C_{ab}^* have to be very close to zero. This statement can also be used to compare the camera with the reference instrument. Following these two conditions, gain and offset ranges of values can be suitably adjusted, and the general working conditions of the acquisition system fixed.

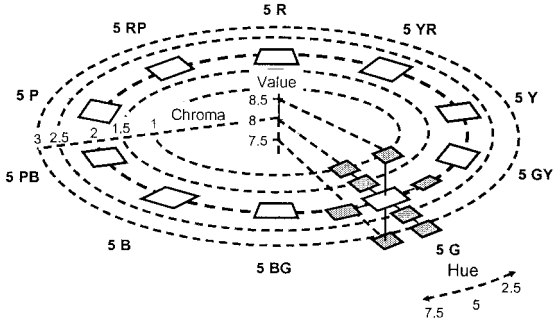

Fig. 2. Scheme of the selection of the 90 Munsell matte chips that comprise the test. They are grouped in 10 subsets regularly distributed on the hue circle. Each subset consists of a group center and its closest neighbors that differ ± 2.5 in hue, ± 0.5 in value, and ± 0.5 and ± 1.0 in chroma from the center.

B. Color-Discrimination Capability of the Camera

Standard color targets consisting of an assortment of color patches are commonly applied to camera characterization. The Gretag Macbeth color-checker color rendition chart[15] is one of the most utilized, although it consists of only 24 patches. In some cases,[13] as we will also do in the second stage of the method, a custom characterization target consisting of a larger number of patches is designed and applied.

We select a set of matte samples from the Nearly Neutral Munsell Collection and the Munsell Book of Colors, regularly distributed in the hue circle (10 Munsell hue) with a low value of chroma (2) and a high value of value (8). The set of samples generated in this way belong to the very pale color region. Each one of the selected chips is compared with its nearest neighbors of the Munsell color system. Taking into account the Munsell specification of hue value and chroma, we consider variations of ± 2.5 hue, ± 0.5 value, ± 0.5 chroma, and ± 1.0 chroma around each selected chip. Figure 2 contains a sketch of the distribution in the Munsell system of the sample set that we use to test the camera. The sketch represents the selected samples in the circle of hue. Each selected sample is the center of the group constituted by it with its neighbors (only shown for the group centered at 5B 8/2 in Fig. 2). According to this, our test in the second stage of the method consists of 90 Munsell matte color chips.

The absolute measurement of color by the camera may be compared with the external reference provided by the reference instrument. For instance, the CIELAB coordinates of a given chip, separately obtained by the camera and the reference instrument in the same conditions, could be compared, and this comparison would be extended to the total amount of test samples.

Apart from absolute measurements, we are more interested in the relative measurement of color that lets us estimate color differences. The uncertainty intervals of the color differences measured by the camera and by the reference instrument will be calculated before comparing the measurement results. All the color differences between the group center and

its neighbors are evaluated in pairs. The discrepancy between the results obtained by the camera and by a reference instrument can be seen as the error associated with the camera. This is a way to test the reliability of the camera's performance in comparison with that of the reference instrument. The best camera performance would correspond to a discrepancy equal to zero or, equivalently, within the uncertainty interval of the reference-instrument measurement.

The experiment just described allows us to obtain additional information about the uniformity of the camera response along different hue regions. Further information relating to the camera response to luminance variations only, or to chroma variations only, is found as well.

A variety of formulas can be considered to evaluate color differences. In this work, we use two of them: the CIELAB classical formula for color differences ΔE_{ab}^*,

$$\Delta E_{ab}^* = [(\Delta L^*)^2 + (\Delta a^*)^2 + (\Delta b^*)^2]^{1/2}, \qquad (1)$$

which is widely known and a reference for other metrics,[9,10] and the CIEDE2000 formula ΔE_{00}, recently proposed by Luo *et al.*[11] and recommended by CIE.

3. Experimental Application

We apply the method described in Section 2 to the characterization of the discrimination capability of a 3CCD camera. The image-acquisition system of our study consists of the following components:

- A Sony DX-9100P 3CCD camera.
- A Matrox Meteor II M/C (8 bits) frame grabber. The frame grabber is integrated in a personal computer that is used for subsequent calculations.
- A VeriVide CAC 120H4 observation booth with a D65 daylight simulator given by a F40/T12 fluorescent lamp. We measured its spectral power distribution, and its correlated color temperature was 6438 K (10° observer).

The color camera is configured so that the gamma function is equal to 1.0. The white balance is automatically adjusted to the color temperature of 6500 K (daylight D65). We totally occlude the camera-lens aperture for the black reference and capture a standard reflectance plate (Photo Research RS-3) for the white reference. The reflectance spectral distribution of the plate is nearly constant and equal to 1 (its calibration did not exceed ±0.6% versus the values of a reference-calibrating source, within 380–780 nm). The gain control was in manual position, at 0-dB level. The camera aperture remained fixed ($f/\# = 4$) during the rest of the experience.

The frame grabber captures an image of 640 × 780 pixel size for each single Munsell chip imaged by the camera lens. However, we only analyze a central window. In this way, we take advantage of the optimal performance of the camera lens around its optical axis, and we also avoid effects from possible nonuniformities of illumination. We initially selected two squared windows of 500 × 500 and 300 × 300 pixel size in images captured by the camera of uniform color samples. Since the mean RGB values and the standard deviations hardly varied from using either one window or the other, we eventually decided to use the smallest one, of 300 × 300 pixel size. The Matrox Meteor II M/C (8 bits) frame grabber digitized the analogic signals provided by the camera into 256 gray levels (digital values) for each R, G, and B channel. The gain and offset values have to be suitably fixed before acquiring images. In Subsection 2.A, we explain the procedure followed to this end.

For image acquisition, we used a VeriVide booth with the illumination provided by its D65 daylight simulator and the illumination–observation geometry stated in Section 2 (Fig. 1) either for the camera or the reference instrument (spectroradiometer). Inside the booth, the illumination is almost uniform, and we verified this characteristic using a luxometer. However, this is not critical in this particular work because the samples we analyze are small enough to consider that the illumination is uniform throughout the sample (the Munsell matte chip area is ~3.5 cm^2). The illumination is approximately 20° from the normal of the sample surface, but within the booth, it must be taken into account that both direct and diffuse light is present. Nevertheless, these geometrical considerations have little importance when one is measuring diffuse materials such as the very matte surface of the Munsell chips.

In this work, the camera's performance is compared with a calibrated spectroradiometer as the reference instrument; both work with the same illumination–observation geometry (replacing the camera by the spectroradiometer in the setup of Fig. 1). We use the Photo Research PR-715 spectroradiometer. The spectroradiometer measured the central area of a Munsell chip with 1° aperture or field coverage. We have used this spectroradiometer to measure several things in this work: the spectral power distribution and correlated color temperature of the D65 simulator of the booth, the spectral sensitivities of the 3CCD camera, and the diffuse spectral reflectance and triestimulus values of the Munsell chips.

A. Camera-Independent Representation of Color

In the camera initialization, the gain and offset values have to be fixed so that the frame grabber converts the analogical signal of the camera into the RGB digital values in the 8-bit range of 0 to 255. Initially, one tries setting some combination out of the four possible combinations where the gain and the offset take the extreme values of the range, i.e., either 0 or 255. We studied the RGB responses of the camera versus a gray scale of 31 Munsell matte neutral chips (within the value range $V = 2$ up to $V = 9.5$) for these four cases (Fig. 3). To complete the range of the gray scale, we occluded totally the camera aperture (that stands for $V = 0$), and then we captured the reference white, the standard RS-3

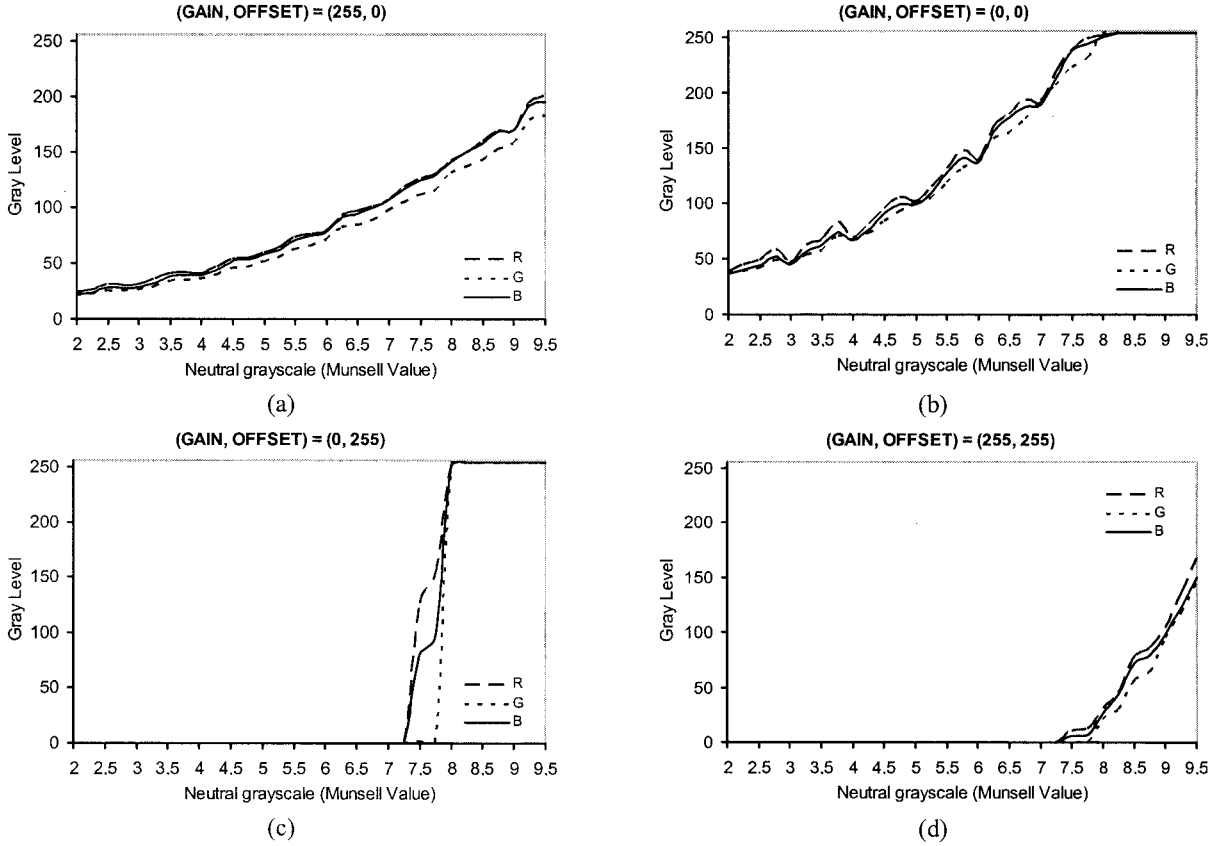

Fig. 3. RGB values provided by the camera when capturing a scale of gray samples with (gain, offset) = {(255, 0), (0, 0), (0, 255), (255, 255)}. A D65 simulator was the light source. The gray scale consisted of a gradation of Munsell matte neutral chips (from value of 2 up to 9.5). Value of 0 corresponds to totally occluding the camera lens, and value of 10 corresponds to capturing the reference white.

plate (that stands for $V = 10$). Since the camera response that takes profit from its maximum dynamic range with the minimum alteration in the signal is usually sought, we selected gain (255) and offset (0), which correspond to the RGB responses graphed in Fig. 3(a). Note in Fig. 3(a) that even when setting offset equal to 0, nonzero RGB signals are obtained when the camera aperture is totally closed, which means there is a constant background or a noise introduced by the camera. The values gain equal to 0 and offset equal to 0 [Fig. 3(b)] are not preferable to the former gain (255) and offset (0) [Fig. 3(a)] because they lead to a saturation of the sensor for high luminances (our region of interest), and, in addition, the constant background is nearly doubled.

We measured the RGB responsivity values of the Sony DX-9100P camera for some values of gain (255, 128) and offset (0, 32, 64) around the initially selected values of gain (255) and offset (0). We applied the classical technique based on stimulating the camera with very narrow-band illumination produced by a monochrometer. Figure 4 shows the graphs of the three spectral responses of the camera measured for the six combinations of gain and offset values. Considering each set of three responsivity functions as a set of color-scanning filters, we calculate the measure of goodness given by factor ν.[5] From Fig. 4, a value $\nu > 0.9$ is reached by the pairs (gain, offset) = {(128, 32), (255, 32)}. On the other hand, the pair (gain, offset) = (255, 0) obtains the lowest value $\nu = 0.8208$ among the six pairs studied. It can be seen that offset variations have greater influence in the RGB responsitivity functions, and hence in their factor ν, than gain variations do. We eventually consider that the best result is obtained for (gain, offset) = (255, 32). In this case, the shape of the R sensitivity function is slightly smoother than for the pair (128, 32).

From the different sensitivities presented in Fig. 4, the spectral power distribution of the D65 simulator, the standard observer responses, and the coefficients of the linear transformations that relate the RGB values obtained by the camera with a given (gain, offset) to the *XYZ* tristimulus values can be calculated. We followed the procedure described in Refs. 6 and 7. For instance, for (gain, offset) = (255, 32), we obtained the linear transform

$$\begin{pmatrix} X \\ Y \\ Z \end{pmatrix} = \begin{bmatrix} 2.080 & 0.246 & 0.359 \\ 1.239 & 1.059 & 0.094 \\ 0.065 & -0.119 & 2.130 \end{bmatrix} \times \begin{pmatrix} R \\ G \\ B \end{pmatrix}. \quad (2)$$

From the *XYZ* values, the CIELAB coordinates $L^*a^*b^*$ are calculated using the CIE 1976 formula.[9,10] As the white reference for this calculation, we

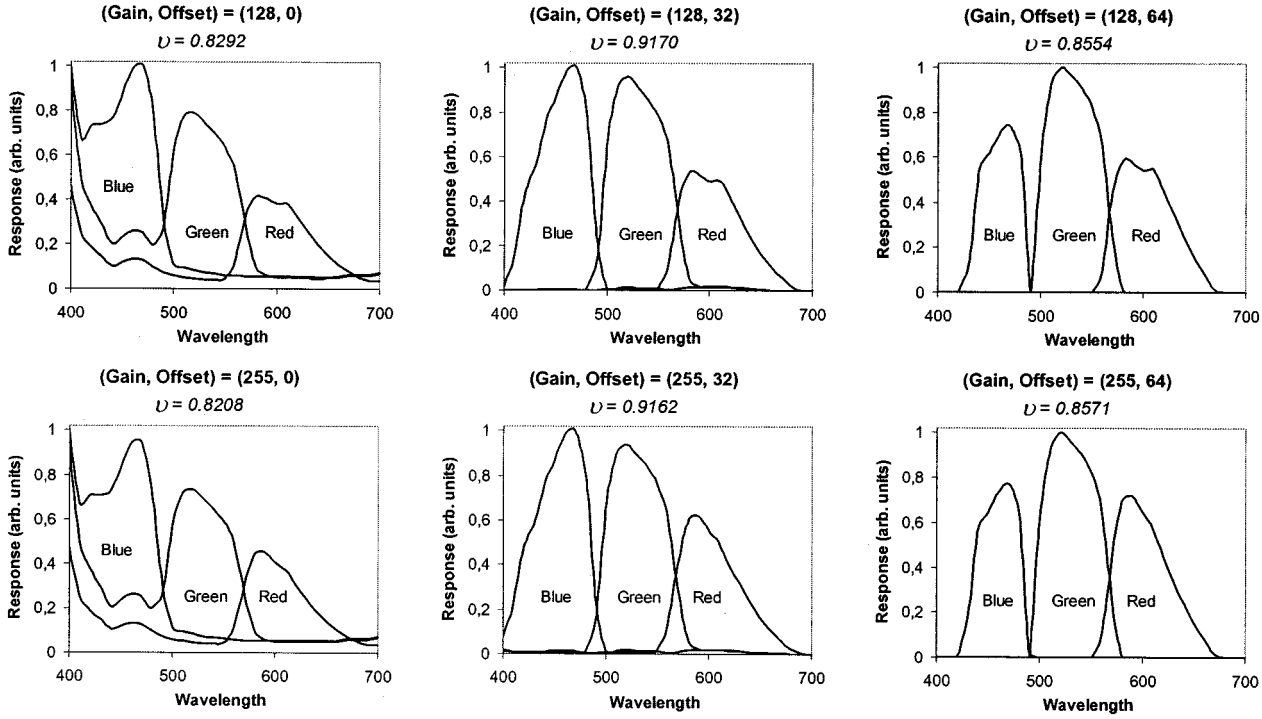

Fig. 4. Spectral responsivities of the Sony DX-9100P camera measured for different (gain, offset) values.

used the X_n, Y_n, and Z_n obtained for the Photo-Research RS-3 standard reflectance plate.

B. Influence of Gain and Offset in the CIELAB Coordinates of a Neutral Scale

To confirm the selection of the camera working conditions, we develop a deeper study of how the camera response, in terms of color representation, is jointly influenced by the gain and the offset controls when it captures the samples of the neutral scale used in Subsection 3.A. This study will allow us to carry out a comparison between the colorimetric data obtained by the camera with those obtained by the reference instrument (spectroradiometer). We apply the linear transformation to the RGB values captured by the camera with a given (gain, offset) to obtain the *XYZ*, and then we apply the CIE 1976 formula to calculate the CIELAB coordinates. Several values of gain (128, 255) and offset (0, 32, 64) have been combined to capture the gray samples with the camera. Figure 5 shows graphs of the luminance L^* versus the Munsell value for the two instruments. All the curves reveal camera responses quite close to the spectroradiometer response in the medium and bright regions of the gray scale. The curves look rather linear, and this fact is in correspondence with the nearly linear scale of the considered neutral Munsell chips. Among the camera-response graphs represented in Fig. 5, the group corresponding to offset (32) and gain (128, 255) is really very close to the spectroradiometer response within the whole gray scale.

On the other hand, if we consider the chromatic plane defined by the a^*, b^* coordinates, all the gray samples (Munsell neutral chips from $V = 2$ to $V = 9.5$) should be represented by points near the origin. As Fig. 6 shows, this is fairly accomplished for the measurements obtained by the spectroradiometer, except for two gray samples with the highest Munsell values. There is a small error or a slight deviation toward the yellow region, which could be due to the samples or to the spectroradiometer. We include in Fig. 6 the group of graphs corresponding to the camera capturing with (gain, offset) = {(255, 0), (255, 32), (128, 32)}. These measurements obtained by the camera tend to deviate toward the red or red-orange zone. The graph corresponding to (gain, offset) =

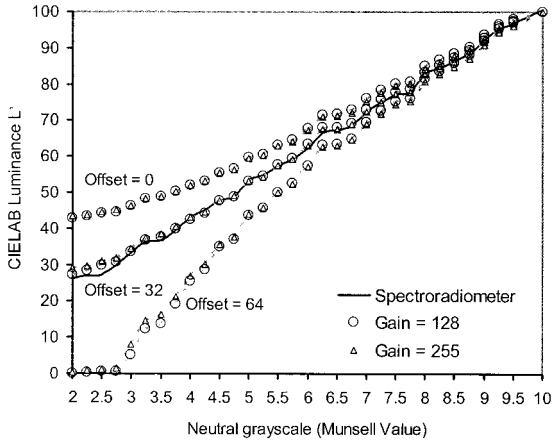

Fig. 5. CIELAB luminance L^* versus the Munsell value of the neutral chips of the gray scale. The measurement of L^* was obtained by a spectroradiometer (in solid curve) and by the camera with different values of gain and offset.

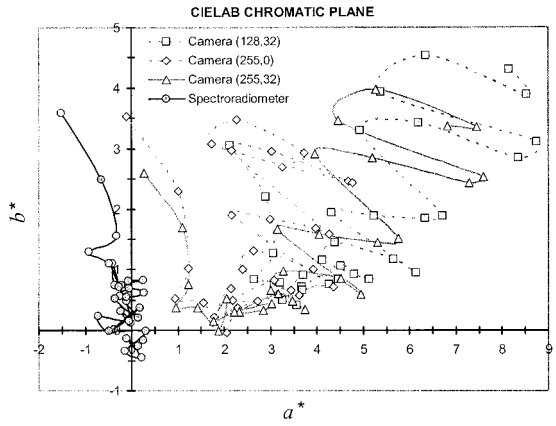

Fig. 6. CIELAB chromatic plane showing the a^*, b^* coordinates of the gray samples measured by the spectroradiometer and by the camera with (gain, offset) = {(128, 32), (255, 0), (255, 32)}.

(255, 32) falls approximately between the other two. If we compare the results of Figs. 5 and 6, we see that, with respect to L^*, the pair (gain, offset) = (255, 32) is better than (gain, offset) = (255, 0). But, looking at the chromaticity plane, we conclude the opposite, i.e., the pair (gain, offset) = (255, 0) obtains slightly better results than the pair (gain, offset) = (255, 32).

Figure 7 takes information from Figs. 5 and 6 and shows the luminance L^* versus the chromaticity $C_{ab}{}^*$. It can be seen (marked by arrows in Fig. 7) that, when using the camera, the pair (gain, offset) = (255, 0) gives lower chromaticity values for the neutral scale, but, on the other hand, it also has less covering of luminance than the pairs (gain, offset) = {(255, 32), (128, 32)}. Again, the graph corresponding to (gain, offset) = (255, 32) is between the other two obtained for the camera. In addition, looking at the area of interest of the pale color region (with Munsell values from $V = 7$ to $V = 9$), we see that the curves corresponding to (gain, offset) = {(255, 32), (255, 0)} appear very close in this region in Fig. 7 and, in fact, also in Fig. 5. For the reasons concerning the results shown in Figs. 5–7, the capturing condition given by (gain, offset) = (255, 32) seems to be preferable, although some tolerance in the gain value can be accepted. For the next experiment, we still consider two offset values (0 and 32) and, in consequence, two capturing conditions (gain, offset) = {(255, 32), (255, 0)} are studied. They lead to interesting comparisons of the results in the measurement of small color differences.

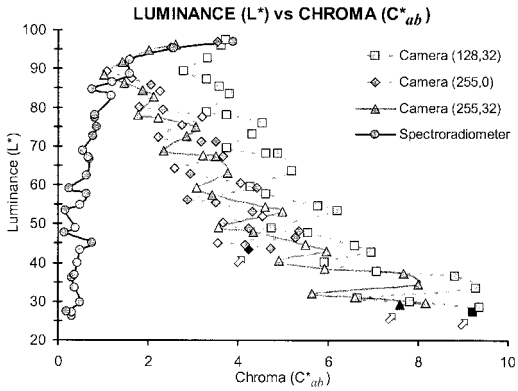

Fig. 7. CIELAB luminance L^* versus chroma $C_{ab}{}^*$ of the gray scale measured by the spectroradiometer and the camera under the capturing conditions of Fig. 6.

C. Color Measurement and Color Difference

To apply the second stage of the method, we have measured the CIELAB coordinates, chroma $C_{ab}{}^*$, and hue h_{ab} of the test of 100 Munsell color chips (Fig. 2) by the spectroradiometer and by the camera with two capturing conditions: (gain, offset) = {(255, 32), (255, 0)}. We present in Fig. 8 the results obtained for the groups centered at (a) 5YR8/2, (b) 5G8/2, (c) 5B8/2, and (d) 5P8/2, as representative of the rest of groups. For a given group, three figures are presented (from left to right): first (left), the a^*, b^* chromatic plane with the points corresponding to the Munsell neighbor chips that represent chroma or hue variations with respect to the group center; second (center), the luminance L^* versus $C_{ab}{}^*$ figure, with the points corresponding to the neighbor chips that represent value or chroma variations with respect to the group center; third (right), the luminance L^* versus $C_{ab}{}^*$ figure, with the points corresponding to the neighbor chips that represent hue variations with respect to the group center.

From the diagrams of Fig. 8, one can appreciate that, in general, the values measured by the spectroradiometer do not coincide with those measured by the camera, but, on the other hand, there is a certain similarity between their relative point positions. Thus the chroma variations in the Munsell system appear radially ordered in the a^*, b^* chromatic plane, whereas the Munsell hue variations appear with a predominantly angular distribution in the same plane. As expected for both devices (camera and spectroradiometer) in the central $L^*C_{ab}{}^*$ diagrams, Munsell chroma variations are nearly constant in luminance, whereas Munsell value variations are nearly constant in chroma and give rise only to predominant luminance variations. Munsell hue variations should not be appreciated in the right-handed $L^*C_{ab}{}^*$ diagrams, so a single point representing the group center and its corresponding one-step-away-in-hue neighbors are expected in each diagram. In fact, points in these right-handed $L^*C_{ab}{}^*$ diagrams (in Fig. 8) appear quite close in general. In addition to the results shown in Fig. 8 for four groups, we have verified the uniformity of the camera response along different hue regions, for luminance variations only, and for chroma variations only.

If we compare the spectroradiometer's performance with the results obtained by the camera for the two capturing conditions (gain, offset) = {(255, 32), (255, 0)} in Fig. 8, it can be said that both capturing conditions lead to rather similar results, and neither of them appears as clearly advantageous.

The results just presented allow us to roughly describe the camera's performance in the absolute mea-

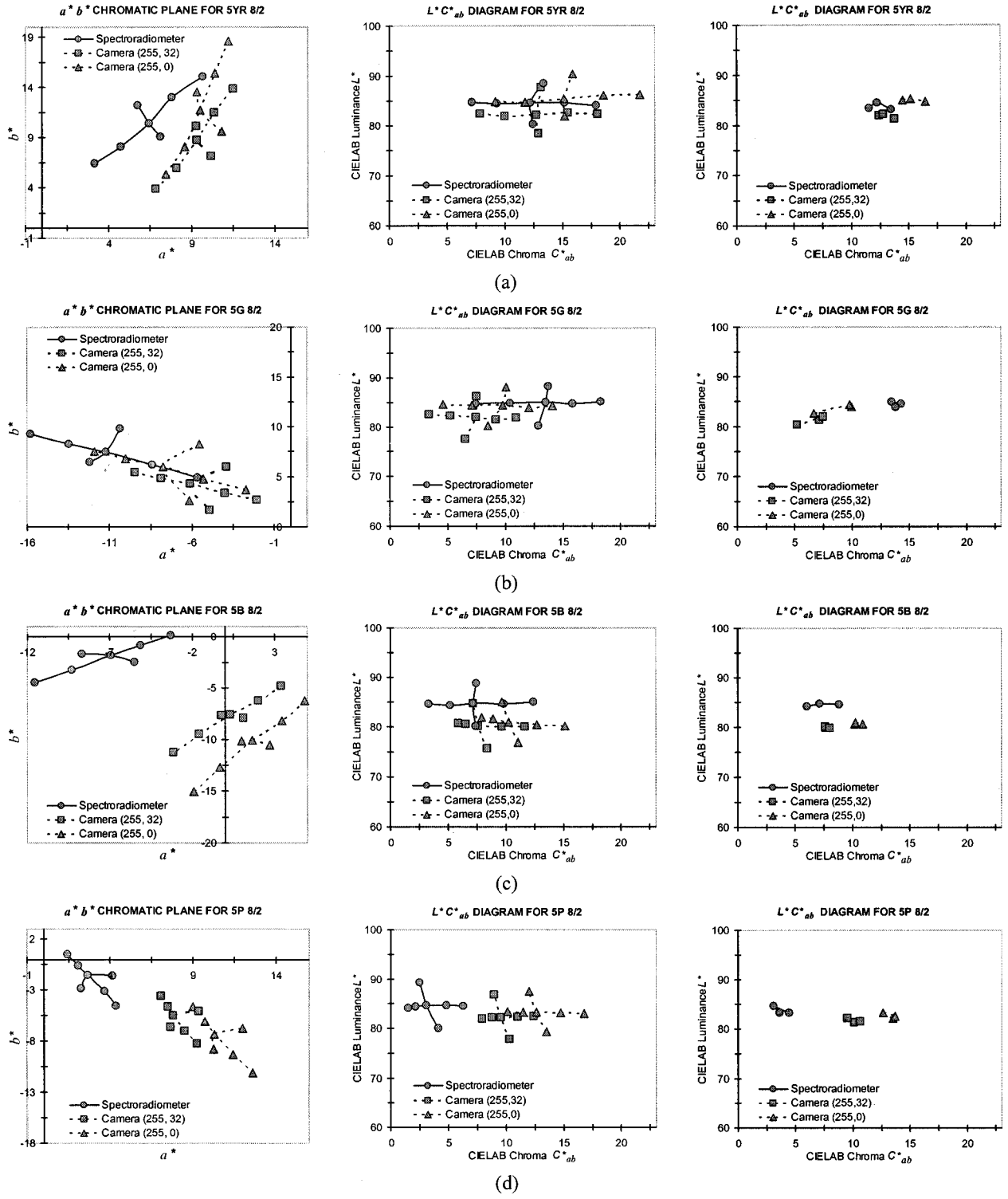

Fig. 8. CIELAB L^*, a^*, b^*, $C_{ab}{}^*$ for four groups of Munsell chips (Fig. 2) centered at (a) 5YR 8/2, (b) 5G 8/2, (c) 5B 8/2, and (d) 5P 8/2, measured by the spectroradiometer and by the camera with two capturing conditions (gain, offset) = {(255, 0), (255, 32)}. On the left, Munsell chroma and hue variations with respect to the group center are represented on the chromatic a^*b^* plane. In the center, Munsell value and chroma variations are represented on a $L^*C_{ab}{}^*$ diagram. On the right, Munsell hue variations are represented on a $L^*C_{ab}{}^*$ diagram.

surement of color. But they do not give enough information about the capability of the camera to obtain relative measurements of color. We are now interested in exploring the discrimination capability of the camera and its reliability in the measurement of small differences between very pale colors. There are a number of industrial tasks for which the absolute measurement of color is not so important, and,

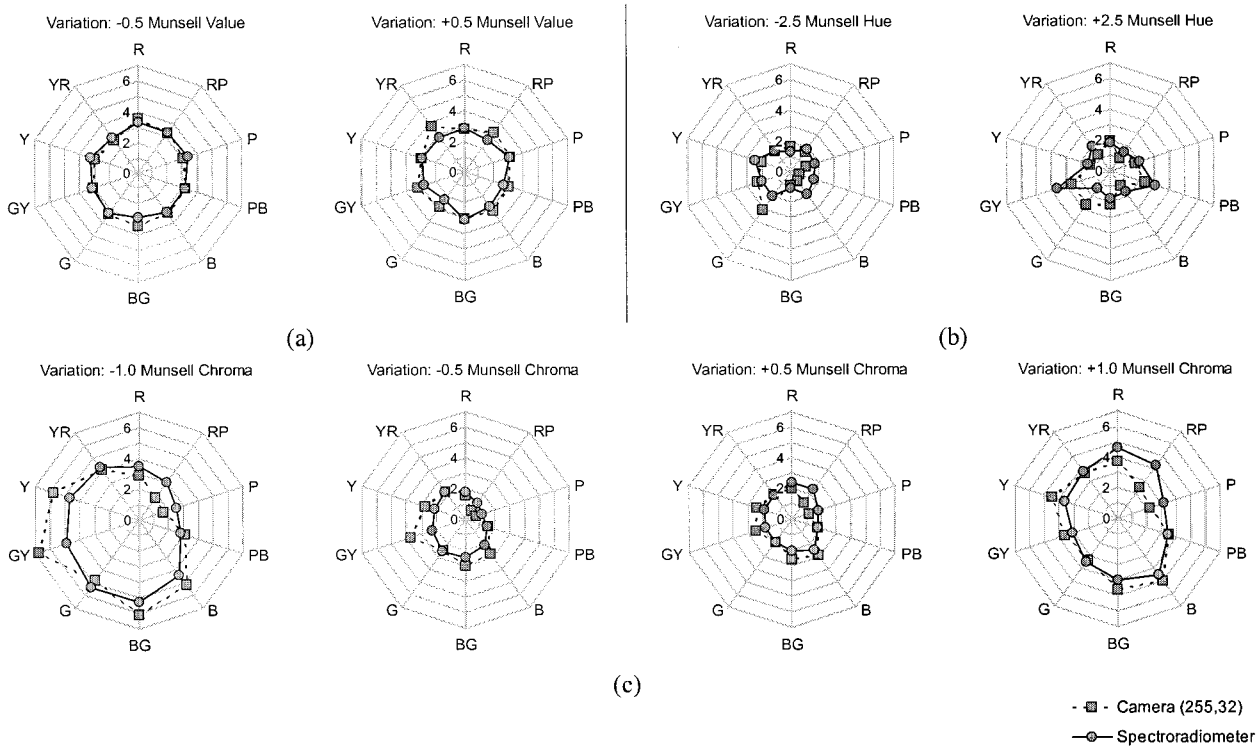

Fig. 9. CIEDE2000 color differences between each group center and its neighbors, calculated for the spectroradiometer and for the camera with (gain, offset) = (255, 32), at ten positions in the circle of hue (Fig. 2). We plot the color differences concerning the following variations in the Munsell system: (a) ±0.5 value, (b) ±2.5 hue, (c) and ±0.5, and ±1.0 chroma.

instead, color difference is what is really important (e.g., in go/not go, pass/fail inspection). We consider the CIELAB formula[9] for the calculation of color differences ΔE_{ab}^* and the more recent CIEDE2000 formula ΔE_{00},[11] also recommended by CIE.

Concerning the amount of uncertainty associated with the measurement process, we consider a specific metric called the mean color difference from the mean[10] (MCDM). For a set of CIELAB measurements, the average ($\bar{L}^*$, $\bar{a}^*$, $\bar{b}^*$) is calculated. Then, a color-difference equation (in our case, either ΔE_{ab}^* or ΔE_{00}) is calculated between each individual measurement and ($\bar{L}^*$, $\bar{a}^*$, $\bar{b}^*$). The average of all the color differences defines the MCDM. The greater the MCDM, the poorer the precision (expressed as a sphere). Although color differences can only be greater than zero and, consequently, a skewed distribution of measurements results, it is still reasonable to use MCDM. As Berns point out,[10] color-difference data are always skewed to larger color differences, and this leads to a larger MCDM, erring on the conservative side when defining instrumental precision. We calculate the MCDM of the measurements obtained from a set of ten samples taken at the central area of a Munsell chip. In the case of the camera measurements, each individual measurement (L_i^*, a_i^*, b_i^*) is, in turn, the average CIELAB coordinates of the central field window of 300 × 300 pixels. We have repeated the procedure for a number of color chips and have observed stability in the final result. Following the notation given in Ref. 10, the value $n\Delta E_{ab}^*$ is the MCDM in the CIELAB metrics. Similarly, the value $n\Delta E_{00}$ is the MCDM in the CIEDE2000 metrics. We have found that the spectroradiometer has a precision, expressed as MCDM, of CIELAB $0.025\Delta E_{ab}^*$ and CIEDE2000 $0.020\Delta E_{00}$. The camera has a precision, expressed as MCDM, of CIELAB $0.05\Delta E_{ab}^*$ and CIEDE2000 $0.06\Delta E_{00}$ working with (gain, offset) = (255, 32). When it captures with (gain, offset) = (255, 0), its precision is CIELAB $0.1\Delta E_{ab}^*$ and CIEDE2000 $0.09\Delta E_{00}$. According to a statistical rule of thumb, the instrumental color tolerance should be no less than ten times the measurement precision. This rule gives us a magnitude order of our instrumental tolerances: $0.25\Delta E_{ab}^*$ or $0.20\Delta E_{00}$ for the spectroradiometer, $0.5\Delta E_{ab}^*$ or $0.6\Delta E_{00}$ for the camera capturing with (gain, offset) = (255, 32), and $1\Delta E_{ab}^*$ or $0.9\Delta E_{00}$ for the camera capturing with (gain, offset) = (255, 0).

We continue our analysis calculating the color differences between each group center of Fig. 2 and its neighbors within the group. We calculate these color differences from the CIELAB coordinates measured by the reference instrument, and, afterwards, we repeat the calculation from the CIELAB coordinates obtained by the camera working with either (gain, offset) = (255, 32) or (gain, offset) = (255, 0).

In Fig. 9, we plot the color differences ΔE_{00}, calculated for the spectroradiometer and for the camera with (gain, offset) = (255, 32), at ten positions in the circle of hue (Fig. 2). In each diagram of Fig. 9, we plot the color differences between each group center

Table 1. Absolute Discrepancies D_{ab}(255, 32) between the Spectroradiometer and the Camera with (gain, offset) = (255, 32) in the Measurement of CIELAB Color Differences

	D_{ab} (255, 32) (±0.06 CIELAB units)							
Group Center	−1.0 Chroma	−0.5 Chroma	+0.5 Chroma	+1.0 Chroma	−0.5 Value	+0.5 Value	−2.5 Hue	+2.5 Hue
5R 8/2	0.271	0.078	0.175	0.544	0.254	0.143	0.342	0.103
5RP 8/2	0.636	0.324	0.699	1.312	0.094	0.909	0.009	0.210
5P 8/2	0.314	0.165	0.264	0.345	0.384	0.016	0.568	0.260
5PB 8/2	0.446	0.061	0.079	0.124	0.196	0.653	0.937	0.298
5B 8/2	0.056	0.178	0.067	0.330	0.110	0.363	1.170	0.671
5BG 8/2	0.955	0.370	0.200	1.026	0.599	0.374	0.406	0.040
5G 8/2	1.727	0.782	0.502	1.366	0.123	0.720	0.322	1.536
5GY 8/2	0.269	0.519	0.235	0.225	0.214	0.431	0.150	1.161
5Y 8/2	0.441	0.436	0.297	0.470	0.560	0.049	0.518	0.308
5YR 8/2	0.302	0.114	0.057	0.104	0.492	1.300	0.065	0.685
Mean	**0.542**	**0.303**	**0.257**	**0.584**	**0.303**	**0.496**	**0.449**	**0.527**

and some neighbors. The color differences plotted concern the following variations in the Munsell system: ±0.5 value [Fig. 9(a)], ±2.5 hue [Fig. 9(b)], and ±0.5 and ±1.0 chroma [Fig. 9(c)].

From the results plotted in Fig. 9, we realize that the camera and the reference instrument present a high level of agreement in the estimation of the color differences. Looking in detail at the figures, we see that the color differences corresponding to ±0.5 value variations [Fig. 9(a)] are nearly uniform as measured by both devices around the circle of hue. Munsell ±2.5 hue variations give rise to color differences in Fig. 9(b) not so uniform around the circle as before. In fact, fluctuations affect the measurements obtained by both the spectroradiometer and the camera. Munsell ±0.5 and ±1.0 chroma variations give rise to relatively oval plots in Fig. 9(c). A high coincidence between both devices can be appreciated when the differences are measured between neighbors that are one Munsell chroma step (±0.5) away from the group center. The discrepancy becomes slightly bigger for neighbors two Munsell chroma steps (±1.0) away from the group center.

D. Instrument Discrepancy

We have estimated the absolute discrepancy D between the color differences measured by the reference instrument and the camera under a given (gain, offset) capturing condition by simply subtracting them and taking the absolute value. Thus we consider the discrepancies defined by the expressions

$$D_{00} = |\Delta E_{00}(\text{ref}) - \Delta E_{00}(\text{cam}_{\text{gain,offset}})|, \quad (3)$$

$$D_{ab} = |\Delta E_{ab}^*(\text{ref}) - \Delta E_{ab}^*(\text{cam}_{\text{gain,offset}})|, \quad (4)$$

where subindex 00 stands for CIEDE2000 in Eq. (3) and subindex ab stands for CIELAB in Eq. (4). Table 1 contain the absolute discrepancies D_{ab} between the spectroradiometer and the camera capturing with (gain, offset) = (255, 32). Although the discrepancies exceed the uncertainty (±0.06 CIELAB units), they fall in general in the camera tolerance ($0.5\Delta E_{ab}^*$) for this (gain, offset) capturing condition. This can be considered a good achievement for the camera performance. It can be seen that most of the absolute discrepancies of Table 1 are even lower than

Table 2. Relative Discrepancies D_{00}^r (255, 32) between the Spectroradiometer and the Camera with (gain, offset) = (255, 32) in the Measurement of CIEDE2000 Color Differences

	D_{00}^r (255, 32)									
Group Center	−1.0 Chroma	−0.5 Chroma	+0.5 Chroma	+1.0 Chroma	−0.5 Value	+0.5 Value	−2.5 Hue	+2.5 Hue	Mean	Std.
5R 8/2	0.193	0.131	0.191	0.214	0.063	0.014	0.233	0.061	**0.137**	0.082
5RP 8/2	0.541	0.581	0.559	0.544	0.029	0.208	0.098	0.357	**0.365**	0.226
5P 8/2	0.427	0.436	0.409	0.341	0.084	0.006	0.427	0.209	**0.293**	0.171
5PB 8/2	0.099	0.044	0.012	0.013	0.014	0.145	0.976	0.262	**0.196**	0.327
5B 8/2	0.170	0.298	0.139	0.085	0.017	0.120	0.770	0.359	**0.245**	0.239
5BG 8/2	0.153	0.192	0.230	0.133	0.187	0.015	0.200	0.209	**0.165**	0.068
5G 8/2	0.095	0.048	0.005	0.054	0.015	0.217	0.432	0.627	**0.187**	0.228
5GY 8/2	0.323	0.491	0.288	0.153	0.009	0.147	0.140	0.324	**0.235**	0.150
5Y 8/2	0.218	0.270	0.234	0.210	0.096	0.050	0.210	0.086	**0.172**	0.082
5YR 8/2	0.043	0.022	0.030	0.043	0.100	0.283	0.019	0.425	**0.121**	0.151
Mean	**0.226**	**0.251**	**0.210**	**0.179**	**0.061**	**0.121**	**0.351**	**0.292**		
Std.	0.158	0.200	0.179	0.162	0.057	0.097	0.308	0.167		

Table 3. Relative Discrepancies $D_{ab}{}^{r}$ (255, 32) between the Spectroradiometer and the Camera with (gain, offset) = (255, 32) in the Measurement of CIELAB Color Differences

	$D_{ab}{}^{r}$ (255, 32)									
Group Center	−1.0 Chroma	−0.5 Chroma	+0.5 Chroma	+1.0 Chroma	−0.5 Value	+0.5 Value	−2.5 Hue	+2.5 Hue	Mean	Std.
5R 8/2	0.083	0.045	0.069	0.107	0.051	0.033	0.191	0.041	**0.078**	0.052
5RP 8/2	0.284	0.347	0.363	0.368	0.020	0.209	0.004	0.151	**0.218**	0.148
5P 8/2	0.139	0.157	0.150	0.105	0.083	0.003	0.335	0.136	**0.138**	0.094
5PB 8/2	0.145	0.039	0.039	0.031	0.043	0.157	0.834	0.118	**0.176**	0.271
5B 8/2	0.013	0.083	0.024	0.064	0.024	0.083	0.968	0.528	**0.223**	0.345
5BG 8/2	0.194	0.147	0.084	0.222	0.133	0.082	0.324	0.018	**0.151**	0.096
5G 8/2	0.327	0.288	0.232	0.324	0.026	0.193	0.119	0.607	**0.264**	0.173
5GY 8/2	0.035	0.129	0.069	0.040	0.047	0.096	0.052	0.367	**0.104**	0.111
5Y 8/2	0.058	0.117	0.083	0.066	0.124	0.011	0.261	0.200	**0.115**	0.081
5YR 8/2	0.057	0.038	0.019	0.018	0.123	0.269	0.035	0.334	**0.112**	0.123
Mean	**0.133**	**0.139**	**0.113**	**0.134**	**0.067**	**0.114**	**0.312**	**0.250**		
Std.	0.107	0.105	0.108	0.126	0.045	0.090	0.333	0.201		

Table 4. Relative Discrepancies $D_{00}{}^{r}$ (255, 0) between the Spectroradiometer and the Camera with (gain, offset) = (255, 0) in the Measurement of CIEDE2000 Color Differences

	$D_{00}{}^{r}$ (255, 0)									
Group Center	−1.0 Chroma	−0.5 Chroma	+0.5 Chroma	+1.0 Chroma	−0.5 Value	+0.5 Value	−2.5 Hue	+2.5 Hue	Mean	Std.
5R 8/2	0.108	0.088	0.105	0.133	0.057	0.156	0.604	0.054	**0.163**	0.182
5RP 8/2	0.484	0.545	0.484	0.479	0.140	0.114	0.193	0.283	**0.340**	0.177
5P 8/2	0.157	0.175	0.161	0.097	0.186	0.075	0.262	0.223	**0.167**	0.061
5PB 8/2	0.233	0.172	0.159	0.165	0.114	0.053	0.851	0.154	**0.238**	0.253
5B 8/2	0.269	0.410	0.276	0.235	0.082	0.023	0.633	0.143	**0.259**	0.194
5BG 8/2	0.306	0.355	0.339	0.255	0.071	0.094	0.069	0.528	**0.252**	0.164
5G 8/2	0.051	0.019	0.171	0.071	0.074	0.102	0.455	0.777	**0.215**	0.265
5GY 8/2	0.548	0.675	0.412	0.271	0.148	0.044	0.214	0.317	**0.329**	0.209
5Y 8/2	0.448	0.471	0.405	0.361	0.223	0.063	0.083	0.006	**0.258**	0.188
5YR 8/2	0.110	0.170	0.206	0.123	0.231	0.178	0.353	0.299	**0.209**	0.084
Mean	**0.271**	**0.308**	**0.272**	**0.219**	**0.133**	**0.090**	**0.372**	**0.278**		
Std.	0.173	0.215	0.131	0.128	0.064	0.049	0.259	0.229		

the suprathreshold for visual discrimination of 0.887 CIELAB units.[16]

We consider that the results obtained so far for the camera are actually very good, and they confirm the camera studied as a reliable imaging system for the measurement of small color differences, particularly in the pale color region.

For further analysis of the camera performance, we have considered relative discrepancies. The relative discrepancy is the absolute discrepancy divided by

Table 5. Relative Discrepancies $D_{ab}{}^{r}$ (255, 0) between the Spectroradiometer and the Camera with (gain, offset) = (255, 0) in the Measurement of CIELAB Color Differences

	$D_{ab}{}^{r}$ (255, 0)									
Group Center	−1.0 Chroma	−0.5 Chroma	+0.5 Chroma	+1.0 Chroma	−0.5 Value	+0.5 Value	−2.5 Hue	+2.5 Hue	Mean	Std.
5R 8/2	0.076	0.104	0.084	0.054	0.045	0.152	0.554	0.041	**0.139**	0.171
5RP 8/2	0.150	0.231	0.204	0.217	0.111	0.129	0.335	0.009	**0.173**	0.097
5P 8/2	0.210	0.191	0.200	0.247	0.170	0.074	0.108	0.087	**0.161**	0.063
5PB 8/2	0.408	0.303	0.327	0.331	0.130	0.074	0.585	0.124	**0.285**	0.171
5B 8/2	0.204	0.263	0.167	0.139	0.111	0.012	0.861	0.270	**0.254**	0.260
5BG 8/2	0.038	0.021	0.049	0.071	0.032	0.172	0.026	0.310	**0.090**	0.101
5G 8/2	0.110	0.132	0.019	0.095	0.092	0.094	0.228	0.802	**0.196**	0.251
5GY 8/2	0.334	0.428	0.352	0.241	0.144	0.046	0.274	0.227	**0.256**	0.121
5Y 8/2	0.337	0.383	0.367	0.343	0.205	0.060	0.086	0.101	**0.235**	0.138
5YR 8/2	0.268	0.278	0.253	0.208	0.223	0.191	0.295	0.220	**0.242**	0.037
Mean	**0.213**	**0.233**	**0.202**	**0.195**	**0.126**	**0.100**	**0.335**	**0.219**		
Std.	0.123	0.125	0.125	0.102	0.062	0.058	0.261	0.228		

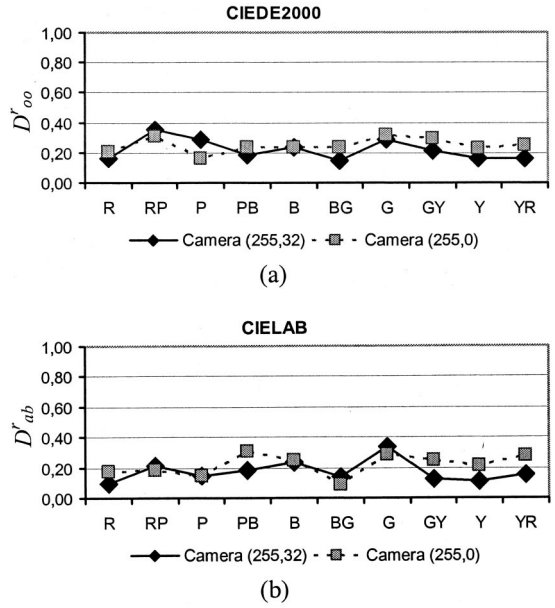

Fig. 10. Relative discrepancies versus group color: (a) in CIEDE2000, (b) in CIELAB. Data are taken from Tables 2–5.

the mean value of the color differences measured by the spectroradiometer and the camera,

$$D_{00}{}^{r} = \frac{D_{00}}{\langle \Delta E_{00}(\text{ref}),\ \Delta E_{00}(\text{cam}_{\text{gain,offset}}) \rangle} = \frac{2|\Delta E_{00}(\text{ref}) - \Delta E_{00}(\text{cam}_{\text{gain,offset}})|}{\Delta E_{00}(\text{ref}) + \Delta E_{00}(\text{cam}_{\text{gain,offset}})}. \quad (5)$$

An analogous equation would be obtained for the CIELAB metrics by replacing subindex 00 with ab in Eq. (5). Tables 2 to 5 contain the relative discrepancies in both metrics for the camera capturing conditions (gain, offset) = {(255, 32), (255, 0)}. In each table, we have taken the mean value and the standard deviation by rows (i.e., all the relative discrepancies related to a given group center), and the results are plotted in Fig. 10. It shows that the camera behaves rather uniformly around the circle of hue. We have also taken the mean value and the standard deviation by columns in Tables 2 to 5, and the results are plotted in Fig. 11. This figure shows that the camera is highly accurate when it measures chroma and value variations, but less accurate for hue variations.

From Figs. 10 and 11, it is difficult to conclude which (gain, offset) capturing condition, (255, 32) or (255, 0), is better, because they both lead to similar results. Instead, this study eventually demonstrates that the selection of the offset value admits some tolerance. The tolerance in the offset value, along with the tolerance in the gain value pointed out in Subsection 3.B, demonstrates that the selections of the gain and offset values are not critical for the considered colorimetric application. Thus it can be said that the imaging system analyzed is a good instrument for color-difference measurements and robust to variations in the capturing conditions of (gain, offset).

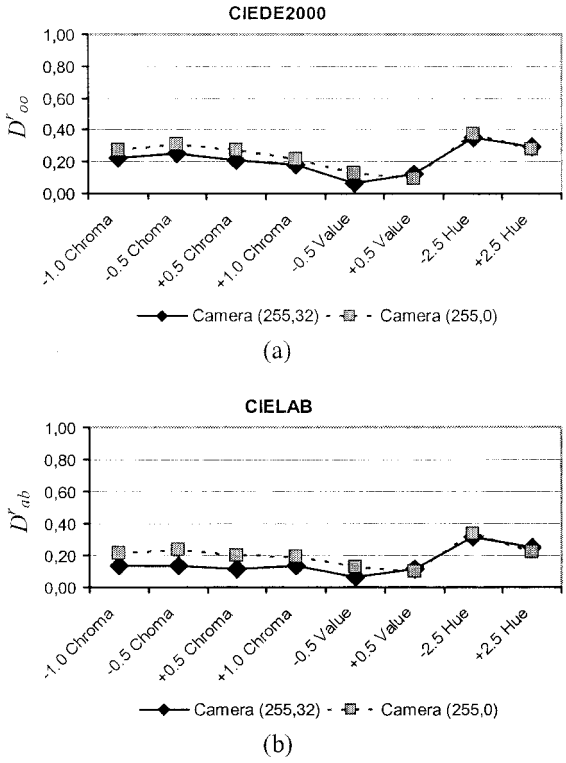

Fig. 11. Relative discrepancies versus type of variation with respect to the group center: (a) in CIEDE2000, (b) in CIELAB. Data are taken from Tables 2–5.

4. Conclusions

The method presented has been demonstrated to be useful to analyze the discrimination capability of a color camera for colorimetric purposes. In its first stage, the method helps to select the working conditions of the acquisition system. The comparison between the camera response and a reference instrument in the measure of luminance (L^*) of a gray scale led us to select the gain and the offset range of values in a more appropriate way than by considering the camera response in the separate RGB channels exclusively. In addition to this, our method takes into account possible chromatic deviations in capturing achromatic samples and compares them with the response of the reference instrument. This sort of analysis can also be used as a basis to establish tolerances in the camera response with respect to the reference instrument.

The second stage of the method analyzes the reliability of a camera for the measurement of color and color differences. To test the camera capability in a difficult case of discrimination, we have considered small color differences in the very pale color region of the Munsell system. A test of 90 Munsell chips distributed in groups of neighbors around the circle of hue has been used to compare the responses of the camera and the reference instrument. This study has allowed us to evaluate the camera's performance

for the absolute measurement of color and for the relative measurement of color through the calculation of color differences. The discrepancies between the results obtained by the camera and by the reference instrument are used to test the reliability of the camera's performance. The experiment proposed in the second stage of the method also provides information about the uniformity of the camera response along different hue regions, for luminance variations only, and for chroma variations only.

We have applied the method to the Sony DX-9100P color camera (Matrox Meteor II M/C frame grabber) capturing under the illumination of a real D65 simulator, and we have compared it with the Photo Research PR-715 spectroradiometer. Following our method, the gain and offset ranges of values were first selected, and two pairs of (gain, offset) values were analyzed during the whole experiment. Second, we measured the CIELAB coordinates of 90 Munsell chips in the very pale color region using the spectroradiometer and the camera under two capturing conditions.

Although the lack of coincidence in the absolute measurements of color is appreciable, we conclude that the camera is reliable to measure color differences. This reliability has been quantitatively estimated through the absolute discrepancy in the measurement of color differences with respect to the reference instrument. Discrepancies have been addressed considering the MCDM metric to represent the uncertainty, and ten times this amount, to determine the instrumental color tolerance. Although the discrepancies exceed the uncertainty, they fall, in general, in the camera tolerance for a given (gain, offset) capturing condition. This is a good achievement for the camera performance. Moreover, the absolute discrepancies are generally lower than the suprathreshold for visual discrimination of 0.887 CIELAB unit.

The analysis of the relative discrepancy shows that the camera behaves quite uniformly around the circle of hue; it is highly accurate when it measures chroma and value variations, but somewhat less accurate for hue variations. We also conclude that the selection (gain, offset) = (255, 32) is suitable but not critical. Moreover, the camera's performance is robust to variations of these values. The results obtained in this work using the CIELAB color-difference equation are very close to those obtained using CIEDE2000; thus the conclusions outlined are consistent in both metrics.

For future study, practical real cases of pale color sample pairs of several materials (textile, ceramic, etc.) that involve nonuniform or textured color samples are to be considered. Taking into account the conclusions outlined in this work, we consider that an image-acquisition system based on a 3CCD camera has promising characteristics for objective and automatic inspection of color matching.

The authors acknowledge the Spanish Ministerio de Ciencia y Tecnología for financial support under project DPI2003-03931. They also thank Javier Romero from the Universidad de Granada and Miquel Ralló from the Universidad Politécnica de Cataluña for fruitful discussions.

References

1. P. L. Vora, J. E. Farrell, J. D. Tietz, and D. H. Brainard, "Digital color cameras. 1. Response models," Tech. Rep. HPL-97-53 (Hewlett-Packard Laboratory, Palo Alto, Calif., 1997); http://www.hpl.hp.com/techreports/97/HPL-97-53.html.
2. P. L. Vora, J. E. Farrell, J. D. Tietz, and D. H. Brainard, "Digital color cameras. 2. Spectral response," Tech. Rep. HPL-97-54 (Hewlett-Packard Laboratory, Palo Alto, Calif., 1997); http://www.hpl.hp.com/techreports/97/HPL-97-54.html.
3. K. Barnard and B. Funt, "Camera characterization for color research," Color Res. Appl. **27**(3), 152–163 (2002).
4. G. Hong, M. R. Luo, and P. A. Rhodes, "A study of digital camera colorimetric characterization based on polynomial modeling," Color Res. Appl. **26,** 76–84 (2001).
5. P. L. Vora and H. J. Trussell, "Measure of goodness of a set of color-scanning filters," J. Opt. Soc. Am. A **10,** 1499–1508 (1993).
6. L. T. Maloney and B. A. Wandell, "Color constancy: a method for recovering surface spectral reflectance," J. Opt. Soc. Am. A **3,** 29–33 (1986).
7. M. L. Simpson and J. F. Jansen, "Imaging colorimetry: a new approach," Appl. Opt. **30,** 4666–4671 (1991).
8. M. Corbalán, M. S. Millán, and M. J. Yzuel, "Color measurement in standard CIELAB coordinates using a 3CCD camera: correction for the influence of the light source," Opt. Eng. **39,** 1470–1476 (2000).
9. G. Wyszecki and W. S. Stiles, *Color Science: Concepts and Methods, Quantitative Data and Formulae* (Wiley, New York, 1982).
10. R. S. Berns, *Billmeyer and Saltzman's Principles of Color Technology*, 3rd ed. (Wiley, New York, 2000).
11. M. R. Luo, G. Cui, and B. Rigg, "The development of the CIE 2000 colour-difference formula: CIEDE2000," Color Res. Appl. **26**(5), 340–350 (2001).
12. G. Johnson and M. D. Fairchild, "A top down description of S-CIELAB and CIEDE2000," Color Res. Appl. **28**(6), 425–435 (2003).
13. R. S. Berns and D. M. Reiman, "Color managing the 3rd edition of *Billmeyer and Saltzman's Principles of Color Technology*," Color Res. Appl. **27**(5), 360–373 (2002).
14. M. Corbalán, M. S. Millán, and M. J. Yzuel, "Color pattern recognition with CIELAB coordinates," Opt. Eng. **41,** 130–138 (2002).
15. C. S. McCamy, H. Marcus, and J. G. Davidson, "A color-rendition chart," J. Appl. Photogr. Eng. **2,** 95–99 (1976).
16. M. Melgosa, E. Hita, A. J. Poza, D. H. Alman, and R. S. Berns, "Suprathreshold color-difference ellipsoids for surface colors," Color Res. Appl. **22**(3), 148–155 (1997).

Small color differences in the very pale and dark grayish regions measured by camera

J. Imaging Sci. Technol. **49**(6), 605-619 (2005).

Small Color Differences in the Very Pale and Dark Grayish Regions Measured by Camera

Edison Valencia and María S. Millán
Departamento de Optica y Optometría, Universidad Politécnica de Cataluña, Terrassa, Barcelona, SPAIN

The camera capability to measure small color differences between sample pairs is evaluated by comparing the camera performance with a reference instrument. To this end, the appropriate working conditions are established, the camera spectral sensitivities and imaging noise are characterized, and the transformation to obtain a device independent representation of color is calculated considering two approaches: one, on the basis of the camera spectral sensitivity (CSS), and two, on the basis of the unified measure of goodness of the camera (UMG) that involves an imaging noise model. The camera performance is assessed from the measurement results of a large number of varied small color differences in the very pale and the dark grayish color regions, the involved uncertainty, the absolute discrepancy, and the relative discrepancy with respect to the reference instrument. In the experimental application, the three CCD camera SONY DX-9100P is assessed and compared with the spectroradiometer Photo Research PR-715 as reference instrument. The results reveal a high quality performance of the camera system, with absolute discrepancies in the estimation of color differences around the camera tolerances (CIELAB $0.5\Delta E^*_{ab}$ or CIEDE2000 $0.6\ \Delta E_{00}$). The color uniformity in textile dying is evaluated by analyzing some pairs of extreme center fabric samples. Although the camera is more sensitive to the texture effects than the spectroradiometer, both instruments yield consistent and satisfactory Pass/Fail results.

Journal of Imaging Science and Technology 49: 605–619 (2005)

Introduction

The characterization of a camera orientated to colorimetric purposes has been described in Refs. 1 through 4. Important applications can be found in color management, for which the acquisition of the color content of either a scene or an image and the transformation to obtain a device independent representation of color are some of the basic stages. Some applications propose to develop databases of calibrated color images. Face colors under varying lighting conditions are the object of the Physics-Based Face Database for color research.[5] Xiao et al. describe an initial methodology to create a database of high dynamic range, color images that represent typical scenes in digital photographs.[6] Such a database[7] should help the development and evaluation of rendering methods and it can also be used to evaluate the constraints imposed by image sensors and lens configurations. Other examples of colorimetric applications of digital cameras can be found in end-to-end color reproduction systems. The possibilities and limitations of commercial input and output devices have been examined in order to produce hardcopy results that are spectrally matched to original colors.[8] The approach consists of scene capture using a trichromatic digital camera combined with multiple color filtration,[9] image processing, and four color ink jet printing.[8]

As far as we know, less effort has been devoted to exploit the discrimination capability of color cameras in the measurement of color differences. A possible reason may be the existence of a number of instruments (colorimeters, spectrophotometers, spectroradiometers) capable of measuring color differences with high precision. These instruments, however, measure color in an integration area of the sample with limited flexibility in configuration, dimensions and sample scanning. These conditions cannot be easily modified in general, even when using expensive and sophisticated instruments. Marszalec et al.[10] studied the performance of color cameras for measuring small color differences and related it to metamerism. They concentrated on the fact that, in general, color cameras and human vision have not exactly the same response functions and, consequently, they could find a number of sample pairs that were metameric or very similar for the human observer but were measured by a color camera as separate colors. They evaluated how similar these colors were in the RGB camera color space by using a non established formula.

In this article we consider a 3CCD camera to measure small color differences with applications in industrial inspection. We emphasize that the target measure here is the "size" of color difference, not color accuracy. This goal in itself is valid, especially for applications where color uniformity, not color fidelity, is the concern. We fix the working conditions of the camera system according

Original manuscript received January 12, 2004

Corresponding Author: Edison Valencia, edison@oo.upc.edu

to methods previously described in Ref. 11. In that study, the camera performance was compared with the performance of a reference instrument in a camera independent color space. In addition to the characterization of the spectral sensitivities of the camera and the Vora–Trussell measure of goodness[12] considered previously in Ref. 11, in this work we also consider the characterization of imaging noise related to dark current, shot noise, and the unified measure of goodness (UMG).[13] This more general approach leads us to compute new coefficients for the linear transform applied to the RGB camera values to obtain the XYZ tristimulus values in the device independent color representation. In this work we explore the reliability of the camera system and estimate the precision and accuracy considered before Ref. 11 and the approach involving the UMMG.

In the experiments we pay particular attention to the nearly neutral region of the color space (unsaturated colors). The nearly neutral colors imply a similar stimulation of the three red-, green- and blue-sensitive channels of the camera, and the differences between these colors involve small variations on a nearly constant background signal. Although humans show a subjective preference for colorfully enhanced images, real colors of original scenes are not as saturated as observers prefer.[14,15] There are a large number of examples, particularly in the western culture, for which unsaturated colors compose the main part of real scenes: natural scenes in cold countries, outdoor city scenes, indoor scenes, suits and other clothing, wall paints and decoration, human skin and faces, etc. Saturated colors are rather limited to children in western countries. Due to such cultural reasons, unsaturated colors draw industrial attention, particularly in the textile industry, which has motivated the application presented in this article. Finally, as a practical consideration, two matte Munsell collections: the Book of Color and the Nearly Neutral Collection, were available to the authors. These provided them with large enough color sample sets to carry out this study.

The CIELAB[16,17] and the more recent CIEDE2000[18] formulae are used in this work to compute color differences. More especially, CIEDE2000 includes a term to improve performance of low-chroma colors[19] and therefore we have considered it suitable for our study. We analyze the camera performance for the very pale and the dark grayish color regions. As an example of application, we consider a practical real case of color matching in the textile industry.

Method for Camera Evaluation

The method aims to assess the discrimination capability of a camera to measure small color differences. We are concerned with the accuracy and precision of the camera and compare it with a reference instrument that is assumed to be calibrated, high quality, and to have a linear response. The method has several stages, including the camera calibration.

Firstly, we determine the appropriate working conditions of the acquisition system. A camera based color imaging acquisition system consists of a camera (often 3CCD), a framegrabber, a PC, and a given lighting-viewing configuration. We compare the camera and the reference instrument in the same illumination/observation conditions (Fig. 1): we use an observation booth with a given light source and a given illumination/observation geometry for which the scene is captured away from specular reflections.

In the camera initialization, the gamma function and the automatic gain control are disabled, and the camera raw signal is white balanced to a given illuminant. The framegrabber converts the analog signal of the camera into the R, G, B digital values (for instance, from 0 to 255 in an 8 bit camera). In the analog to digital conversion, the gain and offset values have to be fixed. In Ref. 11, we measured the R, G, and B responses of the camera when it captures a gray scale using all the four possible combinations where the gain and the offset take the extreme values of the range, i.e., either 0 or 255. Since the camera response that profits from maximum dynamic range with minimum alteration in the signal is usually sought, we tentatively selected the combination of (gain, offset) that best approached this property. We considered intervals around these gain and offset tentative values to further analyze the camera response within such intervals and, consequently, to refine the gain and offset selection.

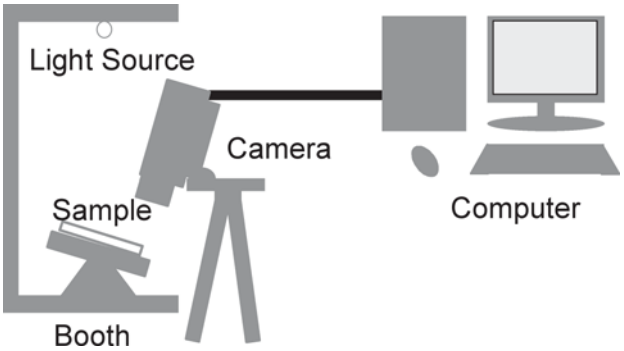

Figure 1. Setup scheme. The camera can be replaced by the spectroradiometer (reference instrument) at the same position so that both instruments measure with the same illumination/observation geometry.

The calibration of a 3CCD camera should involve both the measurement of its 3CCD spectral sensitivities and its noise properties. There are various methods described in the literature to estimate the spectral sensitivity curves of the sensors, e.g., Refs. 2, 3, and 20–22. A conceptually simple method, which we have already followed,[11] is based on stimulating the camera with very narrow band illumination produced by a monochromator.[2] The three RGB spectral sensitivity functions are a set of color scanning filters for which the Vora–Trussell measure of goodness (ν factor, defined in Ref. 12) can be determined. The ν factor is used to characterize input devices, such as cameras or scanners, and indicates the similarity of the set of the device spectral sensitivities to human color matching functions, so that ν = 1 means a perfect fit. According to Berns and Reiman,[23] values of the ν factor above 0.9 are desirable for colorimetric purposes in the first approach.

To overcome the device dependent representation of color based on the R, G, B components provided by the camera, we calculate the coefficients of the linear transformation that defines a mapping between the camera RGB signals and a device independent representation, such as the standard CIE 1931 XYZ. In this study, we consider two ways of calculating the (3 × 3) linear matrix. In one of them, the coefficients are calculated following the method[24,25] which takes into account the three spectral response curves of the camera sensors, the standard observer responses x_{10}, y_{10}, z_{10} (CIE 1976), and the spectral distribution of the white light source. This calculation was already used in our former work,[11] but it does not consider the noise properties of the camera.

A more complete calibration increases the camera's measure of goodness by considering noise characteristics. Among the research works on CCD camera calibration that

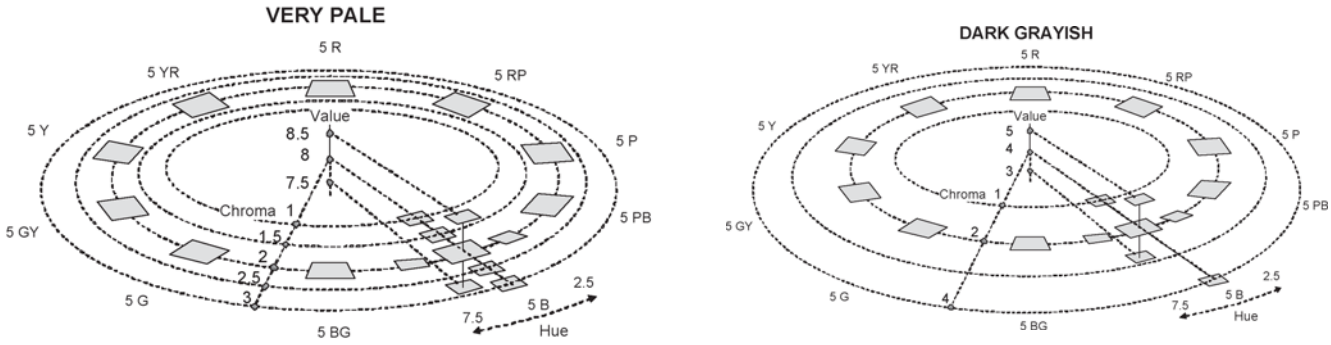

Figure 2. Test of nearly neutral Munsell chips organized in two subsets: (a) very pale sample subset, and (b) dark grayish sample subset. In each one, there are ten groups of samples regularly distributed around the Hue circle. Each group consists of a group center and its closest neighbors (there is a group sketched in detail in both figures).

estimate noise, we mention the work of Healey and Kondepudy for a single CCD camera[26] and the work of Quan et al.[13] that is closer to ours. In the latter, the CCD noise model has two main components: a signal independent noise such as dark noise and a signal dependent noise represented by shot noise. Dark current noise can be measured by taking images with the camera aperture totally closed at ambient temperature. This noise has an average value, which is often subtracted from the output signal, but it also exhibits fluctuations that create fixed pattern noise.[27] Shot noise is associated with the random arrival of photons at the CCD. It is governed by Poisson statistics and, consequently, the shot noise variance is equal to the mean input signal. In our study, we assume the zero mean noise model considered by Quan et al.[13] whose variance σ_η^2 is given by

$$\sigma_\eta^2 = \sigma_d^2 + k\mu_i \,, \tag{1}$$

where σ_d^2 denotes the dark noise variance, $\sqrt{k}$ is the photon-electron conversion quantum efficiency coefficient of the CCD, and μ_i is the input signal intensity, which coincides with the shot noise variance (σ_i^2). From Eq. (1), the noise is dominated by dark noise when the input signal level is low. But when the input signal level is high, shot noise, which is proportional to the signal level, dominates. Noise levels can be represented by digital counts relative to the digital count of maximal signal in Eq. (1). The coefficient k associated to shot noise can be obtained by fitting Eq. (1) with a series of signal levels and the corresponding signal variations. Taking into account the metric called Unified Measure of Goodness (UMG), proposed by Quan et al.,[13] we can compute the coefficients of a linear matrix converting camera RGB to CIE XYZ through the minimization of noise propagation. This metric minimizes the average color difference or error for an ensemble of standard reflectance samples in a perceptually uniform color space. For additional properties and details about the computing procedure, the reader is referred to Quan et al.'s paper.[13]

The CIELAB coordinates L^* a^* b^* (CIE 1976) can be calculated from CIE XYZ using the standard formulae.[16,17] CIELAB chroma C_{ab}^* and hue h_{ab}, that correspond to the polar coordinates of this cylindrical representation system for which the luminance L^* gives the axis, will also be computed and used.

Concerning the amount of uncertainty associated with the measurement process we consider a specific metric called the mean color difference from the mean (MCDM).[17] For a set of CIELAB measurements, the average ($\overline{L}^*$, $\overline{a}^*$, $\overline{b}^*$) is calculated. Then, a color difference equation (in our case, either ΔE^*_{ab} CIELAB[16,17] or ΔE_{00} CIEDE2000[18]) is calculated between each individual measurement and ($\overline{L}^*$, $\overline{a}^*$, $\overline{b}^*$). The average of all the color differences defines the MCDM. The greater the MCDM, the poorer the precision. We calculate the MCDM of the measurements obtained from a set of ten samples taken at the center of a single Munsell patch. In the case of the camera measurements, each individual measurement (L_i^*, a_i^*, b_i^*) is, in turn, the average CIELAB values of the CIELAB values of each of the 300 × 300 pixels that compose the central field window of the captured image in our case. We repeat the procedure for a number of color patches to observe stability in the final result. Following the notation given in Ref. 17, the value $\nu\Delta E^*_{ab}$ is the MCDM in the CIELAB metrics. Similarly, the value $n\Delta E_{00}$ is the MCDM in the CIEDE2000 metrics. We calculate these values to estimate the precision of both the reference instrument and the camera. According to a common statistical rule, the instrumental color tolerance should be no less than ten times the precision. This rule will give us a magnitude order of our instrumental tolerances.

In the following stage of the method, we assess the capability of the camera to measure small color differences, and compare the measurements obtained by the camera with those obtained by the reference instrument. We focus on the extremes of the unsaturated color region, i.e., the very pale and dark grayish colors. To this end, we build a test consisting of samples from two matte Munsell collections: the Munsell Book of Color and the Nearly Neutral Munsell Collection. Ten selected samples are regularly distributed in the hue circle (Fig. 2). They have low value of Chroma = 2, and two values of Value: V = 8 (Fig. 2(a)), and V = 4, (Fig. 2(b)). The two subsets of samples generated in this way are the very pale color subset (with V = 8)[11] and the dark grayish color subset (with V = 4). In the experiment, each one of the selected chips has to be compared with its neighbors according to the sketches of Figs. 2(a) and 2(b).

According to the test of Fig. 2, a large number (140) of color differences between nearest neighbor pairs are separately evaluated by both the camera and the reference instrument. CIELAB ΔE^*_{ab} and CIEDE2000 ΔE_{00} formulae are used to calculate the color differences. The comparison of the results gives the discrepancy between the instruments. The absolute discrepancy D_i can be es-

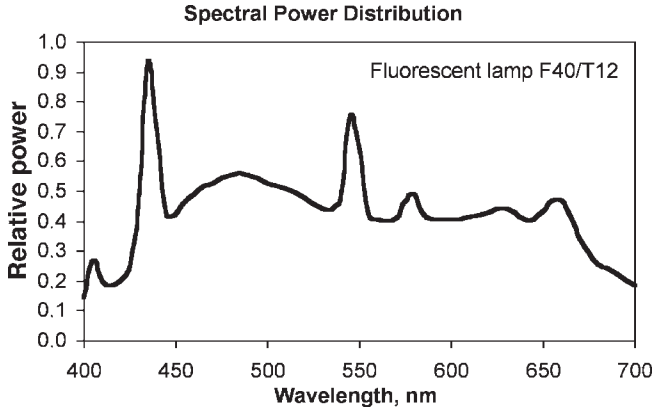

Figure 3. Spectral power distribution of the fluorescent lamp F40/T12 installed in the booth as D65 daylight simulator.

timated by simply subtracting the color differences measured by the reference instrument and the camera, and taking the absolute value, that is,

$$D_i = \left|\Delta E_i\left(ref\right) - \Delta E_i\left(cam\right)\right|, \tag{2}$$

where subindex $i = \{ab, 00\}$ indicates either the CIELAB or the CIEDE2000 metric in Eq. (2). The relative discrepancy D_i^r is the absolute discrepancy divided by the mean value $\langle\cdot\rangle$ of the color differences measured by the spectroradiometer and the camera,

$$D_i^r = \frac{D_i}{\left\langle \Delta E_i\left(ref\right), \Delta E_i\left(cam\right)\right\rangle} = \frac{2\left|\Delta E_i\left(ref\right) - \Delta E_i\left(cam\right)\right|}{\Delta E_i\left(ref\right) + \Delta E_i\left(cam\right)}. \tag{3}$$

These discrepancies are used to test the level of agreement between both the camera and the reference instrument in the estimation of the color differences. Since the reference instrument is of high quality, its tolerance is commonly low (0.5 ΔE^*_{ab} or even coger). As a consequence, these discrepancies allow us to evaluate the reliability of the camera's performance. If the absolute discrepancies do not exceed the uncertainty, then the measurements are indistinguishable. This is an ideal case. More realistically, if the camera tolerance is acceptable (about $1.0\Delta E^*_{ab}$) and the absolute discrepancies fall in general within the camera tolerance, then it can be considered a good achievement for the camera. The relative discrepancies provide information about the accuracy and uniformity of the camera's performance in evaluating hue, chroma or value differences.

Experimental Results

We have applied the method described above to characterize the discrimination capability of a 3CCD camera. The image acquisition system of our study consists of the following components:

- 3CCD camera SONY DX-9100P, with nominal SNR of 57dB,
- Framegrabber MATROX Meteor II M/C (8 bits) that captures a 640 × 780 pixel size image and digitizes the analog signal provided by the camera into 256 gray levels for each R, G, and B channel. The framegrabber is integrated into a personal computer that is used for subsequent calculations.
- Observation booth VeriVide CAC 120H4 with a D65 daylight simulator given by a fluorescent lamp F40/T12. We measured its spectral power distribution (Fig. 3), and its correlated color temperature was 6,438 K (10º observer).

The color camera was configured with the automatic gain control disabled (0 dB level) and the gamma function equal to 1.0 because otherwise it could distort colors. For the white calibration or white balance, we imaged a standard reflectance plate (Photoresearch RS-3) under the illumination given by the D65 daylight simulator of the booth. The entire field of view was then a white area of the standard plate imaged by the camera and, in this situation, the camera made automatic adjustments of the channel responses to achieve the white balance. The reflectance spectral distribution of the plate was nearly constant and equal to 1 (its calibration did not exceed ±0.6% versus the values of a reference calibrating source, within 380–780 nm). We occluded totally the camera lens aperture for the black reference. The camera aperture remained fixed at *f*/#=4 during the rest of the experiment.

The camera is compared with a calibrated spectroradiometer as reference instrument. We used the spectroradiometer Photo Research PR-715. It measured the central area of a Munsell chip with 1º aperture or field coverage.

The camera and the reference instrument worked with the same illumination/observation geometry 20º/0º (replacing the camera by the spectroradiometer in the setup of Fig. 1). Since the samples we consider are matte in general, the choice of the illumination geometry is not critical. We observed that a standard 45º illumination gave rise to some image artifacts or noise caused by a shading effect on the rough matte surface. Instead, we decided to use an approximate 20º illumination for all the measurements. Regarding the observation, the camera was placed in front of the sample, in the direction perpendicular to the sample surface. A frontal viewing is preferable to a slant viewing because it reduces focus errors and geometrical distortions produced by perspective that could be important for future applications to spatially variant images. We verified that the illumination was almost uniform throughout the sample placed inside the booth. The camera lens was adjusted so that the field of view was entirely filled by a single Munsell chip (approximately 3.5 cm^2).We always analyzed, however, a central window of 300 × 300 pixel size.

The gain and offset values were not selected for each R, G, B channel independently, but on the contrary, the gain and offset pair was the same for all the three channels. For an initial selection of the gain and offset values, a gray scale was captured by the camera setting the four combinations of extreme values, i.e., (gain, offset) = {(0,0), (0,255), (255,0), (255,255)}.[11] The camera response that allowed maximum dynamic range with the minimum alteration in the signal was sought. The combination (gain, offset) = (255,0) gave the best camera response out of the four measured. After this coarse selection, we considered intervals around the gain and offset values to further analyze the camera response within such intervals and, consequently, to make a fine selection of the gain and offset. The intervals of greatest interest were eventually limited to gain = [255…128] and offset = [0…64] in our former work. We considered six gain and offset pairs belonging to these intervals and measured the R, G, B responsitivity functions of the camera for each pair. The R, G, B

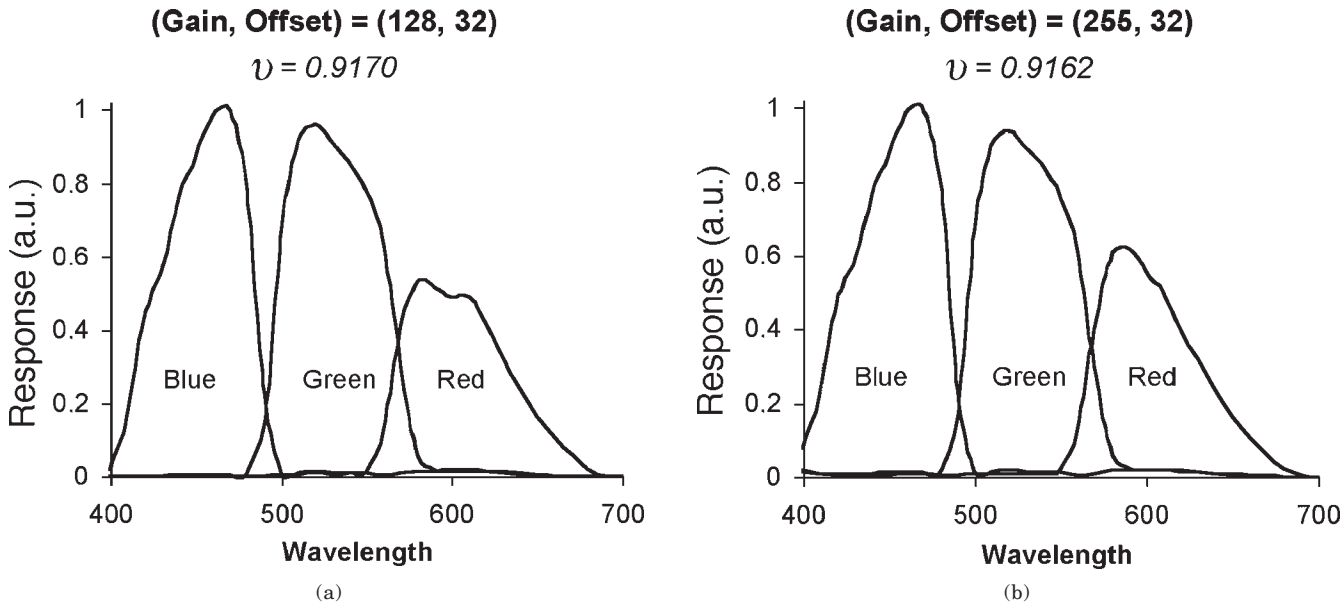

Figure 4. Spectral responsivities of the SONY DX-9100P camera for the (gain, offset) values: (a) (128, 32), and (b) (255, 32).

responsitivity functions were measured by applying the classical technique based on stimulating the camera sensors with a very narrow band illumination generated by a light source and a monochromator. We calculated the factor ν associated to each set of RGB spectral responsivity curves[12] and values > 0.9 were only reached for the pairs (gain,offset) = {(128,32),(255,32)} that yield very close ν values. These spectral responsitivities are represented in Fig. 4. We prefer the RGB responsitivity functions obtained setting (gain,offset) = (255,32), with ν = 0.9162, because the shape of the R sensitivity function is slightly smoother than the corresponding to (gain, offset) = (128, 32).

Regarding the influence of imaging noise in our measurements, we examined dark noise and shot noise among the different noise sources. Dark noise is a signal independent noise, and it can be estimated from the signal fluctuations in the absence of light exposure. In our case, when the offset value was set equal to zero, the dark noise in the three R, G, B components was characterized by non zero mean values (14 for the B channel and 15 for the G and R channels) and a similar variance σ_d^2 (Fig. 5). By setting the offset value equal to 32, however, we compensated for the uniform constant of the dark noise and obtained a nearly zero mean distribution. This result for the dark level reveals a physically meaningful characteristic of the camera and clarifies our final selection of the offset = 32. Shot noise is a signal dependent noise, and it can be estimated from the signal variations corresponding to a series of different signal levels. The coefficient k associated to shot noise can be obtained by fitting Eq. (1), where noise levels can be represented by digital counts normalized to the digital count of maximal signal. To estimate the parameters of noise model for the camera capturing with (gain, offset) = (255,32), we captured multiple images of the white standard plate, uniformly illuminated, with different apertures of the camera lens (including total occlusion). The apertures producing saturation were excluded. In this simple way, we had a variation in the signal level without affecting other acquisition condi-

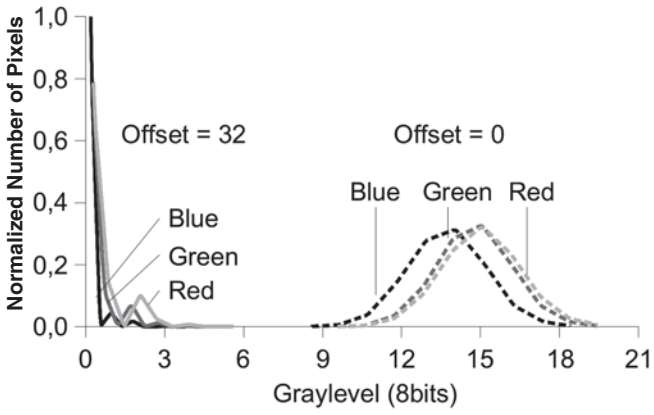

Figure 5. Effects of the offset setting on the dark noise level measured in the R, G, B components of an image captured in absence of light exposure: offset = 0 (dashed lines), offset = 32 (solid lines).

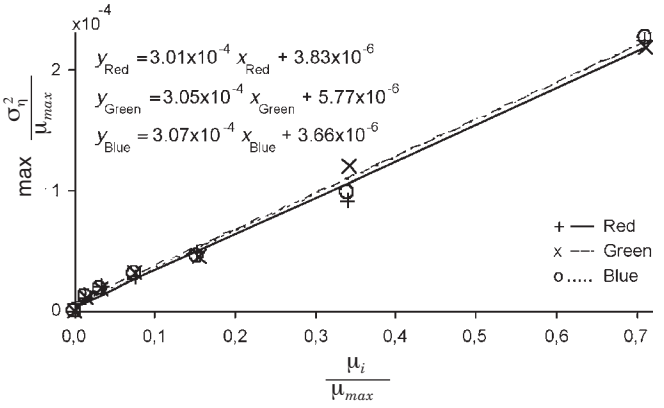

Figure 6. Imaging noise model of the 3CCD camera with contributions of the dark and shot noise. Experimental points and linear fits are given for the R, G, B channels.

tions. The variances of the RGB components of the captured images were calculated. Figure 6 shows the experimental points and the results of fitting Eq. (1) in the R, G, B channels of the camera. The three channels obtained very close linear fits. The coefficients k associated to shot noise were (k_R,k_G,k_B) = 3.011, 3.048, 3.073) × 10^{-4}. Since they are very close in the three channels, we used the average value k = 3.044 × 10^{-4}. The dark noise variances were $(\sigma^2_{dR},\sigma^2_{dG},\sigma^2_{dB})$ = (3.8, 5.8, 3.7) × 10^{-6} and the correlation coefficients of the fits (r_R,r_G,r_B) = (0.995, 0.997, 0.997) were acceptable.

Following the procedure outlined in Refs. 24 and 25, we calculated the coefficients of the linear transform to pass from the RGB device dependent values to the XYZ tristimulus values. Taking into account the camera spectral sensitivities (CSS) for the pair (gain, offset) = (255, 32), the spectral power distribution of the D65 simulator, and the standard observer responses, we computed the coefficients of the linear transform and obtained

$$\begin{pmatrix} X \\ Y \\ Z \end{pmatrix} = \begin{vmatrix} 1.947 & 0.237 & 0.373 \\ 1.155 & 1.000 & 0.103 \\ 0.062 & 0.112 & 2.179 \end{vmatrix}_{CSS} \cdot \begin{pmatrix} R \\ G \\ B \end{pmatrix}. \quad (4)$$

From the XYZ values, the CIELAB coordinates L^* a^* b^* are calculated using the CIE 1976 formula.[16,17] As white reference for this calculation we used the X_n, Y_n and Z_n obtained for the standard reflectance plate Photoresearch RS-3.

We measured the CIELAB coordinates of a gray scale using the camera with (gain, offset) = (255, 32). We compared the camera response with the measurements obtained by a spectroradiometer (see Figs. 5 through 7 in Ref. 11) and they nearly coincided in the measurement of L^* over the whole range of grayscale. They were also close in the measurement of low chromaticities C^*_{ab} for bright neutral chips, but the camera measured higher chromaticity values for dark gray chips that might be due to higher dark current effects. In comparison with other gain and offset pairs, the response of the camera with (gain, offset) = (255, 32) provided the CIELAB measurements closest to those obtained by the spectroradiometer.

The uncertainties associated with the measurement process, expressed as MCDM and calculated following the procedure outlined above, are 0.025 ΔE^*_{ab} in CIELAB (0.020 ΔE_{00} in CIEDE2000) for the spectroradiometer, and 0.5 ΔE^*_{ab} in CIELAB (0.020 ΔE_{00} in CIEDE2000) for the camera working with (gain,offset) = (255,32). Accordingly, the instrumental color tolerances are 0.25 ΔE^*_{ab} (0.20 ΔE_{00}) for the spectroradiometer and 0.5. ΔE^*_{ab} (0.6 ΔE_{00}) for the camera.

So far, the calculations to measure the CIELAB coordinates from the camera RGB values and the measure of goodness of the system do not consider the imaging noise characterization of the camera. In this article, taking into account the Unified Measure of Goodness (UMG) proposed by Quan et al.,[13] we have alternatively computed the coefficients of the linear matrix converting camera RGB to CIE XYZ. This linear transform is obtained through the minimization of noise propagation. The noise model assumed in Ref. 13 is zero mean and the noise variance has the main contributions of dark and shot noises. The UMG metrics minimizes the average color difference or error for an ensemble of standard reflectance samples in a perceptually uniform color space. As representative ensemble of standard object reflectance spectra we took Hardeberg's[28] optimal set consisting of 20 Munsell patches distributed approximately uniformly in the (a^*, b^*) plane (Table I). In addition to the measured spectral reflectance of each sample of the set, we took into account the following data to calculate the coefficients of the linear matrix: the spectral sensitivity curves of the camera, the imaging noise characterization (dark current variances and k coefficient associated to shot noise), the spectral power distribution of the recording and viewing illuminant given by the D65 simulator (Fig. 3), the CIE color matching functions. We completed the UMG computing procedure (see Ref. 13 for details), which requires much more computation than the Vora–Trussell's ν factor, and obtained the following results:

- The linear transform is

$$\begin{pmatrix} X \\ Y \\ Z \end{pmatrix} = \begin{bmatrix} 1.761 & 0.319 & 0.206 \\ 0.867 & 1.139 & 0.003 \\ -0.075 & 0.009 & 1.886 \end{bmatrix}_{UMG} \cdot \begin{pmatrix} R \\ G \\ B \end{pmatrix}. \quad (5)$$

- The minimal color error for the ensemble in CIELAB units is $\varepsilon_{\min}$ = 1.423,
- And the UMG value is θ = 0.899.

Note that the UMG value (θ = 0.899) is lower than the ν factor (ν = 0.9162). Since noise effects are also considered in UMG, it gives a more complete measure of goodness of the camera and, consequently, its value is lower than the ν factor, which exclusively characterizes the deviation from the human color subspace (given by the CIE color matching functions). Using the linear transform of Eq. (5), we can calculate the XYZ, and hence, the CIELAB coordinates from some given RGB values provided by the camera.

Although we are more interested in color differences between sample pairs rather than in the absolute measurement of color, we briefly report on what the color fidelity of the camera estimates are. Figure 7 shows the a^*b^* plane with the points corresponding to the CIELAB cromaticities of the Munsell group center patches of the very pale and dark grayish sets measured by the spectroradiometer, and by the 3CCD camera with the linear transforms given by either Eq. (4) or Eq. (5). The mean color differences between the camera estimated CIELAB values and the spectroradiometer CIELAB measured values were calculated for the entire 90 samples of the very pale test plus the 70 samples of the dark grayish test, and they are contained in Table II. The results are quite close for the two sets and also for the two linear transforms. They reveal that the color fidelity of the camera estimates is limited by an average error of 7 CIELAB units. Although the UMG based linear transform leads to a mean color difference (or error) slightly higher than the CSS based linear transform (about 1 CIELAB or CIEDE2000 unit higher), the

TABLE I. Hardeberg's Optimal Set of Munsell Patches (see Ref. 28)

Hardeberg's optimal set of 20 Munsell patches[28]			
7.5RP9/2	10R7/12	10B6/10	7.5PB5/12
5R4/14	7.5RP6/10	10Y8/4	10Y8.5/6
7.5Y8/12	2.5B5/8	7.5YR8/8	10PB4/10
2.5G7/10	10P3/8	10RP8/6	10YR3/1
5P2.5/6	7.5R7/4	10R3/2	7.5YR6/4

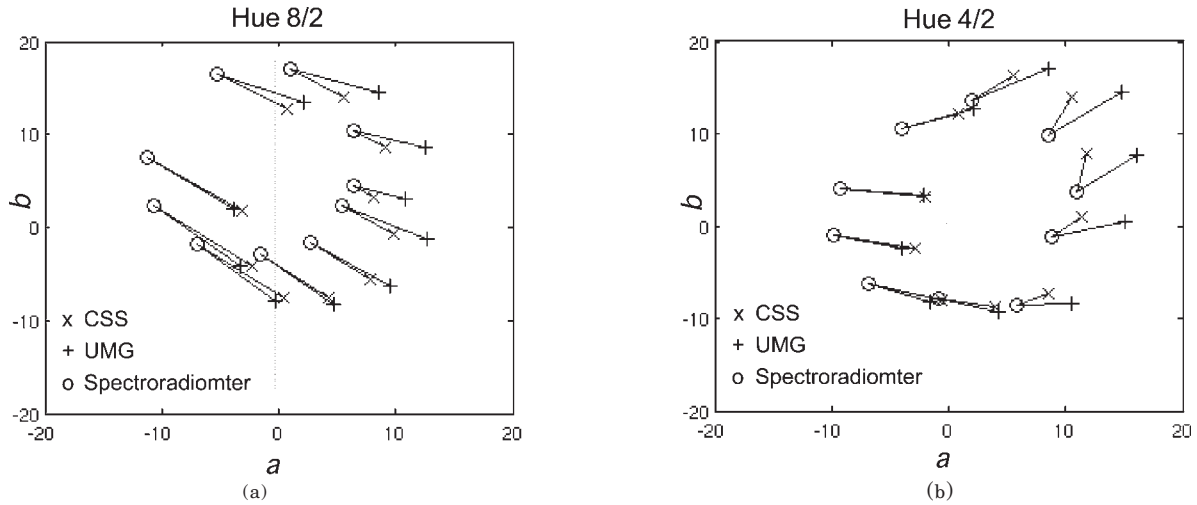

Figure 7. Chromaticity plane showing the CIELAB a^*b^* values of the Munsell group center patches measured by the spectroradiometer, and by the 3CCD camera with the linear transforms given by either Eq. (4) (CSS) or Eq. (5) (UMG). (a) Very pale set, (b) dark grayish set.

TABLE II. Statistics of the Color Differences Calculated between the Camera Estimated CIELAB Values and the Spectroradiometer Measured CIELAB Values for Each Patch of Both the Very Pale and the Dark Grayish Set. The Camera CIELAB Values were Computed using Two Different Linear Transforms: The Matrix with Subindex CSS (Eq. (4)), and the Matrix with Subindex UMG (Eq. (5)).

	Color differences tha camera estimated and the spectroradiometers mesured CIELAB values					
	Very Pale		Dark Grayish		Mean	
CIELAB	CSS	UMG	CSS	UMG	CSS	UMG
Mean $\left(\overline{\Delta E^*_{ab}}\right)$	6.29	7.40	5.96	6.78	6.13	7.09
std. dev (σ)	2.33	1.43	1.70	0.99	2.02	1.21
Max $\left(\left\{\Delta E^*_{ab}\right\}_{max}\right)$	10.48	9.99	9.87	9.35		
MIn $\left(\left\{\Delta E^*_{ab}\right\}_{min}\right)$	1.19	3.70	3.38	5.06		
CIEDE2000						
Mean $\left(\overline{\Delta E_{00}}\right)$	7.25	8.50	6.68	7.61	6.97	8.06
std. dev (σ)	2.85	1.75	2.40	1.63	2.63	1.69
Max $\left(\left\{\Delta E_{00}\right\}_{max}\right)$	11.60	11.46	11.95	13.30		
Min $\left(\left\{\Delta E_{00}\right\}_{min}\right)$	*0.90*	*3.84*	*3.14*	*4.60*		

dispersion is lower. This means that the CSS based linear transform leads to slightly more accurate results whereas the UMG based linear transform leads to slightly more precise results.

Using the test of very pale and dark grayish color patches of Fig. 2, we measured the color differences between each group center and its neighbors by both the reference instrument and the camera. The linear transforms from RGB to XYZ values, given by Eqs. (4) and (5), were separately taken into account to calculate the camera based color differences. Figure 8 shows the CIEDE2000 color differences ΔE_{00} between the very pale Munsell patches. Each diagram corresponds to a given Munsell variation from the group center, e.g., +0.5 Value, –2.5 Hue, +1.0 Chroma, etc. From the results, it can be said that the camera (for both linear transforms) and the reference instrument show a high degree of agreement in the estimation of the color differences between very pale patches. Looking at the diagrams in detail, we can see that the highest coincidence is obtained in the estimation of the color differences corresponding to ± 0.5 variations in the Munsell Value. Figure 9 shows the CIEDE2000 color differences ΔE_{00} between the dark grayish Munsell patches. Again, the diagrams show a good agreement between color differences measured by the spectroradiometer and the camera (for both linear transforms).

We have calculated the absolute discrepancies D_i (Eq. (2)) between the measurements obtained by both instruments for the very pale test (Table III) and the dark grayish test (Table IV). The mean values of the absolute discrepancies corresponding to each color variation are calculated in Tables III and IV. These mean values of the absolute discrepancy exceed the camera uncer-

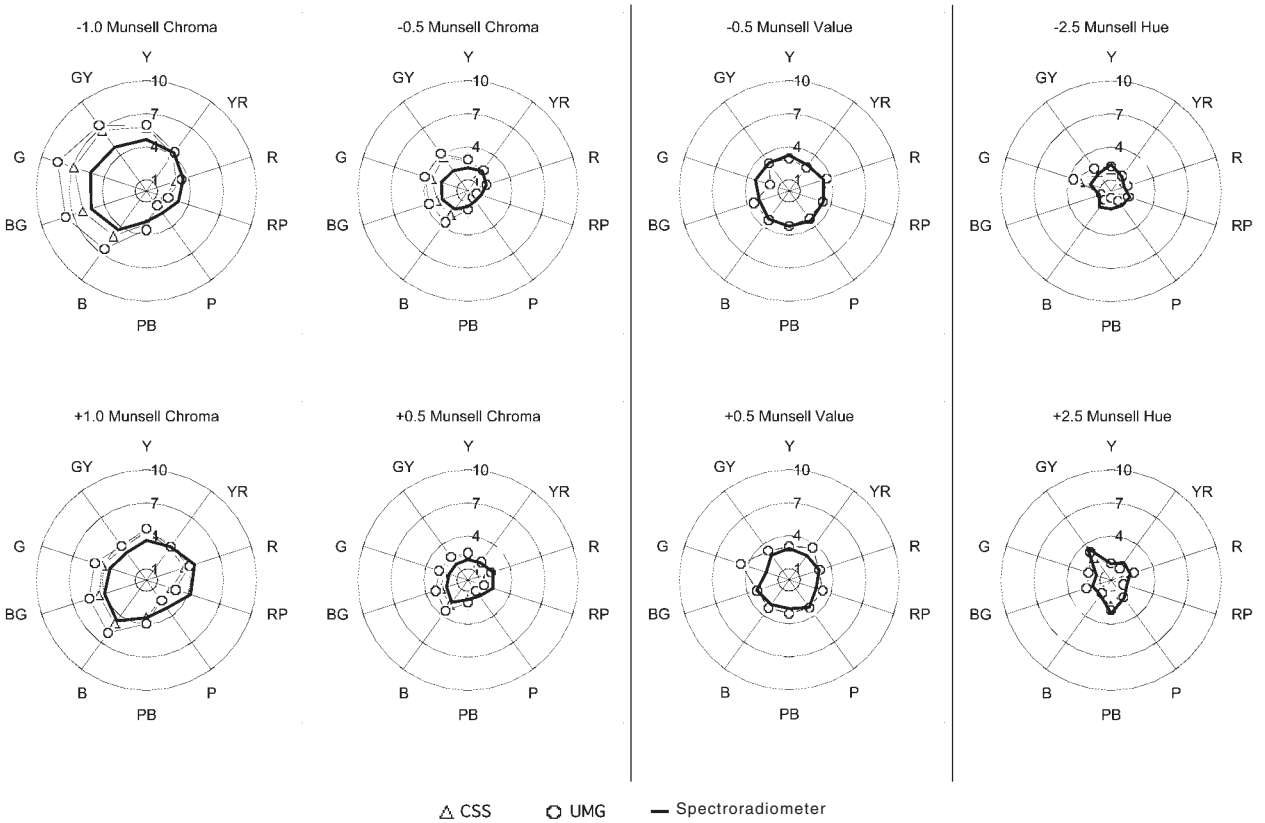

Figure 8. CIEDE2000 color differences ΔE_{00} between each group center and its neighbors in the very pale set of Munsell patches (Fig. 2(a)). ΔE_{00} are calculated from the measurements obtained by the spectroradiomenter and by the camera using either the CSS or the UMG linear transforms. The Munsell color variations concerned are: ±1.0 and ±0.5 Chroma, ±0.5 Value, and ±2.5 Hue.

tainty in general. However, in the case of the very pale subset, most of them fall in the camera tolerance (either 0.5 ΔE^*_{ab} or 0.6 ΔE_{00}). This fact, along with the magnitude of the camera tolerance, can be considered a good achievement for the camera's performance. In the case of the dark grayish subset, whose color variations in Value and Chroma are also bigger, the absolute discrepancies are somewhat higher, and correspond to a much lower stimulation of the instrument sensors and a greater influence of dark current. If we consider the minimal color error calculated with the UMG approach for Hardeberg's ensemble (ε_{min} = 1.423 CIELAB units) as another reference for comparison, nearly all the absolute discrepancies calculated with the UMG matrix are lower than it.

We have calculated the relative discrepancies D_i^r (Eq. (3)) to further analyze the uniformity of the camera performance. Tables V and VI contain the results for the very pale and the dark grayish tests, respectively. In Tables V and VI, we have calculated the mean value of the (CSS or UMG) relative discrepancies aligned on the same row, i.e., corresponding to a given group center, and also the mean value of the relative discrepancies aligned on the same column, i.e., corresponding to a given color variation. These mean values, calculated using CIELAB and CIEDE2000 metrics, are graphed in Figs. 10 and 11. From Fig. 10, the relative discrepancies are low and quite uniform around the circle of hue in both the very pale and the dark grayish regions. This fact also reveals a good property of the camera performance. In Fig. 10, the values calculated using CIEDE2000 and graphed in Fig. 10(a) lead to similar comments to those calculated using CIELAB and graphed in Fig. 10(b). Also the values calculated using either the CSS or the UMG linear transform lead to close graphs in Fig. 10. In Fig. 11, we observe again that the relative discrepancies are low in the evaluation of the color variations of the Munsell components. It can be appreciated that relative discrepancies are slightly higher in the evaluation of Munsell Hue variations than for Munsell Value variations. This is common for both color regions considered, the very pale (Figs. 11(a) and 11(b)) and the dark grayish (Figs. 11(c) and 11(d)). Slight differences in the estimation of small chroma variations (less than ±1.0 Munsell Chroma) can be appreciated depending on the use of CIEDE2000 or CIELAB. In such a case, CIEDE2000 formula tends to be more sensitive and makes the relative discrepancy between the camera and the reference instrument measurements higher than CIELAB formula.

The results shown in Figs. 8 through 11 and Table III through Table VI, computed from the camera estimated XYZ values using either the linear transform of Eq. (4) (matrix with subindex CSS) or Eq. (5) (matrix with subindex UMG), are very close each other, and do not allow us to extract any conclusion about the advantages of

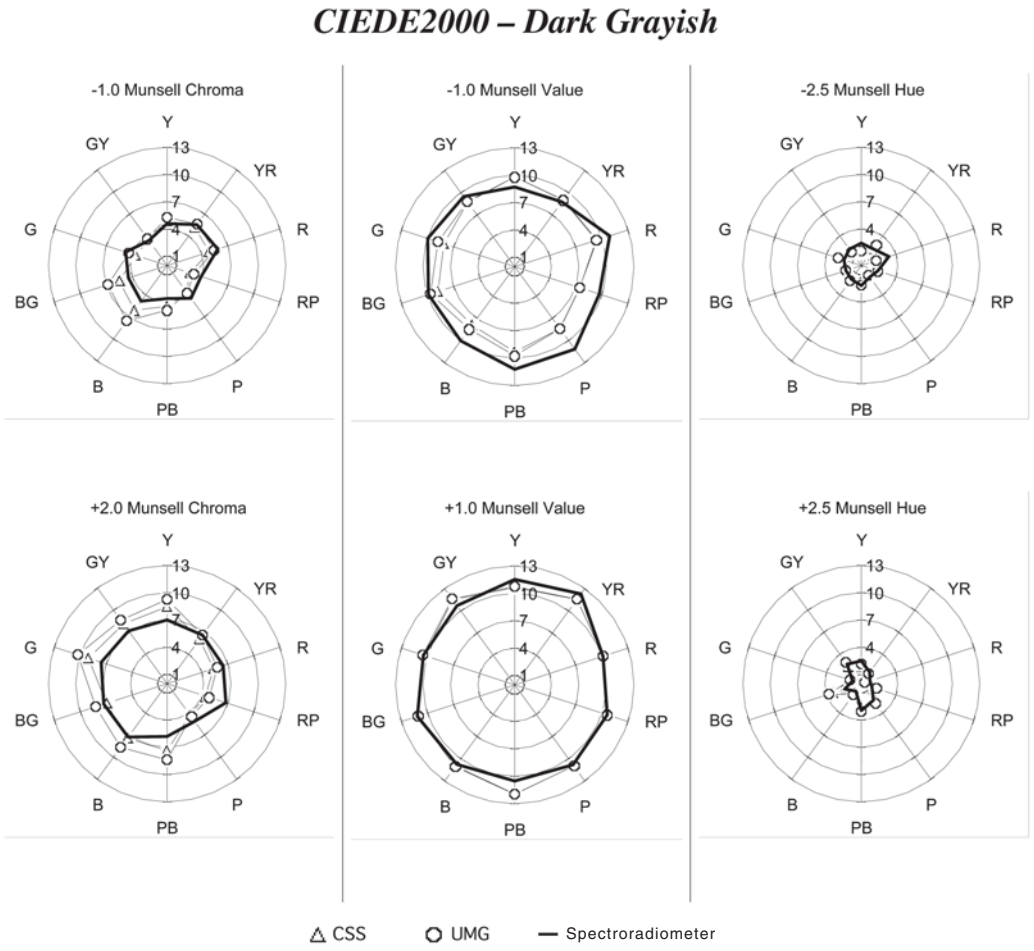

Figure 9. CIEDE2000 color differences ΔE_{00} between each group center and its neighbors in the dark grayish set of Munsell patches (Fig. 2(b)). ΔE_{00} are calculated from the measurements obtained by the spectroradiomenter and by the camera using either the CSS or the UMG linear transforms. The Munsell color variations concerned are: –1.0 and +2.0 Chroma, ±1.0 Value, and ±2.5 Hue.

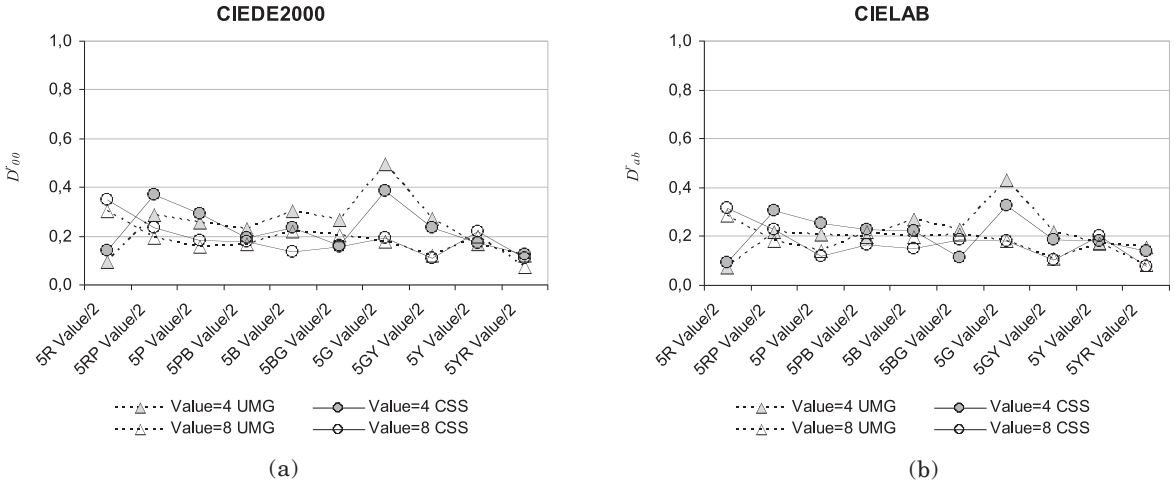

Figure 10. Mean relative discrepancies between the camera and the spectroradiometer around the circle of Hue using: (a) CIEDE2000 metric, and (b) CIELAB metric. The data represented are contained in Tables V and VI. The graphs labeled with V = 8 corresponds to the very pale test, whereas V = 4 corresponds to the dark grayish test. CSS and UMG have the same meaning as in previous figures.

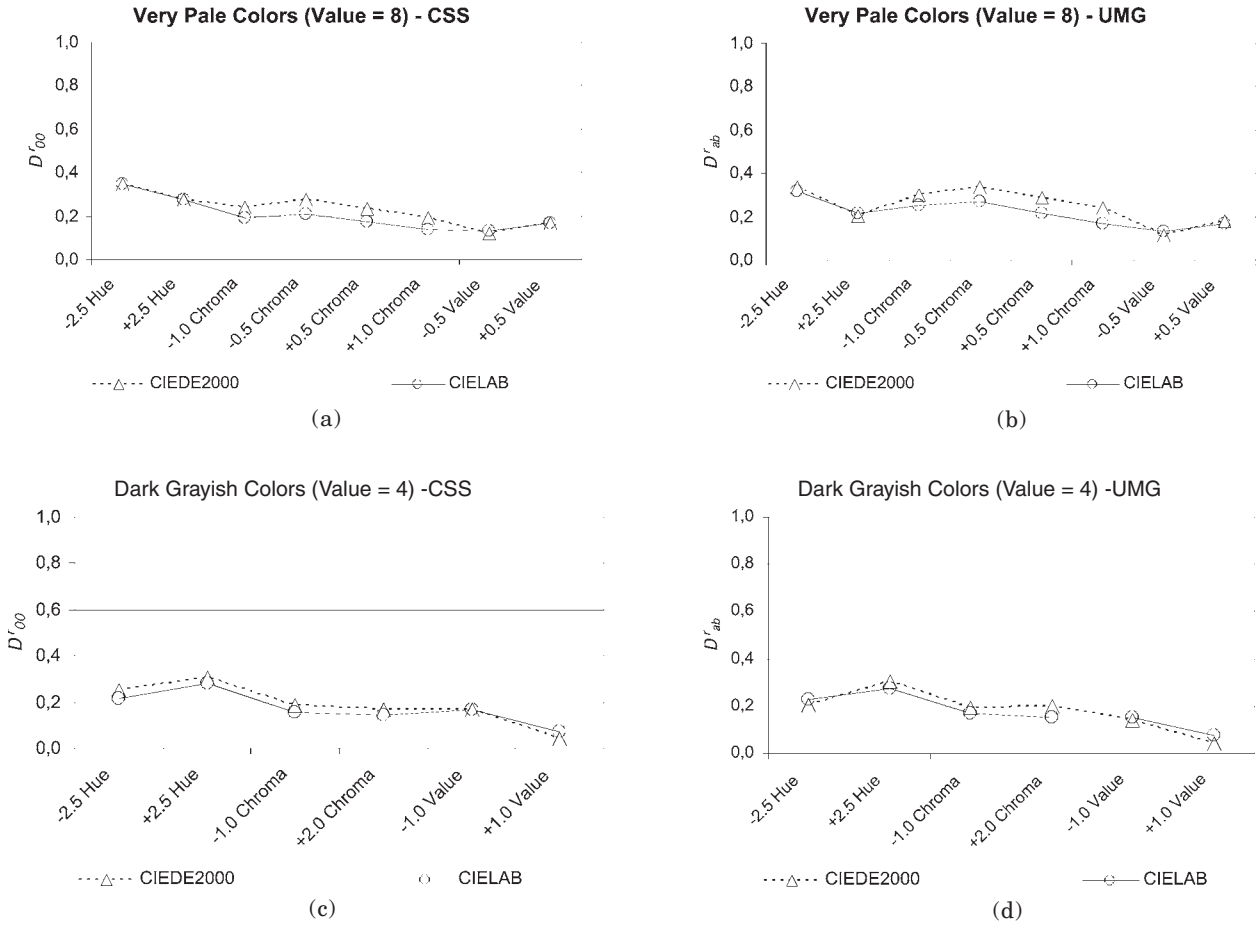

Figure 11. Mean relative discrepancies between the camera and the spectroradiometer versus the Munsell color variations of Hue, Chroma and Value: (a)-(b) for the very pale test, and (c)-(d) for the dark grayish test. The data represented are contained in Tables V and VI.

using one of them in particular. This fact means that the effects of the sources of imaging noise considered in our experiment do not significantly alter the color difference measurements.

Application: Evaluation of Color Uniformity in Textile Dying

From the results obtained above, we consider that the camera system has promising characteristics for objective and automatic inspection of color matching. For this reason, we have applied this system to the evaluation of color uniformity in textile dying. A common task in inspection of textile color is the comparison between the center and both the left and right extremes of the usable width of a fabric piece (usually 150 cm). This is known as extreme-center color matching. The assessment may be repeated several times along the fabric length to evaluate the color uniformity of a piece. An extreme-center sample pair consists of an extreme sample, from either the left or the right side of the fabric piece, sewn side by side, to a sample taken from the central part of the fabric piece. Commonly, the color difference between them is visually estimated by an expert. If the color difference of the extreme-center samples is visually perceived, then the fabric is rejected. Two extreme-center sample pairs, i.e., the left center sample pair and the right center sample pair, are always assessed together at a given length of the fabric piece. This inspection of the fabric quality is difficult to carry out and requires trained vision in color evaluation. Frequently, the standard of quality in the textile industry is very high, but it is difficult to apply because, in addition, the samples to compare are often of unsaturated dark colors, e.g., fabrics for men's suits, and may show very subtle color differences, and may involve texture effects, etc.

In this application, assessing textile samples is more complex than Munsell chips because the structure of the woven fabric adds texture to the colored sample. We have applied our camera vision system to assess eight extreme-center sample pairs of cloths of navy, blue, black and green colors in the dark grayish region. They are also assessed using the spectroradiometer as a reference instrument.

Because the fabric samples are textured, we have first analyzed their variability expressed as MCDM in CIEDE2000. We have calculated the MCDM from the measurements obtained by the spectroradiometer and the camera at ten different positions of each side, named A and B, of every extreme-center sample pair. In the case of the camera measurements, as was already stated above, each individual measurement (L_i^*, a_i^*, b_i^*) at a given position is, in turn, the average CIELAB values of the CIELAB values of each of the 300 × 300 pixels

TABLE III. Absolute Discrepancy between the Measurements of the Color Difference Obtained by the Camera and by the Spectroradiometer for the Very Pale Subset Test.

D_{00} CIEDE2000

Group Center	-2.5 Hue		+2.5 Hue		-1.0 Chroma		-0.5 Chroma		+0.5 Chroma		+1.0 Chroma		-0.5 Value		+0.5 Value		Mean	
	CSS	UMG	CSS	UMG	CSS	UMG	CSS	UMG	CSS	UMG	CSS	UMG	CSS	UMG	CSS	UMG	CSS	UMG
5R 8/2	0.331	0.320	0.111	0.355	0.663	0.160	0.234	0.023	0.439	0.174	0.918	0.475	0.218	0.312	0.038	0.005	0.369	0.228
5RP 8/2	0.171	0.173	0.464	0.335	1.326	1.036	0.574	0.462	1.060	0.858	1.825	1.481	0.095	0.041	0.596	0.626	0.764	0.627
5P 8/2	0.586	0.537	0.402	0.086	0.869	0.848	0.401	0.391	0.606	0.576	0.915	0.850	0.272	0.225	0.015	0.059	0.508	0.447
5PB 8/2	1.060	0.987	0.722	0.295	0.221	0.705	0.025	0.266	0.024	0.270	0.037	0.538	0.051	0.025	0.410	0.458	0.319	0.443
5B 8/2	0.984	0.801	0.524	0.252	0.681	2.152	0.654	1.430	0.320	0.969	0.321	1.372	0.052	0.064	0.355	0.405	0.486	0.931
5BG 8/2	0.209	0.158	0.424	0.622	0.785	2.440	0.486	1.237	0.491	1.040	0.504	1.440	0.577	0.570	0.046	0.021	0.440	0.941
5G 8/2	0.968	1.609	0.668	0.747	1.558	3.127	0.909	1.581	0.521	0.953	0.771	1.496	1.465	1.397	2.458	2.437	1.165	1.668
5GY 8/2	0.268	0.638	1.052	0.438	1.903	2.450	1.484	1.909	0.604	0.786	0.512	0.743	0.027	0.030	0.442	0.504	0.786	0.937
5Y 8/2	0.461	0.178	0.107	0.045	1.125	1.314	0.643	0.750	0.493	0.608	0.841	1.071	0.296	0.288	0.148	0.174	0.514	0.553
5YR 8/2	0.039	0.069	0.693	0.687	0.227	0.110	0.068	0.070	0.053	0.146	0.175	0.026	0.268	0.250	0.896	0.928	0.302	0.286
Mean	0.508	0.547	0.517	0.386	0.936	1.434	0.548	0.812	0.461	0.638	0.682	0.949	0.332	0.320	0.540	0.562		

D_{ab} CIELAB

Group Center	-2.5 Hue		+2.5 Hue		-1.0 Chroma		-0.5 Chroma		+0.5 Chroma		+1.0 Chroma		-0.5 Value		+0.5 Value		Mean	
	CSS	UMG	CSS	UMG	CSS	UMG	CSS	UMG	CSS	UMG	CSS	UMG	CSS	UMG	CSS	UMG	CSS	UMG
5R 8/2	0.363	0.415	0.112	0.336	0.295	0.021	0.093	0.076	0.161	0.055	0.399	0.026	0.255	0.332	0.131	0.109	0.226	0.171
5RP 8/2	0.214	0.160	0.179	0.096	0.777	0.567	0.365	0.276	0.734	0.549	1.354	1.009	0.083	0.048	0.921	0.930	0.578	0.454
5P 8/2	0.664	0.620	0.434	0.132	0.613	0.557	0.285	0.259	0.480	0.431	0.801	0.702	0.394	0.357	0.035	0.001	0.463	0.382
5PB 8/2	0.990	0.949	0.677	0.377	0.229	0.570	0.078	0.079	0.141	0.011	0.350	0.077	0.212	0.200	0.638	0.681	0.414	0.368
5B 8/2	0.816	0.706	0.541	0.346	0.380	1.185	0.307	0.731	0.038	0.488	0.141	0.656	0.125	0.125	0.364	0.411	0.339	0.581
5BG 8/2	0.276	0.235	0.209	0.423	0.333	1.389	0.205	0.712	0.264	0.672	0.000	0.835	0.591	0.575	0.329	0.261	0.276	0.638
5G 8/2	0.479	0.860	0.687	0.764	0.857	1.829	0.495	0.882	0.233	0.585	0.276	0.973	2.427	2.362	3.548	3.517	1.125	1.471
5GY 8/2	0.010	0.249	1.051	0.749	1.238	1.696	0.879	1.183	0.434	0.563	0.374	0.530	0.191	0.197	0.462	0.518	0.580	0.711
5Y 8/2	0.527	0.208	0.325	0.251	0.910	1.179	0.525	0.644	0.378	0.486	0.656	0.862	0.559	0.565	0.114	0.133	0.499	0.541
5YR 8/2	0.143	0.021	0.631	0.604	0.318	0.573	0.163	0.273	0.133	0.222	0.007	0.202	0.485	0.486	1.386	1.400	0.408	0.473
Mean	0.448	0.442	0.485	0.408	0.595	0.957	0.339	0.512	0.300	0.406	0.436	0.587	0.532	0.525	0.793	0.796		

TABLE IV. Absolute Discrepancy between the Measurements of the Color Difference Obtained by the Camera and by the Spectroradiometer for the Dark Grayish Subset Test

D_{00} CIEDE2000

Group Center	-2.5 Hue		+2.5 Hue		-1.0 Chroma		+2.0 Chroma		-1.0 Value		+1.0 Value		Mean	
	CSS	UMG	CSS	UMG	CSS	UMG	CSS	UMG	CSS	UMG	CSS	UMG	CSS	UMG
5R 4/2	1.539	1.468	0.633	0.607	0.984	0.412	1.112	0.683	1.435	1.567	0.041	0.021	0.957	0.793
5RP 4/2	0.027	0.000	0.442	0.466	1.283	0.831	2.367	1.931	2.254	2.233	0.028	0.001	1.067	0.910
5P 4/2	0.409	0.235	0.229	0.447	0.833	0.732	0.864	0.640	2.776	2.753	0.155	0.156	0.878	0.827
5PB 4/2	0.404	0.038	0.318	0.120	0.852	1.272	1.545	2.568	1.895	1.487	1.425	1.443	1.073	1.155
5B 4/2	0.180	0.218	0.243	0.488	1.226	2.678	0.149	1.394	2.136	1.584	0.229	0.331	0.694	1.115
5BG 4/2	0.036	0.027	1.344	1.822	1.057	2.359	0.305	0.931	1.092	0.221	0.119	0.048	0.659	0.901
5G 4/2	0.572	0.675	0.275	0.292	1.167	0.354	1.463	2.682	1.855	1.177	0.129	0.062	0.910	0.874
5GY 4/2	0.522	0.408	0.254	0.233	0.059	0.277	0.949	1.457	0.760	0.684	0.803	0.913	0.558	0.662
5Y 4/2	1.032	0.863	0.650	0.329	0.393	0.684	1.460	2.257	1.105	1.099	0.889	0.783	0.922	1.003
5YR 4/2	0.427	0.510	0.310	0.213	0.383	0.069	0.555	0.006	0.276	0.247	0.747	0.725	0.449	0.295
Mean	0.515	0.444	0.470	0.502	0.824	0.967	1.077	1.455	1.558	1.305	0.457	0.448		

D_{ab} CIELAB

Group Center	-2.5 Hue		+2.5 Hue		-1.0 Chroma		+2.0 Chroma		-1.0 Value		+1.0 Value		Mean	
	CSS	UMG	CSS	UMG	CSS	UMG	CSS	UMG	CSS	UMG	CSS	UMG	CSS	UMG
5R 4/2	1.677	1.584	0.660	0.630	0.164	0.168	0.698	0.076	1.315	1.339	0.431	0.550	0.824	0.725
5RP 4/2	0.014	0.048	0.556	0.612	0.747	0.301	2.294	1.639	2.409	2.283	0.446	0.611	1.077	0.916
5P 4/2	0.037	0.190	0.431	0.659	0.131	0.076	0.667	0.356	2.983	2.879	0.801	0.925	0.842	0.848
5PB 4/2	0.021	0.263	0.343	0.557	1.019	1.332	1.233	1.650	2.296	1.998	2.078	2.147	1.165	1.324
5B 4/2	0.478	0.534	0.072	0.091	1.081	1.770	0.044	1.049	2.547	2.233	1.010	1.099	0.872	1.129
5BG 4/2	0.084	0.023	1.022	1.323	0.897	1.627	0.890	0.432	1.622	1.111	0.724	0.754	0.873	0.878
5G 4/2	0.542	0.660	0.241	0.263	0.942	0.395	0.559	1.899	2.207	1.811	0.515	0.645	0.834	0.945
5GY 4/2	0.585	0.492	0.166	0.111	0.021	0.200	0.835	1.291	0.293	0.217	1.376	1.463	0.546	0.629
5Y 4/2	0.594	0.441	0.410	0.109	0.346	0.598	1.957	2.942	2.022	2.075	0.474	0.325	0.967	1.081
5YR 4/2	0.485	0.605	0.119	0.014	0.122	0.449	0.310	0.395	0.688	0.725	0.288	0.134	0.335	0.387
Mean	0.452	0.484	0.402	0.437	0.547	0.692	0.949	1.173	1.838	1.667	0.814	0.865		

TABLE V. Relative Discrepancy between the Measurements of the Color Difference Obtained by the Camera and by the Spectroradiometer for the Very Pale Subset Test

D^{r}_{00} *CIEDE2000*

Group	-2.5 Hue		+2.5 Hue		-1.0 Chroma		-0.5 Chroma		+0.5 Chroma		+1.0 Chroma		-0.5 Value		+0.5 Value		Mean	
Center	CSS	UMG	CSS	UMG	CSS	UMG	CSS	UMG	CSS	UMG	CSS	UMG	CSS	UMG	CSS	UMG	CSS	UMG
5R 8/2	0.232	0.225	0.059	0.177	0.208	0.046	0.143	0.013	0.203	0.076	0.222	0.109	0.064	0.090	0.013	0.002	0.143	0.092
5RP 8/2	0.100	0.102	0.363	0.250	0.553	0.407	0.593	0.452	0.569	0.437	0.551	0.425	0.030	0.013	0.207	0.216	0.371	0.288
5P 8/2	0.437	0.394	0.221	0.044	0.426	0.414	0.431	0.419	0.408	0.384	0.341	0.314	0.085	0.069	0.005	0.019	0.294	0.257
5PB 8/2	0.992	0.894	0.271	0.103	0.076	0.224	0.018	0.171	0.014	0.142	0.011	0.146	0.016	0.008	0.145	0.160	0.193	0.231
5B 8/2	0.771	0.586	0.372	0.163	0.145	0.395	0.276	0.518	0.121	0.326	0.068	0.262	0.016	0.020	0.120	0.136	0.236	0.301
5BG 8/2	0.212	0.156	0.215	0.300	0.139	0.376	0.180	0.401	0.215	0.407	0.119	0.306	0.184	0.182	0.015	0.007	0.160	0.267
5G 8/2	0.394	0.580	0.386	0.422	0.255	0.453	0.304	0.476	0.253	0.419	0.200	0.355	0.590	0.554	0.719	0.715	0.388	0.497
5GY 8/2	0.129	0.282	0.341	0.129	0.325	0.400	0.493	0.593	0.287	0.358	0.154	0.216	0.009	0.010	0.149	0.168	0.236	0.269
5Y 8/2	0.211	0.077	0.075	0.030	0.215	0.247	0.267	0.304	0.233	0.280	0.209	0.259	0.096	0.093	0.051	0.059	0.170	0.169
5YR 8/2	0.023	0.041	0.425	0.420	0.055	0.025	0.031	0.031	0.027	0.072	0.048	0.007	0.098	0.091	0.282	0.291	0.124	0.122
Mean	0.350	0.333	0.273	0.204	0.240	0.299	0.274	0.338	0.233	0.290	0.192	0.240	0.119	0.113	0.171	0.177		

D^{r}_{ab} *CIELAB*

Group	-2.5 Hue		+2.5 Hue		-1.0 Chroma		-0.5 Chroma		+0.5 Chroma		+1.0 Chroma		-0.5 Value		+0.5 Value		Mean	
Center	CSS	UMG	CSS	UMG	CSS	UMG	CSS	UMG	CSS	UMG	CSS	UMG	CSS	UMG	CSS	UMG	CSS	UMG
5R 8/2	0.233	0.262	0.051	0.146	0.122	0.008	0.072	0.055	0.086	0.028	0.106	0.007	0.052	0.067	0.030	0.025	0.094	0.075
5RP 8/2	0.110	0.081	0.162	0.083	0.439	0.302	0.500	0.356	0.494	0.347	0.496	0.348	0.018	0.010	0.212	0.214	0.304	0.218
5P 8/2	0.417	0.385	0.255	0.071	0.317	0.284	0.320	0.287	0.334	0.295	0.300	0.258	0.085	0.077	0.007	0.000	0.255	0.207
5PB 8/2	0.983	0.924	0.308	0.160	0.087	0.203	0.058	0.056	0.085	0.006	0.106	0.022	0.046	0.044	0.154	0.163	0.228	0.197
5B 8/2	0.835	0.684	0.500	0.293	0.111	0.311	0.176	0.373	0.018	0.206	0.035	0.149	0.027	0.028	0.083	0.093	0.223	0.267
5BG 8/2	0.271	0.226	0.114	0.219	0.085	0.314	0.104	0.321	0.145	0.332	0.000	0.215	0.132	0.128	0.073	0.057	0.116	0.227
5G 8/2	0.206	0.341	0.359	0.392	0.199	0.381	0.224	0.368	0.141	0.319	0.086	0.272	0.687	0.663	0.690	0.686	0.324	0.428
5GY 8/2	0.005	0.120	0.422	0.284	0.255	0.333	0.345	0.438	0.209	0.262	0.110	0.152	0.042	0.044	0.105	0.117	0.187	0.219
5Y 8/2	0.321	0.115	0.230	0.173	0.195	0.245	0.233	0.278	0.177	0.222	0.155	0.199	0.124	0.126	0.026	0.030	0.183	0.174
5YR 8/2	0.090	0.012	0.364	0.346	0.090	0.157	0.083	0.135	0.068	0.110	0.002	0.053	0.121	0.121	0.291	0.293	0.139	0.153
Mean	0.347	0.315	0.277	0.217	0.190	0.254	0.212	0.267	0.176	0.213	0.139	0.167	0.134	0.131	0.167	0.168		

TABLE VI. Relative Discrepancy between the Measurements of the Color Difference Obtained by the Camera and by the Spectroradiometer for the Dark Grayish Subset Test

D^{r}_{00} *CIEDE2000*

Group Center	-2.5 Hue		+2.5 Hue		-1.0 Chroma		+2.0 Chroma		-1.0 Value		+1.0 Value		Mean	
	CSS	UMG	CSS	UMG	CSS	UMG	CSS	UMG	CSS	UMG	CSS	UMG	CSS	UMG
5R 4/2	0.637	0.598	0.925	0.870	0.184	0.073	0.188	0.112	0.141	0.155	0.004	0.002	0.347	0.302
5RP 4/2	0.014	0.000	0.305	0.319	0.391	0.237	0.423	0.332	0.263	0.260	0.003	0.000	0.233	0.191
5P 4/2	0.298	0.161	0.096	0.180	0.206	0.179	0.184	0.133	0.284	0.282	0.014	0.014	0.180	0.158
5PB 4/2	0.202	0.017	0.114	0.040	0.210	0.298	0.235	0.362	0.184	0.142	0.127	0.128	0.178	0.164
5B 4/2	0.092	0.110	0.213	0.387	0.225	0.433	0.020	0.175	0.239	0.172	0.021	0.030	0.135	0.218
5BG 4/2	0.021	0.015	0.520	0.645	0.212	0.419	0.043	0.120	0.117	0.023	0.011	0.004	0.154	0.204
5G 4/2	0.250	0.289	0.240	0.253	0.279	0.077	0.176	0.300	0.205	0.125	0.012	0.006	0.194	0.175
5GY 4/2	0.267	0.203	0.101	0.084	0.017	0.078	0.124	0.184	0.084	0.075	0.072	0.082	0.111	0.118
5Y 4/2	0.534	0.428	0.300	0.141	0.082	0.138	0.189	0.277	0.119	0.119	0.080	0.070	0.217	0.196
5YR 4/2	0.173	0.204	0.219	0.145	0.071	0.012	0.088	0.001	0.031	0.028	0.063	0.061	0.108	0.075
Mean	0.249	0.203	0.303	0.306	0.188	0.194	0.167	0.200	0.167	0.138	0.041	0.040		

D^{r}_{ab} *CIELAB*

Group Center	-2.5 Hue		+2.5 Hue		-1.0 Chroma		+2.0 Chroma		-1.0 Value		+1.0 Value		Mean	
	CSS	UMG	CSS	UMG	CSS	UMG	CSS	UMG	CSS	UMG	CSS	UMG	CSS	UMG
5R 4/2	0.674	0.625	0.920	0.861	0.040	0.039	0.116	0.012	0.109	0.111	0.042	0.053	0.317	0.284
5RP 4/2	0.007	0.022	0.355	0.383	0.299	0.111	0.444	0.299	0.236	0.222	0.041	0.056	0.230	0.182
5P 4/2	0.033	0.157	0.180	0.263	0.035	0.020	0.138	0.071	0.255	0.245	0.071	0.082	0.119	0.140
5PB 4/2	0.014	0.156	0.161	0.249	0.268	0.337	0.176	0.229	0.192	0.165	0.180	0.185	0.165	0.220
5B 4/2	0.244	0.268	0.075	0.088	0.253	0.384	0.006	0.135	0.245	0.211	0.090	0.097	0.152	0.197
5BG 4/2	0.047	0.013	0.479	0.579	0.251	0.413	0.137	0.061	0.152	0.102	0.063	0.065	0.188	0.205
5G 4/2	0.238	0.282	0.201	0.217	0.313	0.120	0.072	0.226	0.214	0.172	0.048	0.060	0.181	0.180
5GY 4/2	0.288	0.237	0.082	0.052	0.007	0.064	0.095	0.143	0.027	0.020	0.121	0.128	0.103	0.107
5Y 4/2	0.410	0.289	0.279	0.067	0.080	0.135	0.212	0.303	0.183	0.187	0.042	0.029	0.201	0.168
5YR 4/2	0.203	0.247	0.095	0.010	0.027	0.097	0.044	0.054	0.065	0.068	0.024	0.011	0.076	0.081
Mean	0.216	0.230	0.283	0.277	0.157	0.172	0.144	0.153	0.168	0.150	0.072	0.076		

TABLE VII. Assessment of Extreme-Center Sample Pair of Fabrics. In the Measurements Made by the Camera, the UMG Based Linear Transform from RGB to CIE XYZ Values was Used

Extreme-Center Sample		Color Variability MCDM CIEDE2000 ($n\Delta E_{00}$)				Color difference			Result	
Pair (L*a*b*)		Side A		Side B						
		SpecR.	Camera	SpecR.	Camera	SpecR.	Abs. Disc	Camera	SpecR.	Camera
Navy 1	(17,5 : 0,7 : -4,8)	0,49	2,18	0,72	2,44	0,83	1,91	2,74	Pass	Pass
Navy 2	(17,6 : 0,6 : -5,2)	0,27	1,20	0,35	1,18	0,75	2,19	2,94	**Fail**	**Fail**
Blue 1	(18,3 : 0,6 : -5,4)	0,52	3,74	0,75	3,22	0,74	3,94	4,68	Pass	Pass
Blue 2	(18,2 : 0,6 : -5,1)	0,24	2,44	0,33	2,72	0,37	2,77	3,14	Pass	Pass
Black 1	(16,3 : 1,0 : -2,6)	0,43	2,75	0,62	3,13	0,66	2,55	3,21	Pass	Pass
Black 2	(16,1 : 0,9 : -2,4)	0,24	1,67	0,35	1,67	0,93	1,86	2,79	**Fail**	Pass
Green 1	(33,4 : -0,4 : 8,9)	0,34	0,59	0,41	0,83	0,71	0,38	1,09	Pass	Pass
Green 2	(32,4 : -0,4 : 8,9)	0,59	1,44	0,73	1,82	0,77	0,94	1,71	Pass	Pass

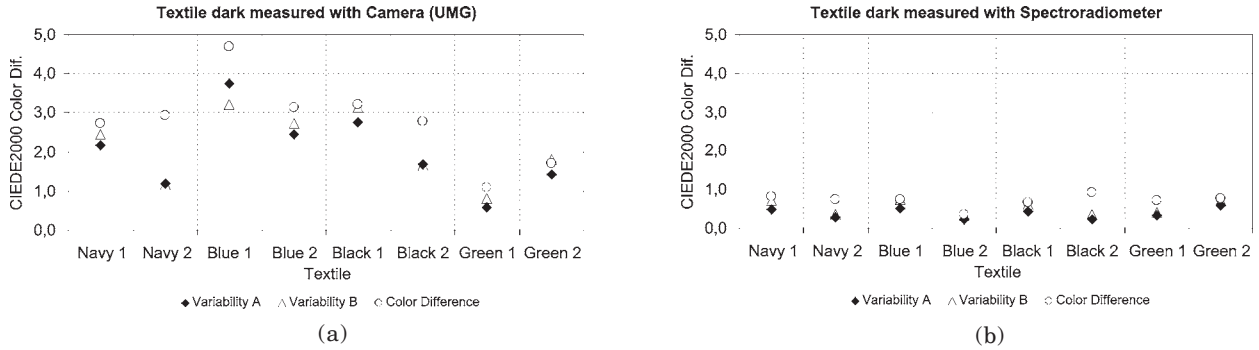

Figure 12. Assessment of the extreme-center sample pairs by: (a) camera, (b) spectroradiometer. The variability (◆ side A, △ side B) and CIEDE2000 color difference (○) data are taken from Table VII.

that compose the central field window of the captured image. Although we have computed the camera XYZ values using both the CSS and UMG based linear transforms of Eqs. (4) and (5), we only present the results obtained using the UMG linear transform in this section. Since each sample pair is made of a single fabric, we expect to obtain similar variabilities for both sides. The results are contained in Table VII and in Fig. 12. Note that each extreme-center sample pair is labeled by a generic color followed by a number and their mean L^* a^* b^* CIELAB coordinates measured by the spectroradiometer. As expected, the color variabilities of both sides of given pair, represented by small triangles in Fig. 12, are quite similar in all cases. The influence of texture can be clearly appreciated in the magnitudes of the MCDM values, especially those high values measured by the camera.

We measure the color difference between the sides A and B of each pair following this procedure: we calculate the color differences between a sample point of one side and each one of the ten sample points of the other side; then, we repeat the same calculation for the rest of nine sample points of the first side to complete a set of 100 individual measurements of the color differences between sides A and B of the given pair. We take then the mean value and compare it with the variabilities (expressed as MCDM) of both sides of the pair. If the mean color difference between both sides is clearly higher, depending of the quality standard, than the variabilities, then it can be said that the extreme-center samples of the pair are different, and the result is "fail". Otherwise, they are accepted as similarly dyed, and the color matching "passes" the test. The mean color differences, the absolute discrepancy between the camera and the reference instrument, and the pass–fail results obtained in our experiment are contained on the right–hand of Table VII. The mean color differences measured by the spectroradiometer and the camera are also represented in Fig. 12 by small circles. As a quality standard, we have considered that a given extreme-center sample pair obtains a "fail" result when the mean color difference between its sides is higher than twice the highest variability of the sides. The instrument precision and the standard of quality have a decisive influence in the final result. Thus, for instance, if the common human visual discrimination of color was applied as quality standard, a suprathreshold of visual discrimination (0.887 CIELAB units[29]) could be used alternatively. We observe that the values obtained by the camera are generally higher than those obtained by the spectroradiometer, which might be due to a higher sensitivity of the camera to texture than the reference instrument. In other words, the spectroradiometer performs a certain integration within the sample area assessed, whereas the camera is more influenced by the variations of the fabric structure imaged pixel by pixel. However, both instruments lead ultimately to similar results. There is only one case (Black 2) out of the eight cases analyzed for which the final decision depends on the instrument: it fails for the reference instrument, but passes for the camera. In fact, this case is near the limit of the applied standard of quality (the mean color difference measured by the camera is 1.7 times the vari-

TABLE VIII. Absolute Discrepancies in the Color Differences of the Extreme-Center Sample Pairs Measured by the Spectroradiometer and the Camera in Three Cases: Without Filtering the Camera Images (the Data Coincide with those Presented in Table VII), with a Smoothing Filter, with a (±20%) Filter.

Extreme-Center Sample Pair (L*a*b*)		Color Difference Absolute discrepancy		
		Without filtering	Smoothing filter	(±20%) filter
Navy 1	(17,5 : 0,7 : -4,8)	1,91	1,83	1,70
Navy 2	(17,6 : 0,6 : -5,2)	2,19	2,28	1,98
Blue 1	(18,3 : 0,6 : -5,4)	3,94	3,91	3,97
Blue 2	(18,2 : 0,6 : -5,1)	2,77	2,64	2,43
Black 1	(16,3 : 1,0 : -2,6)	2,55	2,52	2,39
Black 2	(16,1 : 0,9 : -2,4)	1,86	1,83	1,66
Green 1	(33,4 : -0,4 : 8,9)	0,38	0,33	0,25
Green 2	(32,4 : -0,4 : 8,9)	0,94	0,91	0,93

ability of the sides) and we should also bear in mind the difficulty of the color involved (black).

For a better understanding of both instrument performances, we have filtered the measurements obtained by the camera in order to introduce some integration in the sample area imaged. Two sorts of filters have been applied. One of them is a smoothing filter. In each sample, we have lightly smoothed the image using a Gaussian mask of 5 × 5 pixels before taking the mean values of $L^*a^*b^*$. This filter averages the effects of texture within a sample area that approximately corresponds to thread size, more specifically, 5 pixels corresponds to the mean thread width in both the warp and weft directions of the fabric samples under study (in comparison, the integration area of the spectroradiometer is 100 times wider). Alternatively, we have built the L^* histogram of the sample image and then, we have neglected all the values within either the lowest 20% (shadow) or the highest 20% (bright) of the histogram. This other filter resembles a median filter. From the filtered images, we have recalculated all the variabilities and the color differences obtained by the camera system. For each sort of filter, we have built a table analogous to Table VII. In both cases of filtering, the results obtained by the camera were slightly closer to those obtained by the spectroradiometer than before (Table VII). The final Pass/Fail results did not alter in any case. Table VIII contains the absolute discrepancies between the measurements obtained by the spectroradiometer and the camera in all the three cases analyzed: without filtering (same as in Table VII), smoothing filter, and (±20%) filter. It can be seen that, in general, the absolute discrepancies reduce when some integrating filter is applied to the sample images captured by the camera.

Conclusions

The method presented here analyzes the camera's capability to measure small color differences between sample pairs with reliability. In the first part, the appropriate working conditions are established, the camera spectral sensitivities and imaging noise are characterized, and the transformation to obtain a device independent representation of color is calculated considering two different approaches: one, on the basis of the camera spectral sensitivity (CSS), and two, on the basis of the unified measure of goodness of the camera (UMG) that involves an imaging noise model. In the second part, a large number of varied small color differences in the very pale and the dark grayish color regions are measured by both the camera and the reference instrument. The assessment of the camera performance is based on the analysis of the results, the involved uncertainty, the absolute discrepancy and the relative discrepancy between the camera and the reference instrument.

The method was applied to a camera vision system (3CCD camera SONY DX-9100P) placed in an observation booth with controlled illumination of a D65 real simulator. We used a spectroradiometer (PhotoResearch PR-715) as the reference instrument. Good agreement was obtained between the color differences measured by the spectroradiometer and the camera. Although the mean values of the absolute discrepancy exceed the camera uncertainty, most of them fall within the camera tolerance in the case of very pale colors (CIELAB 0.5 ΔE^*_{ab} or CIEDE2000 0.6 ΔE_{00}). This fact, along with the magnitude of the camera tolerance, is considered a good achievement for the camera's performance. In the dark grayish region, probably caused by a greater influence of dark current, the absolute discrepancies are somewhat higher. Nevertheless, nearly all of them are still lower than the minimal color error calculated with the UMG approach (ε_{min} = 1.423 CIELAB units). The relative discrepancies are low and nearly uniform around the circle of hue in both the very pale and the dark grayish regions. This fact is also a good property of the camera performance. The use of the two CIELAB and CIEDE2000 metrics in parallel led to similar results. The two approaches (CSS and UMG) used in the linear transformation of the RGB values to the camera estimate XYZ values led also to similar results in the measurement of the color differences between sample pairs.

The camera system has been applied to the evaluation of color uniformity in textile dyeing. Eight pairs of extreme-center fabric samples have been analyzed by both the camera and the reference instrument. In this case, the effects of the texture are noticed. Although the camera is more sensitive to texture than the spectroradiometer, both instruments yielded consistent and satisfactory Pass/Fail results. Since the samples assessed were real cases of high difficulty (most of them were very dark colors), the results showed the high quality of the camera performance and, thereby, the potential of this sort of machine vision system for colorimetric tasks that usually have been exclusively the domain of trained observers.

Acknowledgment. The authors acknowledge the financial support of Spanish Ministerio de Educación y Ciencia and FEDER funds (under project No. DPI2003-03931). Edison Valencia thanks the Universitat Politècnica de Catalunya for a PhD scholarship.

References

1. P. L. Vora, J. E. Farrell, J. D. Tietz, and D. H. Brainard, "Digital models", (Hewlett-Packard Laboratory, Palo Alto, CA, 1997), Contract no. HPL-97 53. Available from: http://www.hpl.hp.com/techreports/97/HPL-97 53.html.
2. P. L. Vora, J. E. Farrell, J. D. Tietz, and D. H. Brainard, "Digital response", (Hewlett-Packard Laboratory, Palo Alto, CA, 1997), Contract no. HPL-97-54. Available from: http://www.hpl.hp.com/techreports/97/HPL-97-54.html.
3. K. Barnard and B. Funt, "Camera characterization for color research," *Color Res. Appl.* **27** (3), 152–163 (2002).
4. G. Hong, M.R. Luo and P.A. Rhodes, "A study of digital camera colorimetric characterization based on polynomial modeling," *Color Res. Appl.* **26**, 76–84 (2001).
5. E. Marszalec, J. B. Martinkuppi, M. N. Soriano, and M. Pietikäinen,

"Physics-based FACE database for color research," *J. Electronic Imaging* **9**, 32–38 (2000).
6. F. Xiao, J. M. DiCarlo, P. B. Catrysse, and B. A. Wandell, "High dynamic range imaging of natural scenes," *Proc. IS&T/SID 10th Color Imaging Conference*, (IS&T, Springfield, VA, 2002) pp. 337–342.
7. http://pdc.standford.edu/hdri
8. F. H. Imai, D. R. Wyble, R. S. Berns, and D.Y. Tzeng, "A feasibility study of spectral color reproduction," *J. Imaging Sci. Technol.,* **47**, 543 (2003).
9. F. H. Imai, R. S. Berns and D.Y. Tzeng, "A comparative analysis of spectral reflectance estimated in various spaces using a trichromatic camera system," *J. Imaging Sci. Technol.,* **44**, 280 (2000).
10. E. Marszalec, J. B. Martinkuppi and M. Pietikäinen, "Evaluation of the performance of a colour camera for measuring small colour differences," *Proc. SPIE* **3208**, 348–359 (1997).
11. M. S. Millán, E. Valencia and M. Corbalán, "3CCD camera's capability for measuring color differences: experiment in the nearly neutral region," *Appl. Opt.* **43**, 6523–6535 (2004).
12. P. L. Vora and H. J. Trussell, "Measure of goodness of a set of color-scanning filters," *J. Opt. Soc. Amer. A* **10** (7), 1499–1508 (1993).
13. S. Quan, N. Ohta, R. S. Berns, and X. Jiang, "Unified measure of goodness and optimal design of spectral sensitivity functions," *J. Imaging Sci. Technol.*, **46**, 485–497 (2002).
14. R. W. G. Hunt, "Chromatic adaptation in image reproduction," *Color Res. Appl.* **7**, 46–49 (1982).
15. E. A. Fedorovskaya, H. de Ridder and F. J. J. Blommaert, "Chroma variations and perceived quality of color images of natural scenes," *Color Res. Appl.* **22**, 96–110 (1997).
16. G. Wyszecki and W. S. Stiles, *Color Science. Concepts and Methods, Quantitative Data and Formulae*, (John Wiley & Sons, Inc. New York, 1982).
17. R. S. Berns, *Billmeyer and Saltzman's Principles of Color Technology*, 3rd ed., (Wiley, New York, NY, 2000).
18. M. R. Luo, G. Cui and B. Rigg, "The development of the CIE 2000 colour-difference formula: CIEDE2000," *Color Res. Appl.* **26**, 340–350 (2001).
19. G. Johnson and M. D. Fairchild, "A top down description of S-CIELAB and CIEDE2000," *Color Res. Appl.* **28**, 425–435 (2003).
20. P. M. Hubel, D. Sherman and J. Farrell, "A comparison of methods of sensor spectral sensitivity estimation," *Proc. IS&T's 1999 PICS Conference*, (IS&T, Springfield, VA, 1999), 153–157.
21. G. D. Finlayson, S. Hordley and P. M. Hubel, "Recovering device sensitivities with quadratic programming," *Proc. IS&T's 6th Color Imaging Conference*, (IS&T, Springfield, VA, 1998), pp. 90–95.
22. M. J. Vhrel and H. J. Trusell, "Color device calibration: A mathematical formulation," *IEEE Trans. Image Process* **8**, 1796 (1999).
23. R. S. Berns and D. M. Reiman, "Color managing the 3rd edition of Billmeyer and Saltzman's Principles of Color Technology," *Color Res. Appl.* **27**(5), 360–373 (2002).
24. M. L. Simpson, J. F. Jansen, "Imaging colorimetry: a new approach," *Appl. Opt.* **30**, 4666–4671 (1991).
25. M. Corbalán, M. S. Millán and M. J. Yzuel., "Color measurement in standard CIELAB coordinates using a 3CCD camera: correction for the influence of the light source," *Opt. Eng.* **39**, 1470–1476 (2000)
.26. G. H. Healey, R. Kondepudy, "Radiometric CCD camera calibration and noise estimation," *IEEE Trans. Pattern Analysis and Machine Intelligence*, *PAMI* **16,** 267–276 (1994).
27. G. C. Holst, *CCD Arrays, Cameras, and Displays,* 2nd ed. (SPIE Press, Bellingham, WA, 1999).
28. J. Y. Hardeberg, H. Brettel and F. Schmidt, "Spectral characterization of electronic cameras," *Proc. SPIE* **3409**, 100–109 (1998).
29. M. Melgosa, E. Hita, A. J. Poza, D. H. Alman, and R. S. Berns, "Suprathreshold Color-difference Ellipsoids for surface colors," *Color Res. Appl.* **22**(3), 148–155 (1997).

Color image sharpening inspired by human vision models

App. Opt. **45**(29), 7684-7697 (2006).

Color image sharpening inspired by human vision models

María S. Millán and Edison Valencia

A method to sharpen digital color images that takes viewing conditions and human vision models into consideration is described. The method combines the Laplacian of Gaussian (LoG) operator with spatial filters that approximate the contrast sensitivity functions of human visual systems. The sharpening operation is introduced in the opponent color space, following the scheme proposed in the spatial extension of CIELAB (S-CIELAB). We deduce the modification of the original image necessary to obtain the spatially filtered image that approaches the perceived LoG-sharpened image for given viewing conditions. At short viewing distances, for which the spatial blurring is small, most fine edges and object contours are sharpened. At long distances, for which the spatial blurring is greater, only large figures are sharpened. Because of the smoothing Gaussian functions involved in the LoG operator, the proposed image sharpening does not tend to increase noise. When the sharpening operation is limited to the achromatic channel, the results are good. This is consistent with the high importance attached to the luminance channel in the spatial content of color images. Image sharpening based on only the Laplacian of the original is not sensitive to variations of viewing conditions, tends to increase noise, and suffers from its appearance deteriorating rather quickly with the depth of the sharpening operation.

OCIS codes: 100.0100, 330.0330, 100.2000, 100.2980, 330.1690, 330.6110.

1. Introduction

Edges and object contours in images are usually noisy and badly defined areas as a consequence of the point-spread function of the camera lens, the sensor and/or display resolution, viewing conditions, and digital operations such as image compression and halftone patterns. There are a large number of applications for which image edges or the differences between adjacent light and dark sample points in an image need to be emphasized or sharpened. But image sharpening is a double-edged sword: It may wonderfully enhance an image, but, on the other hand, an improper or excessive use of it affects the image, producing artifacts such as overly contrasted contours, edges that look like halos around objects, jagged edges, mottled areas, and increasing noise.

The use of a second derivative or Laplacian operator to enhance gray-scale images by edge sharpening is widely known. A discrete representation of this operator is a convolving mask whose kernel computes the addition of the weighted gray-level differences between a pixel and its neighbors. The operator has been extended to color images by applying it to each red (R), green (G), or blue (B) component separately and combining the result to yield the sharpened color image.[1] As has been reported, the simple extension of classical gray-level methods to the RGB channels is not the best solution.[2–7] In fact, reasonably good results can be obtained by sharpening edges just in the intensity component while keeping the chromatic components of hue and saturation unchanged.[8] In the work of Di Zenzo[2] color images are treated as multivalued functions for which the tensor gradient is used in more effective edge detection. A more abstract treatment was done by Sochen *et al.*[4,5] They viewed images as embedding maps that flow toward minimal surfaces. They considered a color image as a 2D surface in a 5D space (x, y, RGB). Their geometric framework led to building powerful smoothing and scale space algorithms. In the mathematics developed in Refs. 2–7 the feature coordinates of a color image are the RGB intensity values, although the authors of Ref. 5 mentioned the possibility of using a Euclidean space such as the international standard CIELAB system (CIE 1978). This space has also been used as a basis to define a color-difference-based Laplacian operator for color image sharpening in Ref. 9. But CIELAB, as well as other standard systems, was tested against data from color appearance

The authors are with the Departamento Óptica y Optometría, Universidad Politécnica de Cataluña, Violinista Vellsolà, 37, 08222 Terrassa, Spain. M. S. Millán's e-mail address is millan@oo.upc.edu. E. Valencia's e-mail address is edison@oo.upc.edu.

Received 19 December 2005; revised 25 May 2006; accepted 30 May 2006; posted 31 May 2006 (Doc. ID 66762).

0003-6935/06/297684-14$15.00/0

judgments of large uniform patches. Consequently, it should not be used to determine the color difference between images on a pixel-by-pixel basis because a point-by-point computation of the CIELAB error tends to produce larger errors at most image points than the perceived ones.[10]

Zhang and Wandell[10] proposed a spatial extension to the CIELAB color metric, known as the S-CIELAB metric, that can be applied to complex stimuli, such as digital images, when they are viewed at different distances. They use a series of spatial filters in the opponent color space AC_1C_2, containing one luminance channel (A) and two chrominance channels (C_1, C_2). The filters are smoothing filters consisting of a linear combination of Gaussian masks that approximate the contrast sensitivity functions of the human vision system for a given viewing distance. The filtered image is then back transformed to the CIELAB representation. S-CIELAB allows one to measure the perceived color differences by applying the standard CIELAB formula ΔE to the filtered images pixel by pixel. S-CIELAB has been used to measure color reproduction errors in images,[10] to predict texture visibility of printed halftone patterns,[11] to evaluate the effects of image compression,[10] and to segment color images.[12] This technique can be implemented in both the spatial and the frequency domains.[13] The CIE 2000 color-difference formula[14] (CIEDE2000) ΔE_{00} combined with S-CIELAB was compared with other existing CIE color-difference formulas and three different viewing conditions in Ref. 13. Recently, a new model of the contrast sensitivity functions that is specifically designed for use in image-difference and image-quality models was introduced.[15]

In this work we introduce a new method for color image sharpening that takes into consideration the viewing conditions of an image and the models of the human vision system. Our method follows the basic steps defined in the S-CIELAB algorithm since it offers an interesting scheme to introduce spatial filtering of the visual system in digital color images. We combine such spatial filtering with the Laplacian operator in each channel of the opponent space to obtain the sharpened image. In fact, there is evidence that shows that smoothing and sharpening spatial filters can simulate the on-center off-surround receptive field performance of the primary stages of human vision.[16,17] For instance, the brightness enhancement of Mach bands, which can be explained by retinal receptive field center–surround interactions,[18] is closely related to the result obtained after applying the Laplacian operator. Since the spatial filters used in S-CIELAB are linear combinations of weighted Gaussian functions, the application of the Laplacian to the spatially filtered components can be further simplified by introducing the Laplacian of Gaussian (LoG).[19] This operator takes advantage of the properties of convolution and derivatives and is widely used as an edge detector with a reduced sensitivity to noise. The LoG operator can be approximated by the difference of Gaussians (DoG) that is a computationally efficient function. The DoG function can be computed by convolving an image with two Gaussians of different spread and forming the difference of the resulting two smoothed images. The use of DoG is consistent, and it can be justified since it has also been widely utilized to model receptive fields in early human vision (see, for instance, Refs. 17 and 19). Thus, summarizing, to sharpen a color image that is to be seen at a given viewing condition (i.e., pixel resolution and distance) we combine the basic steps of the S-CIELAB algorithm with either the LoG or the DoG operators to generate the modified spatial filters to convolve with the image in the opponent color space representation. In the case of the DoG operator the modification is quite simple as the new spatial filters are again linear combinations of convolving Gaussian functions but of different spread. The LoG (DoG) filtered images are subtracted from the image component in each opponent channel, then back transformed to *XYZ* space, and then to the device-dependent color representation space RGB (sRGB) for display. We will assume some monitor type (sRGB)[20] using appropriate color profiles. The result is a sharpened color image adapted to viewing conditions.

As far as we know, this compact combination of the S-CIELAB algorithm with derivative edge detectors in the opponent color space has not yet been applied to the color sharpening of digital images. To the best of our knowledge it is also new that human vision models and viewing conditions are involved in the sharpening operation.

The method proposed here is applied to several digital color test images to render sharpened images. We evaluate the possible artifacts that may appear as a consequence of having spatially filtered with different size filters for each channel and the lack of orthogonality of the three channels in the opponent color space. The results are compared on the S-CIELAB basis with other results obtained by applying the LoG operator to the achromatic channel A only (keeping the chrominance C_1 and C_2 components unchanged) or just the Laplacian (∇^2) to the image components in all three channels.

2. Spatial Filtering in the Opponent Color Space and S-CIELAB

In this section we give a brief overview of S-CIELAB[10] that constitutes a general background on which we describe our proposal in the following sections. With S-CIELAB, Zhang and Wandell[10] provided a metric to determine the perceived color differences between image pairs.

To implement S-CIELAB, a sequence of steps has to be followed. First, it is necessary to transform the input images into a device-independent color space, such as CIE 1931 *XYZ*. This transformation requires having a well-characterized display device such as a computer CRT display that can be characterized, for instance, by applying the gain, offset, gamma (GOG) model,[21] although the method can be extended to other displays such as printers. In the following, we assume that the input images of a given pair are

expressed in the standard color space sRGB and are then transformed into CIE *XYZ*.

The second step involves a spatial filtering of the images that is performed in an opponent color space consisting of one luminance channel (A) and two chrominance channels (C_1, C_2). The transformation and spatial filters used in S-CIELAB have been estimated from human psychophysical measurements of color appearance.[22] The opponent channels AC_1C_2 are linear transformed from CIE 1931 *XYZ* as shown by the equation

$$\begin{bmatrix} A \\ C_1 \\ C_2 \end{bmatrix} = \begin{bmatrix} 0.297 & 0.72 & -0.107 \\ -0.449 & 0.29 & -0.077 \\ 0.086 & -0.59 & 0.501 \end{bmatrix} \begin{bmatrix} X \\ Y \\ Z \end{bmatrix}. \quad (1)$$

Since the three AC_1C_2 channels are not completely orthogonal, some color fringes may appear after spatially filtering the image components with different size filters in each channel. These effects are not particularly relevant when calculating color differences for the number of applications described in Refs. 10–13, but it may generate artifacts when rendering images. Nevertheless, we will use the transform given by Eq. (1) in subsequent sections, and we will examine the possible complications caused by the lack of orthogonality.

Once two images I and I' are transformed into the opponent color space, they are spatially filtered using filters that approximate the contrast sensitivity functions of the human visual system. This filtering can be carried out either via convolution in the spatial domain, as we do in this work, or by multiplication in the frequency domain.[13] In each opponent channel, the filter is a linear combination of weighted Gaussian functions, and its kernel sums to 1. Thus the three filters preserve the mean color value for large uniform areas, and S-CIELAB and CIELAB give similar predictions for them. The kernel of each spatial filter F_{di} is given by

$$F_{di}(x, y) = \sum_j w_{ij} G_{ij}\left(x, y, \frac{d\sigma_{ij}}{\sqrt{2}}\right), \quad (2)$$

where $i = \{0, 1, 2\}$ indicates the opponent channel $\{A, C_1, C_2\}$, w_{ij} is the weight, and G_{ij} is the normalized kernel of a Gaussian function described by the expression

$$G(x, y, s) = \frac{1}{S} \exp\left[-\frac{(x^2 + y^2)}{2s^2}\right]. \quad (3)$$

In Eq. (3) s is the spread and S is a constant that normalizes the kernel of the Gaussian so that it sums to one. In Eq. (2), the spread of the Gaussian functions is $s_{ij} = d\sigma_{ij}/\sqrt{2}$, and it represents the decrease in sensitivity that occurs in the human vision system when the viewing distance increases. This blurring effect is represented by the product of the spread expressed in degrees of visual angle (σ_{ij}) times the number of pixels per degree of visual angle (d) when the observer is placed at a given distance from the monitor. Table 1 shows the values of weights and spreads used in S-CIELAB.[10,13] Note that the weights w_{ij} correspond to those published in Ref. 13 that are already adjusted to sum to 1. Let us denote I_{di} and I_{di}' as the components of the spatially filtered images in the opponent color space. They are produced from the convolution of the spatial filters F_{di} with the input image components I_i and I_i':

Table 1. Weight and Spread of Gaussian Kernels Used to Build the Spatial Filters for Image Convolution in the Opponent Channels

i	j	w	σ
0 (A)	1	1.00327	0.0500
	2	0.11442	0.2250
	3	−0.11769	7.0000
1 (C_1)	1	0.61673	0.0685
	2	0.38328	0.8260
2 (C_2)	1	0.56789	0.0920
	2	0.43212	0.6451

$$I_{di}(x, y) = F_{di}(x, y) * I_i(x, y),$$
$$I_{di}'(x, y) = F_{di}(x, y) * I_i'(x, y), \quad (4)$$

where the symbol $*$ is the convolution operation. The 2D convolution in the spatial domain of Eq. (4) can be more efficiently computed as two 1D convolutions taking into account that the kernels are separable. It can be advantageously calculated in the frequency domain as is described in Ref. 13.

The filtered components in the opponent channels I_{di} and I_{di}' [Eq. (4)] are then transformed back into CIE *XYZ* space by using the linear transformation

$$\begin{bmatrix} X \\ Y \\ Z \end{bmatrix} = \begin{bmatrix} 0.979 & -1.535 & 0.445 \\ 1.189 & 0.764 & 0.135 \\ 1.232 & 1.163 & 2.079 \end{bmatrix} \begin{bmatrix} A \\ C_1 \\ C_2 \end{bmatrix}, \quad (5)$$

which is the inverse of Eq. (1). The filtered images $I_{d(XYZ)}$, $I_{d(XYZ)}'$ are transformed into the CIELAB space by using standard equations,[21] for which the tristimulus values of the white point of the display device X_n, Y_n, Z_n have to be known through the device characterization (sRGB monitors have a D65 white point). Once the CIELAB coordinates are calculated for all the pixels, the color differences between the filtered images $I_{d(CIELAB)}$ and $I_{d(CIELAB)}'$ can be computed on a pixel-by-pixel basis. The result is a color-difference image in which each pixel value represents the perceived color difference at that given point. The standard CIE ΔE_{ab}^* color-difference equation[21] has been traditionally used with S-CIELAB. Johnson and Fairchild[13] compare the results of three existing CIE color-difference formulas (ΔE_{ab}^*, ΔE_{94}^*, and ΔE_{00}) when evaluating the color-difference image for a given halftone image pair consisting of an original image and its replica as a cluster dot halftone image. From the image statistics, the authors pointed out

that CIEDE2000 (ΔE_{00}) tends to produce color-difference images (called error images) with the smallest mean and standard deviation among the set of three CIE color-difference formulas. In this work we also use the CIEDE2000 color-difference formula to compare image pairs.

3. Displayed and Perceived Sharpened Images

When performing operations that involve second derivatives for edge extraction, such as edge detection or image sharpening, it is a common practice to smooth the image first by convolution with a Gaussian kernel of spread s to reduce noise before computing a second derivative or Laplacian. Taking into account the properties of the derivative, Gaussian function, and convolution, it is verified that $\nabla^2[G(x, y, s) * I(x, y)] = \nabla^2 G(x, y, s) * I(x, y)$, in which the Laplacian of Gaussian is often just named LoG. A convolution kernel of the LoG operator can be obtained by sampling the continuous function $\nabla^2 G(x, y, s)$ over a $W \times W$ window. To reduce the deleterious truncation effects, the size of the kernel must be set so that $W = 3c \approx 8.5s$, where $c = 2\sqrt{2}s$ is the width of the central lobe of the LoG function.[23,24] Figure 1 shows a plot of $-\nabla^2 G(x, y, s)$.

A sharpened version ShI of a given image I can be obtained by computing

$$\mathrm{ShI}(x, y) = I(x, y) - \mathrm{LoG} * I(x, y). \quad (6)$$

In this work we propose to sharpen the components of the spatially filtered image in the color opponent space, taking into consideration the linear combination of weighted Gaussian functions that compose the spatial filters F_{di} [Eq. (2)] to build the LoG operator. This is the key point of the proposal, and it can be expressed by

$$\mathrm{ShI}_{di}(x, y) = I_{di}(x, y) - k\mathrm{LoG}\{F_{di}\} * I_{di}(x, y), \quad (7)$$

where k is a real positive parameter introduced to control the depth of the sharpening and

$$\mathrm{LoG}\{F_{di}(x, y)\} = \sum_j w_{ij}\mathrm{LoG}_{dij} = \sum_j w_{ij}\nabla^2 G_{ij}\left(x, y, \frac{\mathrm{d}\sigma_{ij}}{\sqrt{2}}\right). \quad (8)$$

In fact, Eq. (7) represents the sharpening of an image as it would be perceived in a given viewing condition. But the perceived sharpened image, represented in the opponent color space by ShI_{di} [Eq. (7)], has to be obtained by spatially filtering the corresponding sharpened image displayed on the monitor. The displayed sharpened image, whose components in the opponent color space are ShI_i, then verifies

$$F_{di}(x, y) * \mathrm{ShI}_i(x, y) = \mathrm{ShI}_{di}(x, y). \quad (9)$$

By introducing Eqs. (4) and (7) into Eq. (9), we obtain for the displayed LoG-sharpened image

$$\mathrm{ShI}_i(x, y) = I_i(x, y) - k\mathrm{LoG}\{F_{di}\} * I_i(x, y). \quad (10)$$

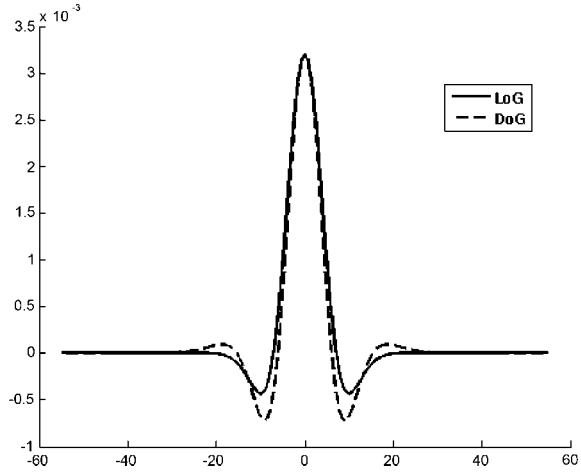

Fig. 1. Profile of the (negative) LoG function (solid curve). The Gaussian considered was $G(x, y, s = 5)$ [Eq. (3)]. The LoG profile can be approximated by a DoG function (dashed curve) $G(x, y, s_1) - G(x, y, s_2)$, with $s_2/s_1 = 1.6$ and $s_1 = s$ (Ref. 19). The DoG function has been plotted normalized to the LoG maximum for comparison.

Note that $\mathrm{ShI}_i(x, y)$ of Eq. (10) represents the sharpened image that must be displayed on the monitor to perceive the sharpened image $\mathrm{ShI}_{di}(x, y)$ of Eq. (7) in the viewing condition given by d (pixels/degree of vision angle). Equations (7) and (10) describe a LoG-based sharpening operation in the perceived and the displayed levels, respectively, that depends on

- the opponent channel—it also involves the linear combinations of Gaussian functions used for spatial filtering in the opponent channels, and
- the viewing conditions (i.e., monitor addressability and viewing distance) through the number of pixels/degree of visual angle d.

Let us consider a monitor that displays a color image of $N \times M$ pixel size with a fixed number of pixels/cm. At short viewing distances, for which the spatial blurring is small, Eq. (10) would sharpen most fine edges and large object contours. At these short distances, some noise could also be emphasized. At long distances, however, for which the spatial blurring is greater, Eq. (10) would sharpen just the most significant object contours. Moreover, the spatial extension of the double edge produced by the $\mathrm{LoG}\{F_{di}\}$ operator, which is added to the image component for sharpening, varies with distance. Whereas fine double edges would be added when viewing the image at short distances, thicker double edges would be added at longer distances. In addition, this sort of image sharpening tends to preserve the continuous tone perceived of areas covered by patterns of spatial rapid variations such as those processed with a halftone algorithm. This is a remarkable property of the proposed sharpening technique, since the majority of sharpening techniques tend to increase noise and the differences between small individual dots.

To have ShI_i displayed on the monitor, it is necessary to first transform the image components in the

opponent color space back into the CIE *XYZ* by using Eq. (5). The result is transformed in turn into sRGB to address the sharpened image $\mathrm{ShI}_{\mathrm{RGB}}$ for display on the monitor.

Several other possibilities can be considered for color image sharpening instead of that used in Eq. (7). Let us mention two of them. In the first one, we consider that the sharpening operation [Eq. (7)] is limited just to the achromatic channel A that represents luminance and that the chrominance channels C_1 and C_2 are kept unchanged. In the second possibility, we consider that the LoG operator is convolved by the image component I_i (before the spatial filtering) in Eq. (7). In such a case, the components of the perceived sharpened image would be

$$\mathrm{ShI}_{di}(x, y) = I_{di}(x, y) - k\mathrm{LoG}\{F_{di}\} * I_i(x, y). \quad (11)$$

Equation (11) can be rewritten as

$$\mathrm{ShI}_{di}(x, y) = I_{di}(x, y) - k\nabla^2 I_{di}(x, y)$$

$$= F_{di}(x, y) * \left[I_i(x, y) - k\nabla^2 I_i(x, y)\right], \quad (12)$$

and, taking into account Eq. (9), the components of the corresponding displayed sharpened image should be

$$\mathrm{ShI}_i(x, y) = I_i(x, y) - k\nabla^2 I_i(x, y). \quad (13)$$

The sharpening operation described by Eq. (13) corresponds to the traditional Laplacian-based sharpening operation. Although it is defined here for the channels of the opponent color space, the same form has been extensively used in a single gray-scale channel[1,8] and other sets of three channels corresponding to different color spaces (RGB and CIELAB, for example).[1,9] This sharpening operation tends to increase noise excessively since no smoothing of the image is performed prior to applying the second derivative. In such a case, the image smoothing corresponds just to the spatial filtering of visual perception according to Eq. (12).

Finally, we consider that the LoG operator can be closely approximated by a difference of Gaussians or DoG operator in the preceding equations. This DoG is defined by

$$\mathrm{DoG}(x, y, s_1, s_2) = G(x, y, s_1) - G(x, y, s_2), \quad (14)$$

and it can be used as a convolution kernel instead of (−LoG). Marr and Hildreth[19] found that the ratio $s_2/s_1 = 1.6$ provides a good approximation to the LoG (Fig. 1). This sort of operator has been used to describe the neural cell performance of the receptive fields in human vision.

4. Experiments

We apply the sharpening operation described by Eqs. (7)–(10) to the test image $I(x, y)$ of 385 × 289 pixel size [Fig. 2(a)]. Let us consider that this image is to be displayed on a CRT monitor controlled by a computer.

(a)

(b)

Fig. 2. (Color online) (a) Test, original image of 385 × 289 pixel size. (b) Set of ten regions of interest of nearly uniform colors that are defined to analyze noise and color variations due to the processes.

Since the RGB values are device dependent, we perform the color transformations based on devices that conform to sRGB. The sRGB color space has been characterized by the International Electrotechnical Commission (IEC).[20] Thus, we consider that the original image is in sRGB; i.e., it was created using devices that conform to sRGB, and the monitor is sRGB compliant, and it is associated with an appropriate color profile. In consequence, the resulting processed images will be consistent across the devices, and we will be able to compare them with the original in appearance. The formulas to convert between sRGB and the *XYZ* tristimulus values for the D65 white point are the following (also available on the Internet[20,25]):

$$\begin{bmatrix} X \\ Y \\ Z \end{bmatrix} = \begin{bmatrix} 0.4124 & 0.3576 & 0.1805 \\ 0.2126 & 0.7152 & 0.0722 \\ 0.0193 & 0.1192 & 0.9505 \end{bmatrix} \begin{bmatrix} \mathrm{R} \\ \mathrm{G} \\ \mathrm{B} \end{bmatrix},$$

$$\begin{bmatrix} \mathrm{R} \\ \mathrm{G} \\ \mathrm{B} \end{bmatrix} = \begin{bmatrix} 3.2406 & -1.5372 & -0.4986 \\ -0.9689 & 1.8758 & 0.0415 \\ 0.0557 & -0.2040 & 1.0570 \end{bmatrix} \begin{bmatrix} X \\ Y \\ Z \end{bmatrix}. \quad (15)$$

Let us consider that the monitor is capable of displaying p pixels per centimeter (ppc) and it is viewed at L cm. The number of pixels per degree of visual

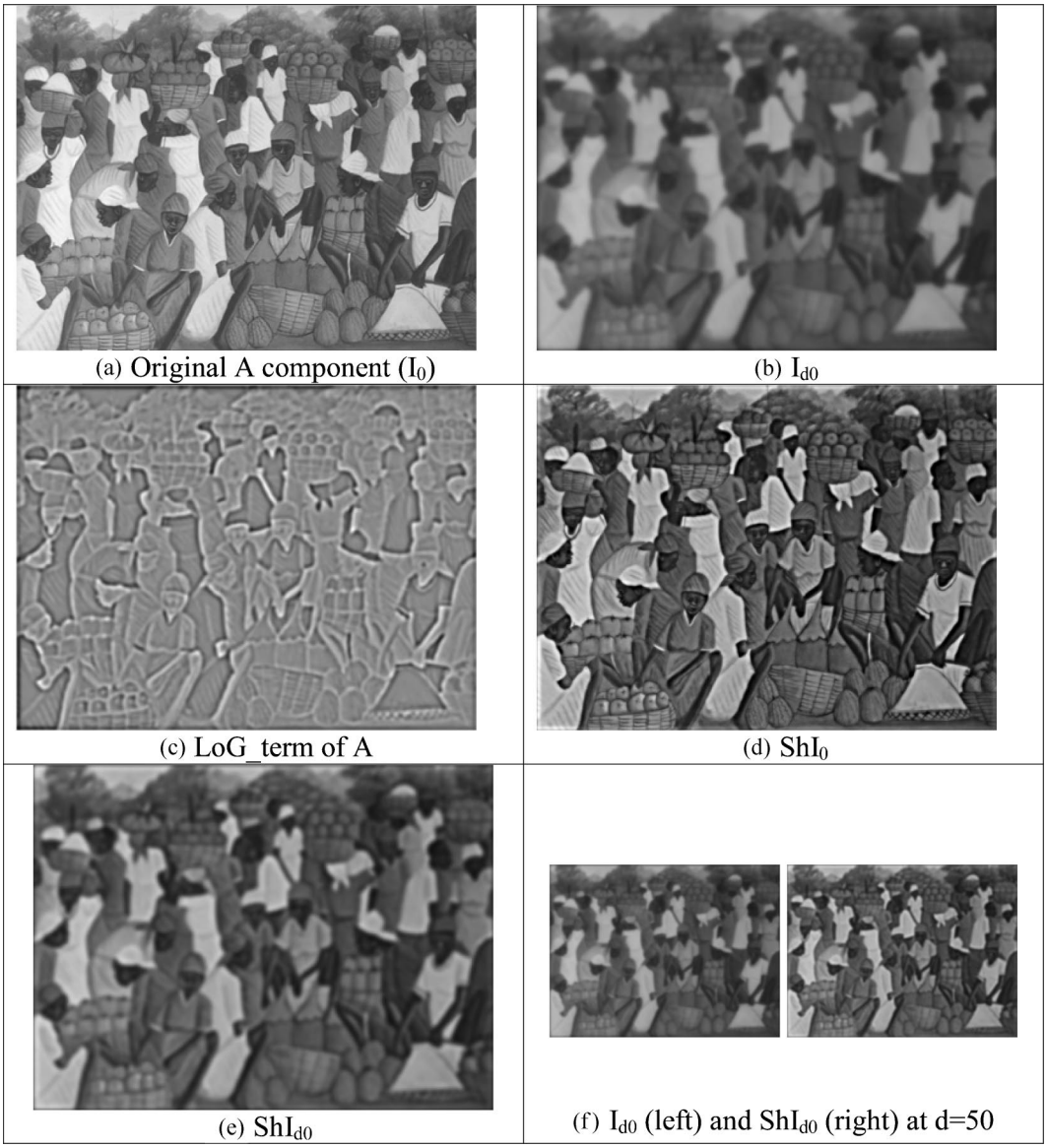

Fig. 3. Sharpening operation in the A channel ($i = 0$) for $d = 50$ pixels/degree and $k = 5$: (a) original image component $I_0(x, y)$, (b) spatially filtered image $I_{d0}(x, y)$ shown with the same scale as in (a), (c) LoG term $k\text{LoG}\{F_{d0}\} * I_0(x, y)$, (d) sharpened image component $\text{ShI}_0(x, y)$, (e) spatially filtered sharpened image component $\text{ShI}_{d0}(x, y)$ shown with the same scale as in (d), (f) scaled versions of $I_{d0}(x, y)$ and $\text{ShI}_{d0}(x, y)$ as they would be seen at $d = 50$ pixels/degree.

angle is then

$$d = pL \tan\left(\frac{\pi}{180}\right) = 0.0175\text{pL}. \tag{16}$$

In our case, we consider that the image is displayed on the monitor with $p = 57$ ppc and is to be observed at two different distances $L = \{25, 50\}$ cm so that, according to Eq. (16), the pixels per degree of visual angle are $d = \{25, 50\}$. Figure 3 shows the results of applying Eqs. (7) and (10), with $d = 50$ pixels/degree and $k = 5$, to the achromatic image component of channel A [$i = 0$, Fig. 3(a)]. Figure 3(b) shows the spatially filtered version of the image in Fig. 3(a), and it was obtained by convolution with the spatial filter $F_{di}(x, y)$ of Eq. (2) with $d = 50$ and $i = 0$. Figure 3(c) is the LoG term $k\text{Log}\{F_{d0}\} * I_0(x, y)$ that is to be subtracted from the original A component to produce the sharpened version $\text{ShI}_0(x, y)$ in Fig. 3(d). Note the double-edge distribution in Fig. 3(c) that emphasizes object contours. Figure 3(e) shows the spatially filtered version of the sharpened component in Fig. 3(d). The spatially filtered images Figs. 3(b) and 3(e) appear as blurred versions of the images Figs. 3(a) and 3(d), respectively, when they are shown with the same scale. But the viewing condition $d = 50$ pixels/degree implies that they would be seen with a scale reduced to a factor of 2. Thus the scaled versions of the spatially filtered images $I_{d0}(x, y)$ and $\text{ShI}_{d0}(x, y)$ are placed together for comparison in Fig. 3(f) as if they would be seen with $d = 50$ pixels/degree. In Figure 3(f), we realize the edge sharpening effects introduced in $\text{ShI}_{d0}(x, y)$ in comparison with $I_{d0}(x, y)$.

In this section we organize the following series of experiments:

- Experiment 1. To restrain the sharpening operation to the achromatic channel A, while keeping the chrominance channels C_1 and C_2 unchanged. The result is to be compared with the sharpening operation applied to the whole set of channels A, C_1, and C_2. The CIEDE2000 color differences between the resulting and the original images will be computed on the S-CIELAB basis for the sake of comparison.
- Experiment 2. Comparison of the conventional Laplacian-based sharpening operation $\mathrm{ShI}\nabla^2$ [Eq. (13)] with our proposed LoG-sharpening operation ShI [Eq. (10)] in terms of color variations and noise with respect to the original image. Again, the CIEDE2000 color differences between the original image and the image resulting from each sharpening operation will be computed on the SCIELAB basis [$\Delta E_{00}{}^{\mathrm{SCIELAB}}(I, \mathrm{ShI})$ and $\Delta E_{00}{}^{\mathrm{SCIELAB}}(I, \mathrm{ShI}\nabla^2)$]. We consider a set of ten regions of interest (ROIs) in the original image [Fig. 2(b)] to analyze the effects of noise and color variations. All ten ROIs have the same area (either 6×6 or 4×9 pixels). They show different but nearly uniform colors, and they are placed relatively far from edges or other contours. The signal-to-noise ratio (SNR) is the metric we use to evaluate noise in the image of the color differences between the sharpened and the original images [$\Delta E_{00}{}^{\mathrm{SCIELAB}}(I, \mathrm{ShI})$ and $\Delta E_{00}{}^{\mathrm{SCIELAB}}(I, \mathrm{ShI}\nabla^2)$]. Since edges and contours are sharpened by design, they contribute to have a large value of the standard deviation, not due to noise, but to the variation in local information. Consequently, the zones corresponding to edges and contours must be excluded from the estimation of noise. For this reason, the average SNR is calculated from the logarithm of the ratio of the contrast due to the structural difference ($V_{\max} - V_{\min}$) to the noise level represented by the standard deviation of the ROIs, according to the expression

$$\langle \mathrm{SNR} \rangle = \left(\frac{20}{N_{\mathrm{ROI}}} \right) \sum_{i \in \mathrm{ROI}} \log_{10} \left(\frac{V_{\max} - V_{\min}}{s_i} \right), \qquad (17)$$

where $V_{\max}$ and $V_{\min}$ are the maximum and minimum boundaries between which the image of the color differences lies, N_{ROI} is the number of ROIs, and s_i is the standard deviation of the iROI in the images of the color differences [either $\Delta E_{00}{}^{\mathrm{SCIELAB}}(I, \mathrm{ShI})$ or $\Delta E_{00}{}^{\mathrm{SCIELAB}}(I, \mathrm{ShI}\nabla^2)$]. The experiment will be repeated for different viewing distances.

- Experiment 3. The DoG operator [Eq. (14) with $s_2/s_1 = 1.6$] is taken in Eq. (10) as an approximation of the LoG operator. The results will be compared by computing the color differences on the SCIELAB basis.
- Experiment 4. We will look for the effects of the proposed method in terms of artifacts. We focus on possible fringes or color variations that may appear when rendering images caused by the lack of complete orthogonality of AC_1C_2 channels. We will consider tests of geometrical figures on uniform background, and we will analyze the characteristics of color variations in sharpened edges and contours.
- Experiment 5. We analyze the joint influence of the control parameter k and the viewing condi-

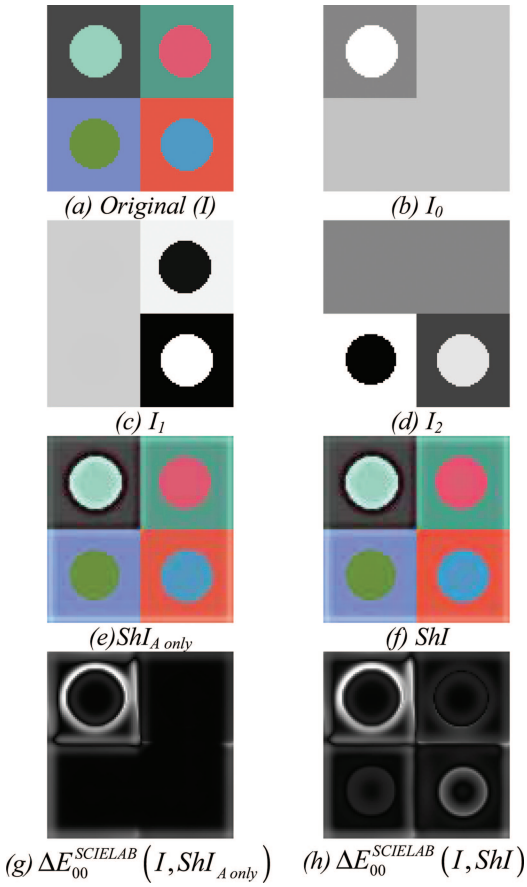

Fig. 4. (Color online) (a) Original image (I); (b) A component (I_0); (c) C_1 component (I_1); (d) C_2 component (I_2); LoG-sharpened images obtained by using Eq. (10) with $k = 5$ and $d = 50$ pixels/degree: (e) limited to the A channel, and (f) in the A, C_1, and C_2 channels. (g) CIEDE2000 color difference between the (e) and (a) image pair based on the S-CIELAB metric. (h) CIEDE2000 color difference between the (f) and (a) image pair based on the S-CIELAB metric.

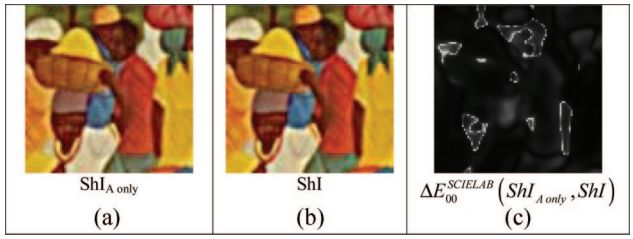

Fig. 5. (Color online) LoG-sharpened images obtained by using Eq. 10 with $k = 5$ and $d = 50$ pixels/degree: (a) limited to the A channel, and (b) in the A, C_1, and C_2 channels. (c) CIEDE2000 color difference between the (a) and (b) images based on the S-CIELAB metric. The data corresponding to the CIEDE2000 color differences of the processed whole images (of 385×289 pixels) are mean = 2.7197, std = 4.7788, max = 54.9434, min = 0.0036.

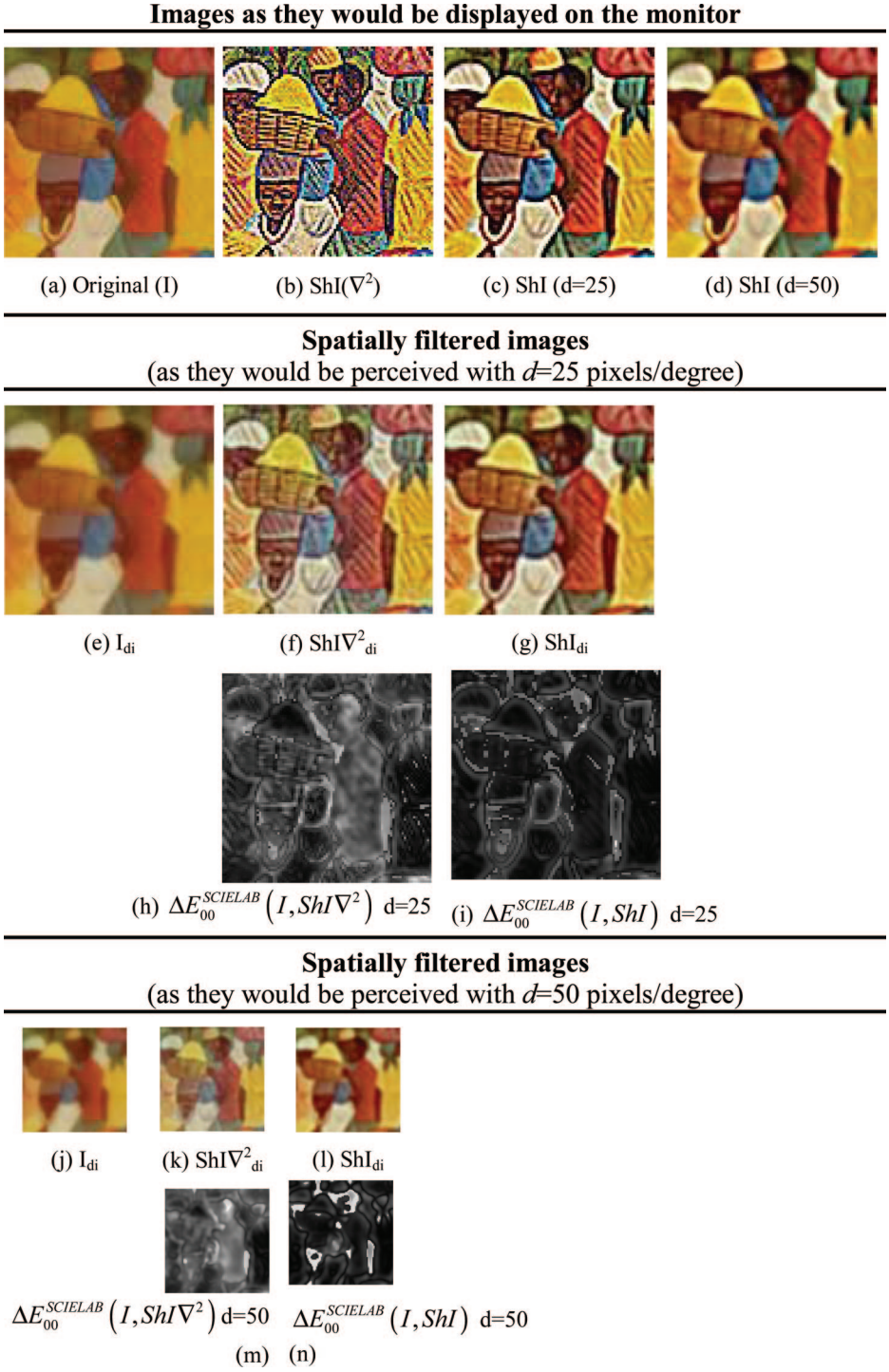

Fig. 6. (Color online) (a)–(d) Zone of the image of Fig. 2(a), displayed on the monitor with $p = 57$ ppc: (a) original, (b) sharpened image using the Laplacian [Eq. (13)], (c) sharpened image using the proposed LoG method [Eq. (10)] to be seen at $d = 25$ pixels/degree; (d) same as (c) but to be seen at $d = 50$ pixels/degree; (e)–(g) spatially filtered images of (a)–(c) for the viewing conditions of $d = 25$ pixels/degree; (h) and (i): color differences $\Delta E_{00}{}^{\mathrm{SCIELAB}}(I, \mathrm{ShI}\nabla^2)$ and $\Delta E_{00}{}^{\mathrm{SCIELAB}}(I, \mathrm{ShI})$ for the viewing condition of $d = 25$ pixels/degree; (j), (k), (l) spatially filtered images of (a), (b), (d), respectively, for the viewing condition of $d = 50$ pixels/degree; (m), (n) color differences $\Delta E_{00}{}^{\mathrm{SCIELAB}}(I, \mathrm{ShI}\nabla^2)$ and $\Delta E_{00}{}^{\mathrm{SCIELAB}}(I, \mathrm{ShI})$ for the viewing condition of $d = 50$ pixels/degree.

tions (d pixels/degree) in the LoG-sharpened image. With this experiment, we will try to reach some conclusion about the value of k for different viewing conditions d. The method will be applied to different images.

5. Results

A. Results of Experiment 1

Experiment 1 restrains the sharpening operation to just the achromatic channel A and keeps the chromi-

nance channels C_1 and C_2 unchanged. Figure 4 gives an example obtained for a test image consisting of four sectors. Each sector of the test has some A, C_1, or C_2 components constant [Figs. 4(a)–4(d)]. Figure 4(e) shows the result of using the LoG of the spatial filter [Eq. (10)] with $k = 5$ and $d = 50$ pixels/degree to sharpen only the A component of the test, keeping the components C_1 and C_2 constant, whereas Figure 4(f) shows the sharpened image in all its A, C_1, and C_2 components. Both sharpened images Figs. 4(e) and 4(f) are rather similar at first sight. However, looking at them in detail, we appreciate that only the top left sector, which exhibits variations in the A channel, has been sharpened in Fig. 4(e) and the rest of the sectors, with constant A values, are not sharpened. In Fig. 4(f) all sectors have been sharpened, although the clearest effects appear in the top left and the bottom right sectors. Evidence of this fact are provided in Figs. 4(g) and 4(h) that show the CIEDE2000 color differences computed between each sharpened version and the original image according to the S-CIELAB metric. In most of the images analyzed by us, the exclusive sharpening of the A channel produces good results, very close to those obtained by sharpening in all three channels. This can be seen in the example of Fig. 5. The S-CIELAB color differences between the whole processed images $\mathrm{ShI}_{\mathrm{A\ only}}$ and ShI, of 385 × 289 pixels are small as it can be appreciated the from the following statistics (in CIEDE2000 units): mean = 2.7197, std = 4.7788, max = 54.9434, min = 0.0036.

B. Results of Experiment 2

Figure 6 shows the sharpened images obtained by using the bare Laplacian operator [Eq. (13), represented by $\mathrm{ShI}\nabla^2$] and the LoG of the spatial filter in each channel [Eq. (10), represented by ShI] and compares them with the original image when they are seen at two distances, with $d = \{25, 50\}$ pixels/degree. We have considered $k = 7.5$ to make the differences between them more evident. In the first row, Figs. 6(a)–6(d), we can see the images as they would be displayed on a monitor with $p = 57$ ppc. Note that the LoG-sharpened image takes into account the distance at which it is going to be seen and, consequently, two different images are computed to be displayed on the monitor [Figs. 6(c) and 6(d)] for the distances $L = \{25, 50\}$ cm (equivalent to the viewing conditions of $d = \{25, 50\}$ pixels/degree). That is not the case of the image sharpened by using the Laplacian operator [Eq. (13)], which is an operation independent of the viewing conditions. This $\mathrm{ShI}\nabla^2$ image also shows a colored noise, as could be expected from this sort of operation, in contrast with the sharpened images of Figs. 6(c) and 6(d) that appear smoothed. A high value of k also produces rapid saturation in a large number of points in the displayed image level $\mathrm{ShI}\nabla^2$. In these points, values are truncated according to the considered dynamic range (8 bits). In such a case, Eq. (12) is no longer verified in a large number of points, that is

Table 2. Average Metrics of the ROIs in the SCIELAB ΔE_{00} Color Differences Computed between the Sharpened and Original Images[a]

	Mean CIEDE2000 Units	std CIEDE2000 Units	SNR dB
$\Delta E_{00}^{\mathrm{SCIELAB}}(I, \mathrm{ShI})$ $d = 25$	3.0043	1.6738	38.6370
$\Delta E_{00}^{\mathrm{SCIELAB}}(I, \mathrm{ShI}\nabla^2)$ $d = 25$	10.5977	3.1173	30.8695
$\Delta E_{00}^{\mathrm{SCIELAB}}(I, \mathrm{ShI})$ $d = 50$	1.5848	0.5330	42.7710
$\Delta E_{00}^{\mathrm{SCIELAB}}(I, \mathrm{ShI}\nabla^2)$ $d = 50$	9.9441	1.5266	35.1087

[a]A zone is shown in Fig. 6; $k = 7.5$ in all the sharpened images, and two distances $L = \{25, 50\}$ cm were considered ($p = 57$ ppc, $d = \{25, 50\}$ pixel/degree).

$$I_{di}(x, y) - k\nabla^2 I_{di}(x, y) \neq F_{di}(x, y) * \left[I_i(x, y) - k\nabla^2 I_i(x, y)\right]. \quad (18)$$

As a consequence, the spatially filtered image $F_{di}(x, y) * [I_i(x, y) - k\nabla^2 I_i(x, y)]$ has been taken into account for computing the S-CIELAB color differences.

To evaluate the color variation and noise associated with both the Laplacian and the LoG-based sharpening operations, we compute the CIEDE2000 (ΔE_{00}) color differences between the sharpened and the original images on the S-CIELAB basis [Figs. 6(h), 6(i), 6(m), and 6(n)]. Table 2 contains the nu-

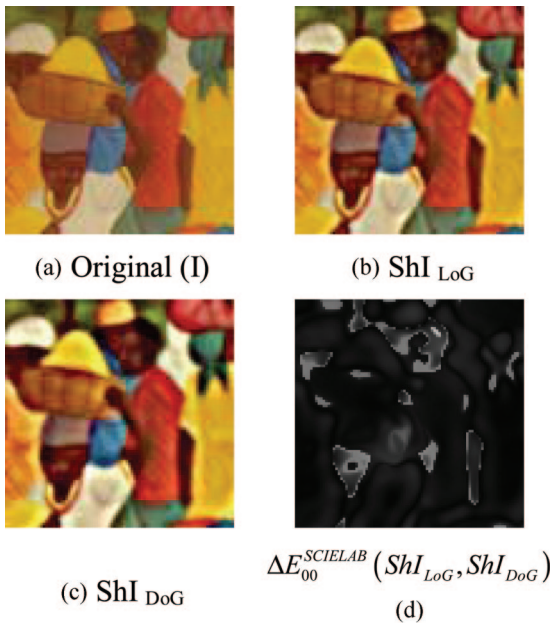

Fig. 7. (Color online) (a) Area of the original image (Fig. 2). Sharpened images obtained by using (b) the LoG operator [Eq. (10)], (c) the DoG [Eq. (14)] instead of LoG in Eq. (10). Values of $k = 5$ and $d = 50$ pixels/degree were used to compute (b) and (c). (d) Color difference between (b) and (c) image pair based on the S-CIELAB metric. Statistics of $\Delta E_{00}^{\mathrm{SCIELAB}}(\mathrm{ShI}_{\mathrm{LoG}}, \mathrm{ShI}_{\mathrm{DoG}})$ in CIEDE2000 units: mean = 6.3, std = 8.6, max = 112, min = 0.01.

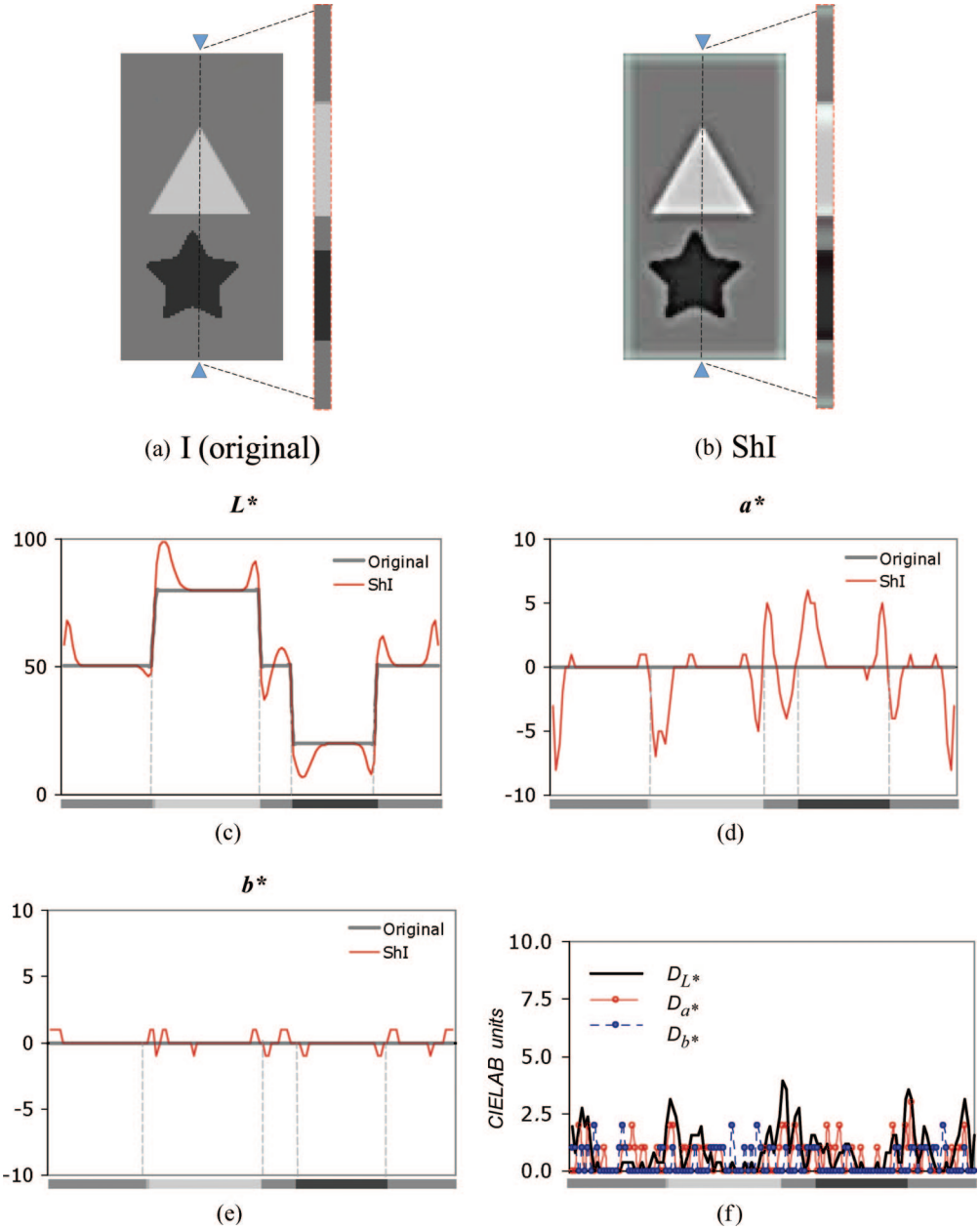

Fig. 8. (Color online) (a) Achromatic test with three gray levels: light (triangle), medium (background), dark (star). The column of pixels marked with arrows is analyzed in (c)–(f); (b) sharpened image with ($k = 5, d = 50$); (c)–(e) CIELAB coordinates of the pixels of the column in the original I (thick black curve) and the sharpened ShI (red line) images; (f) distortions [Eq. (19)].

merical results obtained for the set of ten ROIs defined in this experiment [Fig. 2(b)]. After sharpening, the color distortions should ideally be limited to the vicinity of the object contours to produce the desired edge enhancement and should decrease to negligible values in the uniformly colored areas of the image. This ideal situation is better approached by our LoG sharpening operator of Eq. (10) [Figs. 6(i) and 6(n)] than by the Laplacian-sharpening operator of Eq. (13) [Figs. 6(h) and 6(m)]. In fact, the average mean color differences evaluated in the ROIs shows a lower value and a lower standard deviation for $\Delta E_{00}{}^{\mathrm{SCIELAB}}(I, \mathrm{ShI})$ than for $\Delta E_{00}{}^{\mathrm{SCIELAB}}(I, \mathrm{ShI}\nabla^2)$ at the two distances considered. Moreover, this average value of the mean color differences decreases significantly with the viewing distance in the case of using our LoG-sharpening operator, whereas the decrease is very slow in the case of using the Laplacian-sharpening operator. As for noise, the $\mathrm{ShI}\nabla^2$ images show an increase in noise in comparison with the smoothed sharpened ShI images. Thus from Table 2, it can also be seen that the average SNR evaluated for the ROIs in the color-difference image $\Delta E_{00}{}^{\mathrm{SCIELAB}}(I, \mathrm{ShI}\nabla^2)$ is lower than the value obtained for $\Delta E_{00}{}^{\mathrm{SCIELAB}}(I, \mathrm{ShI})$ for both viewing conditions. For all these reasons, it can be said the LoG-sharpening operator is more conservative with the color of the

uniform areas and shows a much lower tendency to increase noise than does the Laplacian-sharpening operator.

C. Results of Experiment 3

We have approximated the LoG operator in Eq. (10) by the DoG operator defined in Eq. (14) to sharpen the image of Fig. 2(a). Figure 7 shows the results $\mathrm{ShI}_{\mathrm{LoG}}$ and $\mathrm{ShI}_{\mathrm{DoG}}$ for a part of the image, with $k = 5$ and $d = 50$, and Fig. 7(d) shows the part of the color difference between the image pair on the S-CIELAB basis. From the statistics of $\Delta E_{00}^{\mathrm{SCIELAB}}(\mathrm{ShI}_{\mathrm{LoG}},\mathrm{ShI}_{\mathrm{DoG}})$, the color differences are acceptable (mean = 6.3, std = 8.2, max = 112, min = 0.01 in CIEDE2000 units). Moreover, these differences are concentrated mainly in the vicinity of the sharpened edges as can be seen in Fig. 7(d) and as can be derived from the fact that the average of the mean and the standard deviations of the color differences computed for the ROIs in $\Delta E_{00}^{\mathrm{SCIELAB}}(\mathrm{ShI}_{\mathrm{LoG}}, \mathrm{ShI}_{\mathrm{DoG}})$ are very small quantities ($\langle\mathrm{mean}\rangle = 0.99$, $\langle\mathrm{std}\rangle = 0.29$, max = 1.70, min = 0.58 in CIEDE2000 units). Consequently, the approach is reasonably good in this case. The DoG operator is interesting because the spatial summation properties (excitatory center-inhibitory surround) of receptive fields of the retina have been modeled by DoG functions. In addition to this, there are clear advantages in applying the DoG operator since it can be computed more efficiently than that of the LoG. However, despite these advantages, we use the LoG-sharpening operator in the rest of the experiments for the sake of comparison of the results.

D. Results of Experiment 4

As stated in Ref. 13 the lack of complete orthogonality of the $\mathrm{AC_1C_2}$ channels may result in possible fringes or color variations when rendering images. We have looked for the artifacts derived from that statement in the images sharpened with the LoG operator. Figure 8(a) shows an achromatic test of geometrical figures. The gray levels are limited to light gray (triangle), medium gray (background), and dark gray (star). The test is achromatic by design to better show the possible color deviations introduced by the sharpening process. Figure 8(b) shows the LoG-sharpened image ShI with ($k = 5, d = 50$). A column of pixels marked with arrows in Figs. 8(a) and 8(b) has been selected to analyze the CIELAB values in both the original and the sharpened images [Figs. 8(c)–8(e)]. This column of pixels is placed in the abscissa axis of Figs. 8(c)–8(f). The L^* profiles of Fig. 8(c) show the results expected for the sharpened image with respect to the original. However, the a^* and b^* profiles of Figs. 8(d) and 8(e) show unexpected results. Although the a^* and b^* profiles of the original image column are flat (constant), as corresponding to an achromatic image, the a^* and b^* profiles of the sharpened image column are not. This fact is particularly notable for the a^* profile in Fig. 8(d), and it reveals the color distortions introduced by the sharpening process. For a proper comparison of both the original and the sharpened images we consider the color differences on the SCIELAB basis. For each spatially filtered image I_{di} and ShI_{di}, we have computed the ΔL, Δa, and Δb CIELAB differences between the neighbor pixels $(j, j + 1)$ of the column, that is, $\{\Delta L(j, j + 1), \Delta a(j, j + 1), \Delta b(j, j + 1)\}$. For each pixel of the column, we have calculated the differences between the ΔL, Δa, and Δb values corresponding to the ShI_{di} and I_{di} images, and we have taken the absolute value to obtain the distortions D in the CIELAB coordinates between both images. These distortions are then given by the set of expressions

$$\begin{aligned} D_{L^*} &= \left|\Delta L(j, j+1)_{\mathrm{ShI}_{di}} - \Delta L(j, j+1)_{I_{di}}\right|, \\ D_{a^*} &= \left|\Delta a(j, j+1)_{\mathrm{ShI}_{di}} - \Delta a(j, j+1)_{I_{di}}\right|, \\ D_{b^*} &= \left|\Delta b(j, j+1)_{\mathrm{ShI}_{di}} - \Delta b(j, j+1)_{I_{di}}\right|. \end{aligned} \tag{19}$$

Figure 8(f) plots D_{L^*}, D_{a^*}, and D_{b^*}. In this figure we see that the distortions of L^* (expected) and a^* and b^* (undesired) are comparable in magnitude. Nevertheless, the undesired color distortions have been estimated to be less than 2.5 CIELAB units, in general

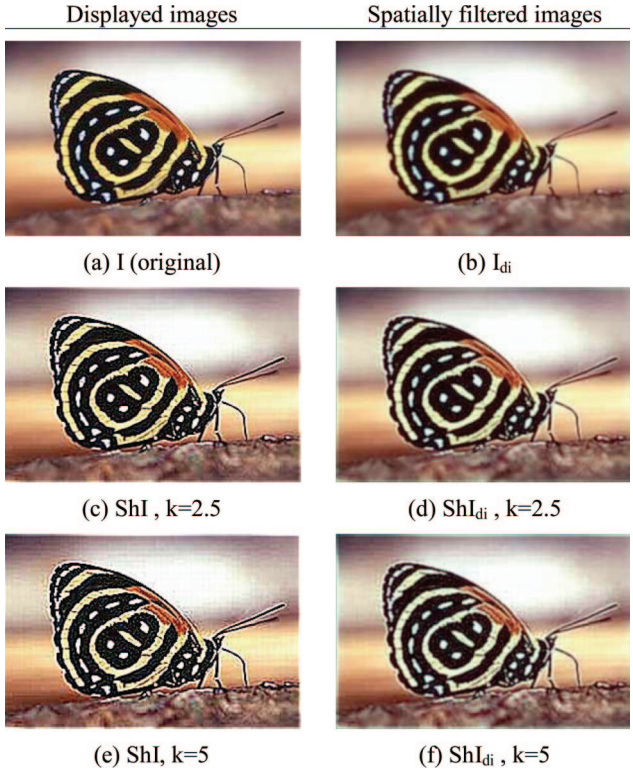

Fig. 9. (Color online) Butterfly, original image 300 × 197 pixels, displayed with 57 ppc to be seen at $L = 25$ cm (d = 25 pixels/degree). Artifacts appear when the sharpening LoG operator of Eq. (10) is used with high values of k. For instance in this figure halos in antennas and wings and pseudotexture in the background. Note that these artifacts are clearly visible for $k = 5$ not only in the displayed image (left column) but also in the spatially filtered image (right column).

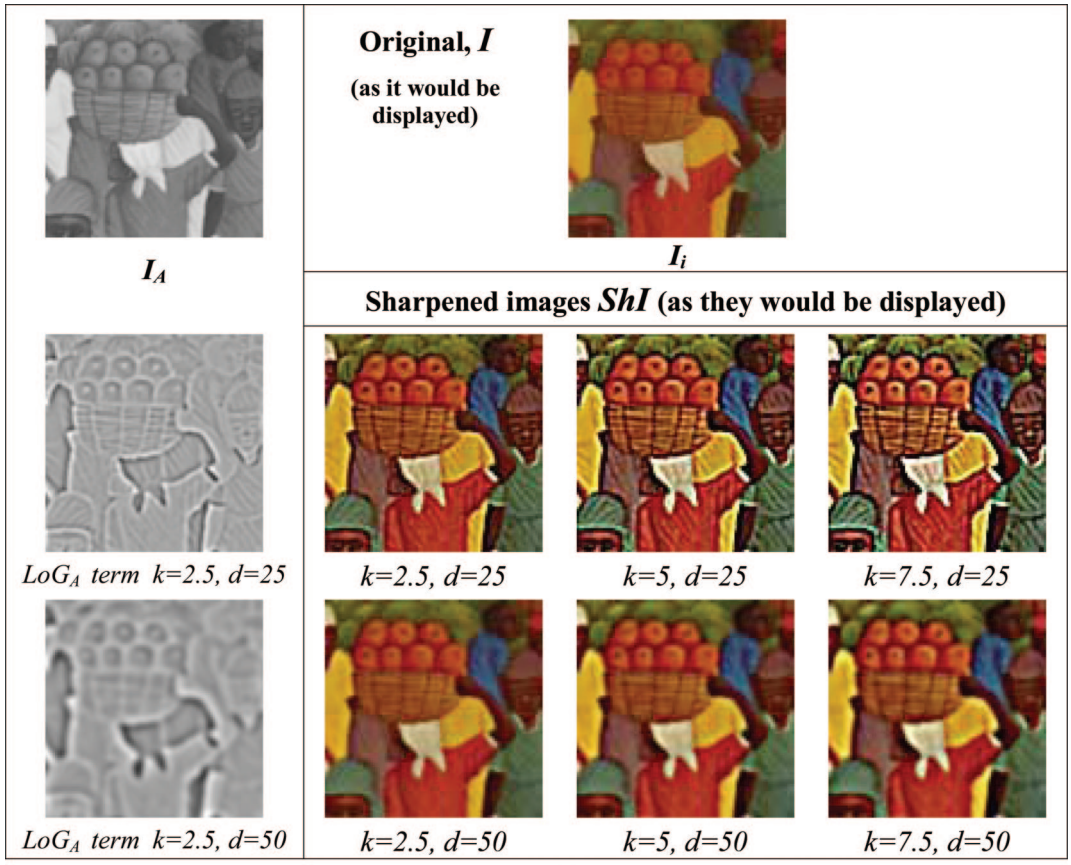

Fig. 10. (Color online) Dependence on $k = \{2.5, 5, 7.5\}$ and $d = \{25, 50\}$ pixels/degree. (a) Original image I and sharpened ShI images as they would be displayed. On the left, the A component of the original image and LoG terms in channel A. (b) Spatially filtered (original and sharpened) images as they would be perceived.

for the pixels of the column, and it reveals that such color distortions are of little relevance.

Figure 9 shows some artifacts that may appear when dealing with images that contain objects with high contrast and our LoG-sharpening operation is applied with an unnecessarily high value of k [Fig. 9(e)]. In this case, halos and a pseudotextured background can be perceptible even in the spatially filtered image [Fig. 9(f)].

E. Results of Experiment 5

As stated in Section 3, the sharpening operation represented by Eq. (10) varies with viewing conditions through the number of pixels per degree of visual

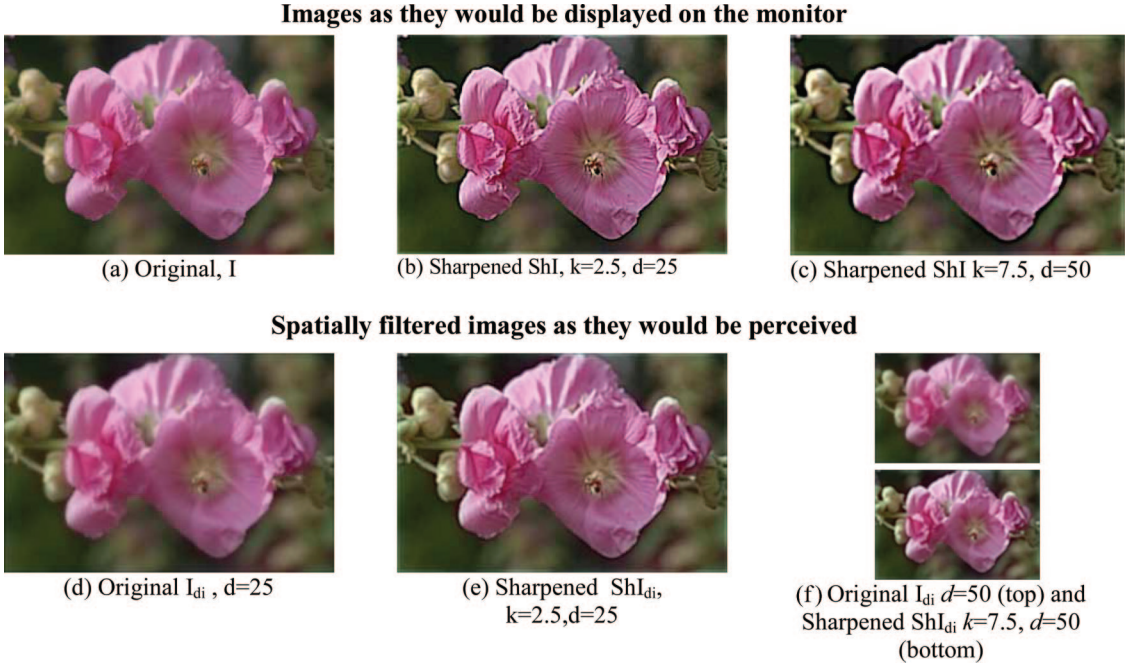

Fig. 11. (Color online) Original and sharpened images for $d = \{25, 50\}$ pixels/degree. First row, images as they are displayed with $p = 57$ ppc. Second row, spatially filtered images as they would be seen at distances $L = \{25, 50\}$ cm from the display. Note that (e) sharpening with low values of k is preferable when the image is to be seen at short viewing distances, whereas (f) higher values of k must be used to produce similar effects at longer viewing distances.

angle d. Since the monitor is assumed to display the original image with a fixed number of pixels/cm, the variations in the viewing distance are what determine the variations in d (pixels/degree) according to Eq. (16). In Fig. 10(a) on the left, an area of the A component of the original image and its corresponding LoG terms calculated for $d = 25$ pixels/degree and $d = 50$ pixels/degree are shown. For both LoG terms, parameter k was set to $k = 2.5$. At short viewing distances ($d = 25$), for which the spatial blurring is small, Eq. (10) sharpens most fine edges (for instance, basket lines, shadow lines in clothes, and details of the face) and object contours. At these short distances, some noise could also be emphasized. At long distances ($d = 50$), however, for which the spatial blurring is greater, Eq. (10) sharpens just the large figures and the most significant object contours (now, the basket lines and other fine details are no longer sharpened). Moreover, the spatial extension of the double edge produced by the LoG$\{F_{di}\}$ operator, which is subtracted from an image component for sharpening, varies with distance. Thus fine double edges are superposed when viewing the image at short distances, and thicker double edges are superposed at longer distances.

Figure 10(a) also contains the original and sharpened images as they would be displayed on a monitor in full color. Sharpened full color images were computed for different values of $d = 25, 50$ pixels/degree and sharpening depths ($k = 2.5, 5, 7.5$). All these images are more properly compared in the spatially filtered versions of Fig. 10(b), in which they appear as they would be perceived. When the sharpened image is to be seen at a short distance, an increase of parameter k tends to rapidly increase noise and gives an artificial appearance. On the other hand, when the sharpened image is to be seen at a long distance, the result changes much more slowly with k. In fact, it is necessary to consider higher values of k to have similar effects (Fig. 11).

6. Conclusions

A method to sharpen digital color images that takes into consideration human vision models and viewing conditions (pixels per degree of visual angle, estimated from both the pixels/cm displaying capability and the viewing distance) has been described. The method combines the LoG operator with the spatial filters that approximate the contrast sensitivity functions of human visual systems. The sharpening operation has been introduced in the opponent color space, following the scheme proposed in S-CIELAB. We deduced the degree of sharpening to introduce in the original image to obtain the spatially filtered image (that approaches the perceived image), LoG sharpened for a given viewing condition. Consequently, at short viewing distances, for which the spatial blurring is small, most fine edges and object contours are sharpened by adding narrow double edges. At these short distances, some noise can also be emphasized. On the other hand, at long distances, for which the spatial blurring is greater, just large figures are sharpened by adding thick double edges. Because of the smoothing effect of the Gaussian functions involved in the LoG operator, the proposed image sharpening does not tend to increase noise.

When the sharpening operation is limited exclusively to the achromatic channel, the results obtained are good. This is consistent with the high importance of the luminance channel in the spatial content of color images. When the sharpening is based on the Laplacian operator instead of on the LoG operator, the image sharpening does not adapt to the viewing conditions. In this case, the image sharpening tends to increase noise and distort colors, and the general appearance of the image deteriorates rather quickly with the depth of the sharpening operation. The LoG operator has been approached by a DoG operator, and the results obtained in sharpening color images are good. Some artifacts involving color distortions of little relevance were observed when rendering sharpened achromatic tests designed on purpose, but they were not imperceptible in other examples of more natural images. These artifacts are consequences of the fact that the three opponent color channels are not completely orthogonal. Thus, should such a case ever appear when rendering images, it would be convenient to limit the sharpening operation exclusively to the achromatic channel. The depth of the sharpening operation must be carefully applied, taking into account the viewing distance, to avoid overacting or producing artificial appearances. When the sharpened image is to be seen at a short distance, a low k value can lead to the desired result, whereas when the sharpened image is to be seen at a longer distance, we must considerably increase the k value to have a similar result.

The authors acknowledge the financial support of the Spanish Ministerio de Educación y Ciencia and the Fondo Europeo de Desarrollo Regional under project DPI2003-03931. E. Valencia acknowledges receipt of a grant from the Universidad Politècnica de Cataluña.

References

1. R. C. González, R. E. Woods, and S. L. Eddins, *Digital Image Processing Using MATLAB* (Prentice-Hall, 2004).
2. S. Di Zenzo, "A note on the gradient of a multi-image," Comput. Vis. Graph. Image Process. **33,** 116–125 (1986).
3. J. Weickert, "Coherence-enhancing diffusion of colour images," Image Vis. Comput. **17,** 201–212 (1999).
4. N. Sochen, R. Kimmel, and R. Malladi, "A general framework for low level vision," IEEE Trans. Image Process. **7,** 310–318 (1998).
5. R. Kimmel, R. Malladi, and N. Sochen, "Images as embedded maps and minimal surfaces: movies, color, texture, and volumetric medical images," Int. J. Comput. Vis. **39,** 111–129 (2000).
6. C.-K. Yang, T.-C. Wu, J.-C. Lin, and W.-H. Tsai, "Color image sharpening by moment-preserving technique," Signal Process. **45,** 397–403 (1995).
7. M. Vanrell, R. Baldrich, A. Salvatella, R. Benavente, and F. Tous, "Induction operators for a computational colour-texture representation," Comput. Vis. Image Underst. **94,** 92–114 (2004).
8. J. C. Russ, *The Image Processing Handbook,* 4th ed. (CRC, 2002).
9. M. S. Millán and E. Valencia, "Colour image sharpening using color difference based operators," in *Proceedings of the Tenth Congress of the International Colour Association* (Granada, 2005), pp. 1055–1058.
10. X. Zhang and B. A. Wandell, "A spatial extension of CIELAB for digital color image reproduction," SID Int. Digest Tech. Papers **27,** 731–734 (1996).
11. X. Zhang, D. A. Silverstein, J. E. Farrell, and B. A. Wandell, "Color image quality metric S-CIELAB and its application on halftone texture visibility," in *Proceedings of IEEE COMPCON* (IEEE, 1997), Vol. 97, pp. 44–51.
12. M. Mirmehdi and M. Petrou, "Segmentation of color textures," IEEE Trans. Pattern Anal. Mach. Intell. **22,** 142–159 (2000).
13. G. M. Johnson and M. D. Fairchild, "A top down description of S-CIELAB and CIEDE2000," Color Res. Appl. **28,** 425–435 (2003).
14. M. R. Luo, G. Cui, and B. Rigg, "The development of the CIE 2000 colour-difference formula: CIEDE2000," Color Res. Appl. **26,** 340–350 (2001).
15. S. Westland, "Models of the visual system and their application to image-quality assessment," in *Proceedings of the Tenth Congress of the International Colour Association* (Granada, 2005), pp. 309–312.
16. B. A. Wandell, *Foundations of Vision* (Sinauer, 1995).
17. P. Kruizinga and N. Petkov, "Computational model of dot-pattern selective cells," Biological Cybern. **83,** 313–325 (2000).
18. T. T. Norton, D. A. Corliss, and J. E. Bailey, *The Psychophysical Measurement of Visual Function* (Butterworth-Heinemann, 2002).
19. D. Marr and E. Hildreth, "Theory of edge detection," Proc. R. Soc. London, Ser. B **207,** 187–217 (1980).
20. IEC 61966-2-1 and Basic sRGB Math are available at http://www.srgb.com/basicsofsrgb.htm.
21. R. Berns, *Billmeyer and Saltzman's Principles of Color Technology* (Wiley, 2000).
22. A. B. Poirson and B. A. Wandell, "The appearance of colored patterns: pattern-color separability," J. Opt. Soc. A **10,** 2458–2470 (1993).
23. A. Huertas and G. Medioni, "Detection of intensity changes with subpixel accuracy using Laplacian-Gaussian masks," IEEE Trans. Pattern Anal. Mach. Intell. **8,** 651–664 (1986).
24. S. R. Gunn, "On the discrete representation of the Laplacian of Gaussian," Pattern Recogn. **32,** 1463–1472 (1999).
25. http://white.stanford.edu/~brian/scielab/scielab.html.

Diferencias de color entre dos ejemplares del atlas de color Munsell

Opt. Pura y Apl. **38**(2), 57-65 (2005).

Diferencias de color entre dos ejemplares del atlas de color Munsell

Colour differences between two individual collections of Munsell colour chart

Edison Valencia, María S. Millán

Departamento de Optica y Optometría, Universidad Politécnica de Cataluña, 08222 Terrassa (Barcelona), España. E-mail: millan@oo.upc.edu

RESUMEN:
Las muestras de un atlas de color pueden experimentar variaciones en su color de referencia, dependiendo de su antigüedad, estado de conservación, uso, etc. En este trabajo medimos las diferencias de color existentes entre pares de muestras que tienen la misma especificación pero que pertenecen a dos libros distintos del atlas de color Munsell. Utilizamos un espectrorradiómetro para medir el color bajo iluminación D65. Calculamos las diferencias de color en las métricas CIELAB y CIEDE2000 y las comparamos con otras distancias: el error instrumental y la diferencia de color de cada una de las muestras del par con sus vecinos más próximos dentro de la propia colección a la que pertenece. El estudio se realiza sobre los ejemplares de dos libros Munsell de muestras mate: la colección de colores casi neutros (*Nearly Neutral Munsell Collection*) y el libro de colores (*Munsell Book of Colours*). Las diferencias de color llegan a alcanzar 1 unidad CIELAB en las muestras de la región del amarillo.

Palabras Clave: diferencias de color, CIELAB, CIEDE2000, atlas de color Munsell

ABSTRACT:
A colour chart consists of a collection of patches whose reference colour may vary depending on their age, keeping conditions, use, etc. In this work we measure the colour differences between sample pairs with the same specification but belonging to two individual books of the Munsell chart. A spectroradiometer is used for colour measurements under D65 illumination and CIELAB and CIEDE2000 metrics are considered for colour difference calculation. The colour differences are then compared with other distances: the instrumental uncertainty and the colour differences between each pair sample and their respective nearest neighbour samples within the particular collection to which they belong. The study is carried out on two individual Munsell books of matte colour samples: the *Nearly Neutral Munsell Collection* and the *Munsell Book of Colours*. The colour differences reach one unity CIELAB in the case of patches belonging to the yellow colour region.

Keywords: colour difference, CIELAB, CIEDE2000, Munsell colour chart

REFERENCIAS Y ENLACES

[1] Vocabularios del color, Comité español del color – Sociedad Española de Óptica. 2002.

Recibido: .9 Dec 2004

[2] **http://www.munsell.com**
[3] G. Wyszecki and W.S. Stiles, *Color Science. Concepts and Methods, Quantitative Data and Formulae*, John Wiley & Sons, Inc. New York (1982).
[4] R. S. Berns, *Billmeyer and Saltzman's Principles of Color Technology*, 3rd ed., Wiley, New-York (2000).
[5] Luo MR, Cui G, Rigg B., "The development of the CIE 2000 colour-difference formula: CIEDE2000", Color Research and Application **26** (5), 340-350 (2001).
[6] Gaurav Sharma, Wencheng Wu, Edul N. Dalal, "The CIEDE2000 color difference formula: Implementation notes, supplementary test data, and mathematical observations," submitted to Color Research and Application (2004).
[7] G.. Johnson, M. D. Fairchild, "A top down description of S-CIELAB and CIEDE2000," Color Research and Application **28** (6), 425-435 (2003).
[8] M. Melgosa, M.M. Pérez, A. Yebra, R. Huertas, E. Hita, "Algunas reflexiones y recientes recomendaciones internacionales sobre evaluación de diferencias de color", Optica Pura y Aplicada **34**, 1-10 (2001).
[9] M. Melgosa, E. Hita, A. J. Poza, D. H. Alman, R. S. Berns, "Suprathreshold color-difference ellipsoids for surface colors," Color Research and Application **22** (3), 148-155 (1997).

1.- Introducción

Un atlas de color es una colección de muestras de colores dispuestas e identificadas según reglas específicas [1], que sirven como guía de referencia para orientar la selección del color a usar y como indicador de control de calidad. Los atlas de color (por ejemplo, Pantone, Munsell) son utilizados ampliamente en distintos ámbitos: gestión del color (caracterización, calibración y puesta a punto de dispositivos, imagen digital), arte de impresión, arquitectura (doméstica, decoración), industria (igualación del color, diseño e inspección), ciencia, artes plásticas, moda, etc. También son muy utilizados algunos tests o cartas que constan de un pequeño número de muestras, como la *GretagMacbeth Color-Checker*. Uno de los atlas más utilizados en el campo de la ciencia del color y en la industria es el atlas Munsell [2]. Una muestra de color en el sistema Munsell está definida como un punto con tres dimensiones: *Munsell Hue* (H), *Munsell Value* (V) y *Munsell Chroma* (C), que se escriben como H V/C, fórmula conocida como "Notación Munsell".

Las muestras de un atlas pueden experimentar variaciones en su color de referencia, dependiendo de la antigüedad de las muestras, las horas de uso, las condiciones de almacenamiento, el estado de conservación, etc. Por esta razón, aunque dos personas empleen el mismo atlas de referencia, puede suceder que una determinada especificación de color se corresponda con muestras cuyo color real no sea idéntico, dependiendo de la colección o libro concreto en el que se encuentren. Así pues, existe una incertidumbre en la definición del color asociada al hecho de utilizar un ejemplar concreto de un atlas.

En este trabajo analizamos el problema de las variaciones de color en material impreso debidas principalmente a la distinta edición, si bien no se excluye la incidencia de otras causas como el envejecimiento y el uso. El problema es tanto más grave por cuanto el material impreso del que se trata es un atlas de color, que se usa como referencia para especificar el color, mediante la asignación de valores a los atributos perceptivos de claridad, tono y croma.

Para llevar a cabo el análisis mediremos las diferencias de color existentes entre pares de muestras que tienen la misma especificación pero que pertenecen a distintos ejemplares del atlas de color Munsell. Utilizamos un espectrorradiómetro y una iluminación determinada para efectuar las medidas. Empleamos la formulación CIELAB [3,4] y la fórmula más reciente CIEDE2000 [5] para el cálculo de las diferencias de color, ΔE^*_{ab} y ΔE_{00}, respectivamente. Comparamos las diferencias de color calculadas con otras distancias:

- el error instrumental y
- la distancia o diferencia de color de cada una de las muestras del par con sus vecinos más próximos dentro de la colección a la que pertenece.

2.- Diseño del experimento

Comparamos las muestras mate de dos libros Munsell distintos: la colección de muestras casi neutras (*Nearly Neutral Munsell Collection*) y el libro de color (*Munsell Book of Colors*). Estos dos libros fueron adquiridos simultáneamente (fecha de certificación 07/2002, fecha de vencimiento

07/2004) y se han conservado juntos en nuestro laboratorio, en las mismas condiciones ambientales de temperatura y humedad controladas.

El test de muestras a analizar es un conjunto de muestras mate que está formado por diez grupos distribuidos de forma regular alrededor del círculo de tono Munsell (Fig. 1a). Cada grupo H_i, con i={5R, 5YR, 5Y, 5GY, 5G, 5BG, 5B, 5PB, 5P, 5RP} está formado por un conjunto de muestras cuyos valores Munsell de Valor y Croma son $(V/C)_i$={6/2, 7/1, 7/2, 7/4, 8/2}. La muestra central del grupo es H_i 7/2 y, alrededor de ella, se distribuyen cuatro muestras vecinas (Fig. 1b). Todas las muestras del test están contenidas tanto en la colección Munsell de colores casi neutros, como en el libro de colores Munsell. De este modo, podemos cubrir el objetivo de medir la diferencia de color que presentan los pares de muestras con igual especificación pero pertenecientes a dos ejemplares distintos del atlas Munsell.

En esta experiencia se ha empleado una cabina de observación con iluminación controlada proveniente de un simulador D65 (lámpara fluorescente F40/T12 con temperatura correlacionada de color 6438K y observador de 10º). Se utilizó una geometría de iluminación/observación aproximada de 45/0. La iluminación directa se veía ligeramente incrementada por la luz que, tras ser reflejada difusamente por las paredes de la cabina, incidía sobre la muestra. Como blanco de referencia se ha utilizado la placa Photoresearch RS-3. La reflectancia espectral de esta placa es aproximadamente constante e igual a 1 (su calibración no excedió de ±0.6% respecto a los valores de la fuente calibradora de referencia, dentro del intervalo 380-780nm). Como instrumento de medida, se ha empleado un espectroradiómetro *Photo Research PR-715*. Todas las medidas fueron efectuadas en pocos días, tres meses después de la fecha límite de vencimiento de la certificación por el laboratorio Munsell fabricante. De cada muestra se obtuvieron su reflectancia espectral, los valores triestímulos CIE XYZ y las coordenadas CIELAB en las condiciones de iluminación y observación descritas. Se calcularon las diferencias de color en la métrica CIELAB [3,4]. También se han calculado las diferencias de color en la métrica CIEDE2000 [5,6], asimismo recomendada por la CIE más recientemente. En la Ref. [7] la métrica CIEDE2000 ha sido considerada más adecuada para evaluar muestras con valores bajos de croma.

El error instrumental al medir las coordenadas CIELAB de cada muestra, expresado en términos de la "media de las diferencias de color de las medias" (MCDM, iniciales de su nombre en inglés *'Mean Colour Difference from the Mean'* [4]), se ha determinado antes de iniciar la experiencia siguiendo el procedimiento indicado en la Ref. 4. A partir de un conjunto de medidas CIELAB, en nuestro caso 10, consecutivamente tomadas de puntos distintos de una muestra, se calcula el valor medio $(\overline{L}^*, \overline{a}^*, \overline{b}^*)$. A continuación se calcula la diferencia de color entre cada medida individual y el promedio $(\overline{L}^*, \overline{a}^*, \overline{b}^*)$. Para ello utilizamos dos formulas de diferencias de color, ΔE^*_{ab} y ΔE_{00}. El valor medio de las diferencias de color calculadas es el MCDM. Se ha calculado el MCDM de un conjunto de 10 muestras Munsell contenidas en el test (centros de grupo) (Fig. 1), alcanzándose valores de MCDM $<\Delta E^*_{ab}>$=0.025 unidades CIELAB y $<\Delta E_{00}>$=0.020 unidades CIEDE2000.

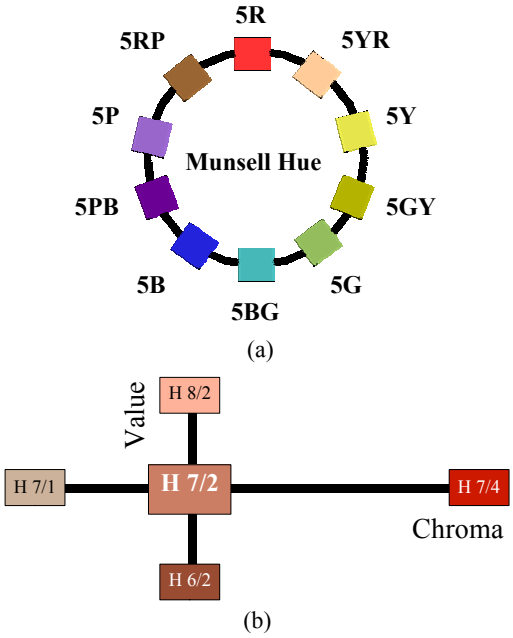

Fig. 1.- Esquema del test de muestras: (a) distribución de grupos sobre el círculo de tono Munsell, (b) composición de cada grupo en una muestra central y cuatro vecinas (del Munsell Book of Colors).

Como se ha dicho, nuestro interés es medir y analizar las diferencias de color entre pares de muestras que responden a una misma especificación de color en dos ejemplares concretos de la colección Munsell. Nos interesa asimismo conocer la importancia que tienen las variaciones de luminancia, croma o tono en la diferencia de color existente entre muestras nominalmente iguales.

Por otra parte, en cada libro de los dos considerados, la muestra central de cada grupo aparece rodeada de modo distinto por sus muestras vecinas. En el caso del libro de color Munsell, los vecinos inmediatos de cada centro de grupo son los mismos que se representan en la Fig. 1(b). En el caso del libro Munsell de colores casi neutros, los vecinos

del centro de grupo son colores más próximos, con pasos de 0.5 tanto en los valores de Value como de Chroma (Fig. 2). Obsérvese que las muestras que ocupan el centro y los extremos de este grupo de la Figura 2 tienen una especificación coincidente con el centro y los extremos del grupo representado en la Figura 1(b).

Para completar nuestra experiencia, compararemos las diferencias de color obtenidas entre los pares de muestras nominalmente iguales, pertenecientes a libros distintos, con las diferencias de color existentes entre el centro de cada grupo y sus vecinos más inmediatos dentro de cada libro. En el caso del libro de colores Munsell se tendrán en cuenta los cuatro vecinos representados en la Figura 1(b), mientras que para el libro de colores casi neutros se tendrán en cuenta los diez vecinos representados en la Figura 2.

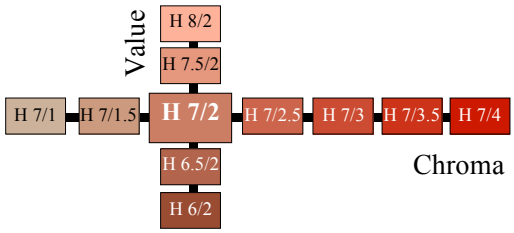

Fig. 2.- Composición de cada grupo en una muestra central y diez vecinas de la colección Nearly Neutral Munsell.

3.- Resultados

En la Figura 3 representamos los resultados de las diferencias de color CIELAB ΔE^*_{ab} (línea azul) y CIEDE2000 ΔE_{00} (línea roja) obtenidas para los pares de muestras de la misma especificación nominal pertenecientes a los dos libros Munsell. En la Figura 3 se presentan, sobre cinco diagramas circulares de tono Munsell, las diferencias de color obtenidas para cada uno de los valores $(V/C)_i$={6/2, 7/1, 7/2, 7/4, 8/2}, con i={5R, 5YR, 5Y, 5GY, 5G, 5BG, 5B, 5PB, 5P, 5RP}. De esta forma, la figura 3(a) presenta las diferencias de color para los pares muestras con $(V/C)_i$ = 7/2, la figura 3(b) para los pares de muestras con $(V/C)_i$ = 6/2, la figura 3(c) para los pares de muestras con $(V/C)_i$ = 7/1, la figura 3(d) para los pares de muestras con $(V/C)_i$ = 7/4 y la figura 3(e) para los pares de muestras con $(V/C)_i$ = 8/2. En cada diagrama circular, la dimensión radial representa la magnitud de la diferencia de color en las unidades correspondientes al gráfico considerado (CIELAB para el gráfico azul y CIEDE2000 para el gráfico rojo). Las diferencias de color medidas en CIEDE2000 son de menor magnitud que las medidas en CIELAB. Todos los valores de diferencias de color medidos son, en general, muy superiores al error instrumental.

Como característica común, se observa en estas figuras que las diferencias de color más altas se dan en la amplia región de los tonos cálidos: rojos, naranjas, amarillos y amarillo verdosos (R, YR, Y y GY), mientras que las diferencias más pequeñas se dan para los tonos fríos: púrpura y verde (P y G). Las diferencias de color en la región de tonos azules, entre el verde y el púrpura, tienen valores intermedios, relativamente bajos en comparación con la región ya señalada del amarillo-rojo.

En la tabla I se presentan las mismas diferencias de color pero promediadas para cada tono. Junto a los valores medios de las diferencias de color en unidades CIELAB (ΔE^*_{ab}) y en unidades CIEDE2000 (ΔE_{00}), se indican sus respectivas desviaciones estándar. En la última fila de la tabla I se calculan los valores globales de la media y la desviación estándar para todos los tonos considerados. La media global de las diferencias es relativamente baja, con un valor de 0.59 y una desviación estándar de 0.34 en unidades CIELAB y de 0.44, con una desviación estándar de 0.26, en unidades CIEDE2000.

Los tonos cálidos (R, YR, Y y GY) tienen en media diferencias de color mayores a 0,9 unidades CIELAB (la mayor diferencia se obtiene para el tono Y cuyo valor medio es de 1,05) lo que representa valores por encima del umbral justamente perceptible, situado entre 0.38 y 0.73 unidades CIELAB [8]. Quiere esto decir que, en esta región cromática, las diferencias de color entre los pares de muestras de igual especificación, pertenecientes a los dos libros Munsell considerados, pueden ser percibidas por una persona que observe las muestras en las condiciones adecuadas. Si bien las diferencias de color medidas por nosotros en esta región no alcanzan el valor supraumbral de 1.75 unidades CIELAB [9] relacionado con la tolerancia de color o aceptabilidad de la diferencia de color, también es cierto que no se quedan tan lejos. Aunque se trata de un tema controvertido en general, en el caso de un atlas parece razonable elevar el nivel de exigencia, por parte del fabricante, en la reproducción del color de las muestras que componen el atlas y en la conservación de sus atributos durante un periodo de vida útil relativamente largo. Este periodo de vida debe ser tenido en cuenta por los usuarios del atlas.

Profundizando un poco más, nos preguntamos qué tipo de variación, en las dimensiones de luminancia, croma y tono, es la que más influye en la diferencia de color medida entre muestras con la misma especificación de color pero pertenecientes a libros distintos.

(a)

(b)

(c)

(d)

(e)

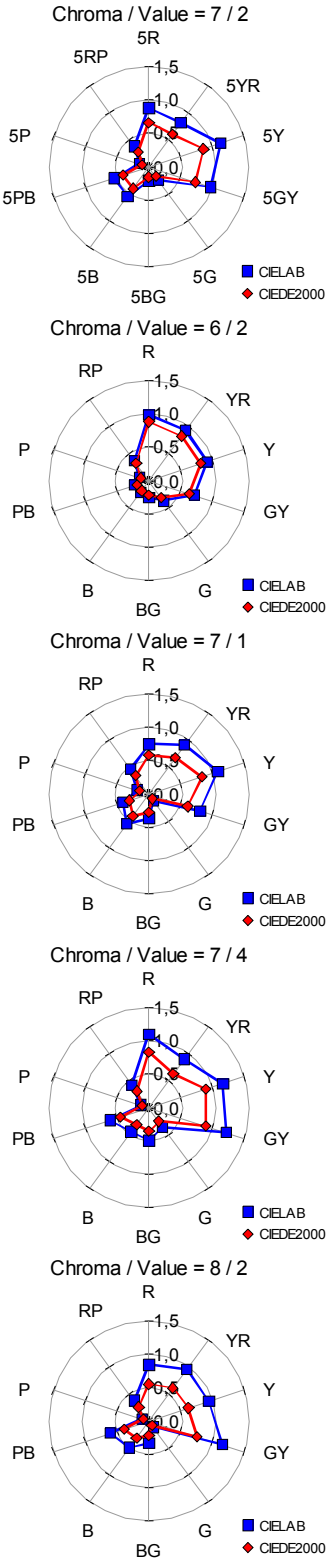

Fig. 3.- Diferencias de color (CIELAB en azul, CIEDE2000 en rojo) entre pares de muestras de igual denominación Munsell pertenecientes a libros diferentes. Valores agrupados por $(V/C)_i$ igual a: (a) 7/2, (b) 6/2, (c) 7/1, (d) 7/4 y (e) 8/2.

Tabla I – Diferencias de color entre pares de muestras de igual denominación Munsell pertenecientes a dos libros diferentes. Valores agrupados y promediados por región de tono.

CIELAB

Color		ΔE^*_{ab}	$\Delta L^*/\Delta E^*_{ab}$	$\Delta C^*_{ab}/\Delta E^*_{ab}$	$\Delta H^*_{ab}/\Delta E^*_{ab}$
R	Media	0,911	0,980	0,065	-0,172
	σ	0,137	0,016	0,033	0,079
YR	Media	0,902	0,968	0,104	-0,069
	σ	0,055	0,053	0,235	0,025
Y	Media	1,048	0,988	-0,068	-0,063
	σ	0,111	0,011	0,128	0,052
GY	Media	0,975	0,983	0,080	0,019
	σ	0,215	0,010	0,172	0,065
G	Media	0,243	0,907	-0,216	-0,021
	σ	0,123	0,120	0,303	0,239
BG	Media	0,332	0,946	0,004	0,112
	σ	0,110	0,045	0,327	0,075
B	Media	0,452	0,980	0,044	0,127
	σ	0,140	0,018	0,134	0,087
PB	Media	0,477	0,978	0,157	-0,010
	σ	0,164	0,023	0,121	0,088
P	Media	0,143	-0,430	0,330	-0,371
	σ	0,026	0,729	0,357	0,228
RP	Media	0,401	0,963	0,050	-0,192
	σ	0,039	0,042	0,134	0,148
	Media	**0,588**	**0,826**	**0,055**	**-0,064**
	σ	**0,335**	**0,442**	**0,142**	**0,150**

CIEDE2000

Color		ΔE_{00}	$\Delta L'/\Delta E_{00}$	$\Delta C'/\Delta E_{00}$	$\Delta H'/\Delta E_{00}$
R	Media	0,702	0,966	0,117	-0,202
	σ	0,146	0,031	0,063	0,108
YR	Media	0,667	0,981	0,094	-0,094
	σ	0,092	0,022	0,153	0,033
Y	Media	0,806	0,989	-0,054	-0,084
	σ	0,108	0,012	0,111	0,051
GY	Media	0,724	0,989	0,055	0,029
	σ	0,115	0,005	0,125	0,083
G	Media	0,184	0,900	-0,238	-0,003
	σ	0,105	0,130	0,283	0,265
BG	Media	0,244	0,931	0,032	0,117
	σ	0,076	0,062	0,371	0,083
B	Media	0,326	0,978	0,001	0,147
	σ	0,089	0,016	0,132	0,092
PB	Media	0,347	0,968	0,164	-0,013
	σ	0,100	0,032	0,141	0,154
P	Media	0,115	-0,420	0,227	-0,481
	σ	0,018	0,667	0,400	0,271
RP	Media	0,300	0,947	0,058	-0,214
	σ	0,032	0,070	0,176	0,180
	Media	**0,442**	**0,823**	**0,046**	**-0,080**
	σ	**0,255**	**0,438**	**0,128**	**0,185**

En la tabla I se incluyen, para la métrica CIELAB las relaciones ($\Delta L^*/\Delta E^*_{ab}$), ($\Delta C^*_{ab}/\Delta E^*_{ab}$), ($\Delta H^*_{ab}/\Delta E^*_{ab}$) y para CIEDE2000, las relaciones ($\Delta L'/\Delta E_{00}$), ($\Delta C'/\Delta E_{00}$), ($\Delta H'/\Delta E_{00}$). En general, se observa que la variación de la luminancia es la que tiene mayor peso en la diferencia de color medida entre las muestras de ambos libros. Las otras variaciones de croma y tono tienen un peso relativo en la diferencia de color muy similar entre sí y muy inferior al de la luminancia. Este efecto nos

lleva a concluir que incluso en las regiones de tono de mayor diferencia de color entre ambos libros, estas diferencias se deben fundamentalmente a variaciones de luminancia (claro-oscuro), permaneciendo bastante estable la cromaticidad de las muestras (dada por el tono y el croma). No obstante, podemos señalar el caso curioso del tono púrpura (P) que, por una parte, obtiene las menores diferencias de color para los pares de muestras de ambos libros (media de 0.105 unidades CIEDE2000) y, por otra parte, tiene más repartido el peso relativo de las variaciones de luminancia, croma y tono.

La figura 4 ilustra directamente los valores de la luminancia versus el croma para las muestras de cada grupo H_i en los dos libros. En cada uno de los diez diagramas se representan elementos en forma

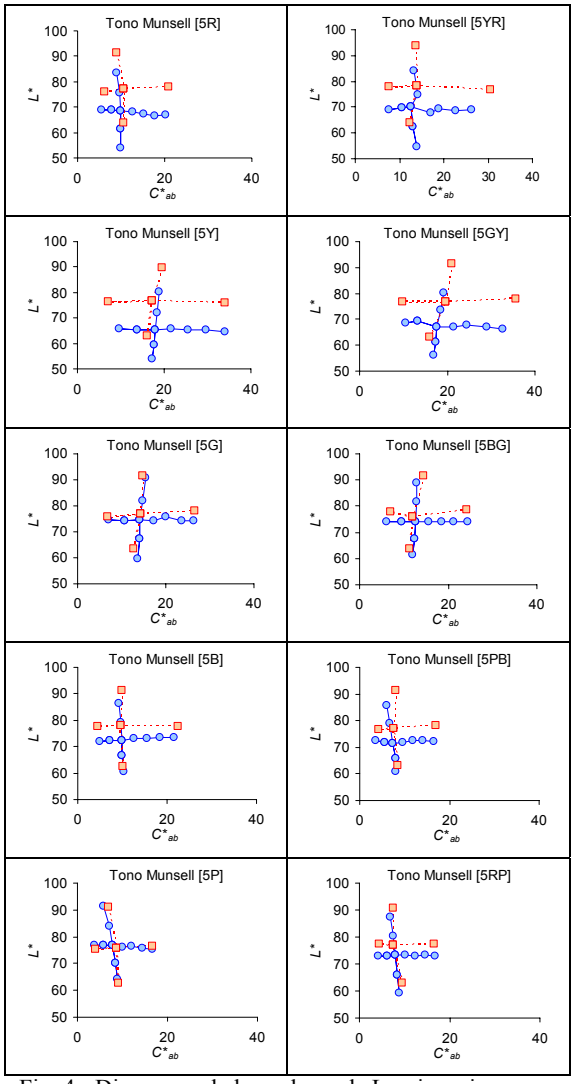

Fig. 4.- Diagramas de los valores de Luminancia versus Croma para los diez grupos de tono H_i (Fig. 1(a)). En rojo se representan los grupos del libro Munsell de Color (Fig. 1(b)) y en azul los grupos del libro Munsell de Colores Casi Neutros (Fig. 2).

de cruz, que corresponden al centro de grupo y a sus vecinos. Los elementos dibujados en línea roja unen los puntos correspondientes a las cinco muestras extraídas del *Munsell Color Book* según la composición de los grupos de la figura 1(b). Los elementos dibujados en línea azul unen los puntos correspondientes a las once muestras extraídas del libro *Nearly Neutral Munsell Collection* según la composición de los grupos mostrada en la figura 2.

En cada figura, cabe resaltar la diferente posición de estos elementos en cruz que, aun siendo similares en forma, aparecen afectados por un desplazamiento relacionado principalmente con la luminacia (L). En la Fig. 4 este desplazamiento es máximo en el tono amarillo verdoso (5GY) y mínimo en los tonos púrpura (5P) y verde (5G).

Por último, compararemos las diferencias de color entre los pares compuestos por los centros de grupo, con igual denominación pero pertenecientes a distinto libro Munsell (Figura 3(a)), con las diferencias de color entre cada centro de grupo del par con los vecinos de su mismo libro. Con ello pretendemos conocer si la diferencia de color debida al cambio de libro puede ser alguna vez mayor que las distancias a las muestras más próximas dentro de un mismo libro.

En la Figura 5 se muestra un diagrama circular, en el que se representan las diferencias de color CIELAB y CIEDE2000 con respecto a los centros de grupo H_i 7/2. La línea gruesa negra (etiquetada con la letra *o*) corresponde a las diferencias medidas entre pares de muestras (centros de grupo) de igual especificación pero de libro distinto. En trazos continuos, finos y de diferente color, se representan las diferencias de color entre el centro y los vecinos de cada grupo de muestras extraídas del libro Munsell de colores casi neutros. En trazos similares, pero discontinuos, se representan las diferencias de color entre el centro y los vecinos de cada grupo de muestras extraídas del libro Munsell de color.

Del análisis de la Figura 5 se deduce que la incertidumbre en la definición del color asociada al cambio de libro (línea de trazo grueso, *o*) puede englobar la incertidumbre asociada a la variación de color entre muestras vecinas de un mismo ejemplar (líneas de trazo fino). Tan sólo para los tonos verde (5G), verde azulado (5BG) y púrpura (5P) la diferencia de color asociada al cambio de libro es inferior a las distancias de la muestra (centro de grupo) a todos sus vecinos inmediatos en ambos libros. En los restantes tonos se presentan mayores y más variados niveles de incertidumbre. Así, por ejemplo, en el otro extremo, los tonos 5GY, 5Y, 5YR, 5R, 5PB y 5B, presentan una diferencia de color asociada al cambio de libro superior a las diferencias de color introducidas por variaciones de (-1.0 Chroma) en ambos libros Munsell (líneas *i* y *j* en la Figura 5).

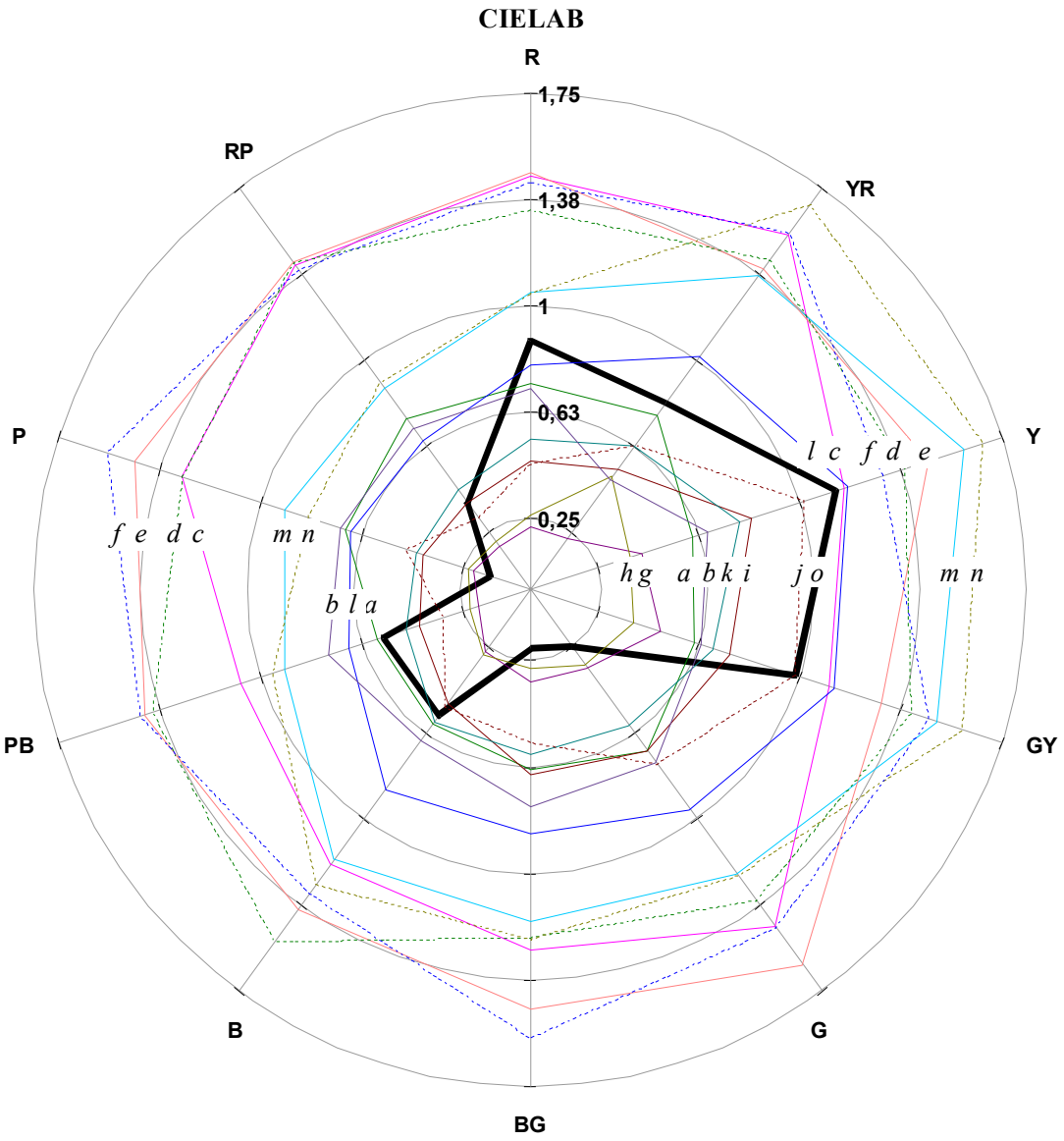

[*a*] -0,5 Value	[*d*] -1,0 Value	[*g*] -0,5 Chroma	[*j*] -1,0 Chroma	[*m*] +2,0 Chroma
[*b*] +0,5 Value	[*e*] +1,0 Value	[*h*] -0,5 Chroma	[*k*] +1,0 Chroma	[*n*] +2,0 Chroma
[*c*] -1,0 Value	[*f*] +1,0 Value	[*i*] -1,0 Chroma	[*l*] +1,5 Chroma	[*o*] igual referencia

(a)

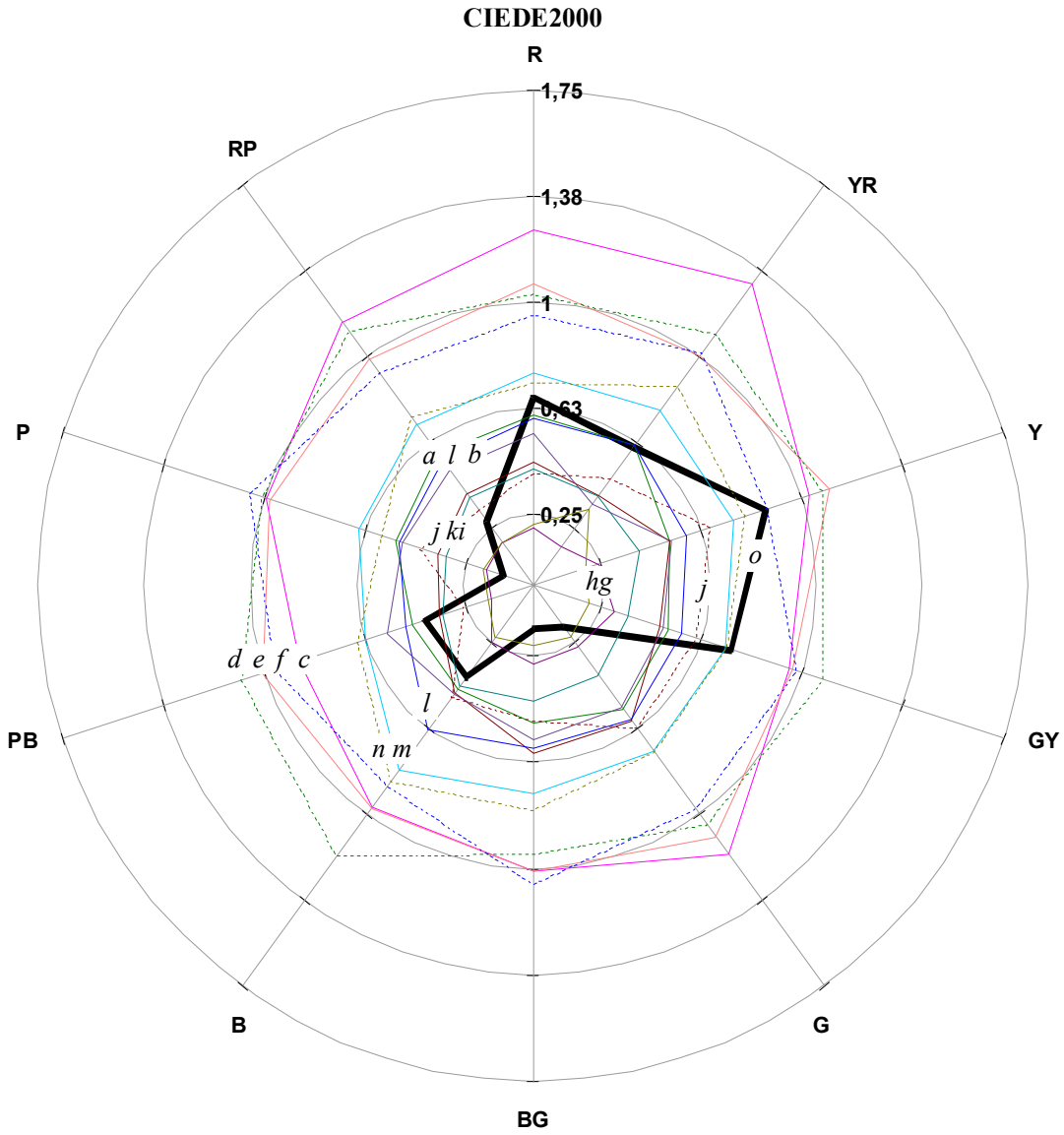

[*a*] -0,5 Value	[*d*] -1,0 Value	[*g*] -0,5 Chroma	[*j*] -1,0 Chroma	[*m*] +2,0 Chroma
[*b*] +0,5 Value	[*e*] +1,0 Value	[*h*] -0,5 Chroma	[*k*] +1,0 Chroma	[*n*] +2,0 Chroma
[*c*] -1,0 Value	[*f*] +1,0 Value	[*i*] -1,0 Chroma	[*l*] +1,5 Chroma	[*o*] igual referencia

(b)

Fig. 5.– Diferencias de color CIELAB (a) y CIEDE2000 (b) entre cada centro de grupo (H_i 7/2) y otra muestra correspondiente a: una muestra de igual especificación nominal que el centro de grupo pero de distinto libro Munsell (trazo grueso negro), o bien, una muestra que representa una variación de Munsell Value y Munsell Chroma en los libros Munsell de color (trazos finos discontinuos) y Munsell de colores casi neutros (trazos finos continuos).

4.- Conclusiones

Concluimos que, para los dos ejemplares de libros Munsell analizados existe una diferencia de color perceptible entre pares de muestras con la misma especificación Munsell de color. Los ejemplares (*Nearly Neutral Munsell Collection* y *Munsell Book of Colors*) contienen muestras mate, tenían algo más de dos años de antigüedad en el momento de efectuar las medidas, tiempo que superaba en tres meses la fecha de vencimiento de la certificación establecida por el

fabricante. En el test de muestras analizadas, esta diferencia de color era muy pequeña en los tonos fríos (verde, verde azulado y púrpura), pero era comparativamente elevada en los tonos cálidos (amarillo-rojo), llegando a alcanzar en estos últimos el valor de 1 unidad CIELAB. La variación en luminancia era la dimensión que incidía con mayor peso relativo en la diferencia de color existente entre muestras con la misma especificación y de libro distinto. La incidencia relativa de las variaciones de croma y tono era mucho menor que la de la luminancia y estaba más equilibrada. Este efecto nos llevó a concluir que incluso en las regiones de mayor diferencia de color entre ambos libros, estas diferencias son fundamentalmente variaciones de luminancia (claro-oscuro), permaneciendo bastante estable la cromaticidad de las muestras.

En los casos de mayor diferencia de color debida al cambio de libro, se llega a dar la circunstancia de que esta distancia es superior a la que existe entre una muestra y sus vecinas, dentro de un mismo libro. Este hecho constituye una fuente de incertidumbre o ambigüedad que, en general, no es evaluada por los usuarios de estos atlas y que puede dar lugar a errores inaceptables en la especificación de un color.

Los autores de este trabajo desconocen en qué medida las conclusiones extraídas en este trabajo para dos ejemplares concretos del Atlas Munsell pueden extenderse o generalizarse a otros ejemplares del mismo atlas o de atlas diferentes. Tampoco conocen la causa o las causas que pueden dar lugar al fenómeno descrito. No pueden excluirse defectos de impresión en la fabricación de las muestras ya que es bien conocida la dificultad técnica de la reproducción del material impreso. Sin profundizar en tales consideraciones, sí puede recomendarse a los usuarios de los atlas de color realizar regularmente una evaluación de la posible inconsistencia en el color de las muestras del libro concreto que utilizan, a fin de acotar el margen de ambigüedad introducido en la especificación del color, así como de hacer un seguimiento del estado del ejemplar que permita su uso correcto.

Agradecimientos

Los autores agradecen la financiación del Ministerio de Educación y Ciencia (proyecto Nº DPI2003-03931), fondos FEDER y de la Generalitat de Catalunya (Red temática, referencia 2003XT-00081). Edison Valencia agradece a la Universitat Politècnica de Catalunya una beca predoctoral.

Evaluación objetiva de la hiperemia de la conjuntiva tarsal superior mediante análisis de imagen. Ensayo preliminar

Revista Española de Contactología **12**, 9-15 (2005).

REV. ESP. CONTACT. 2005; 12: 9-15

ARTÍCULO ORIGINAL

EVALUACIÓN OBJETIVA DE LA HIPEREMIA DE LA CONJUNTIVA TARSAL SUPERIOR MEDIANTE ANÁLISIS DE IMAGEN. ENSAYO PRELIMINAR

OBJECTIVE ASSESSMENT OF UPPER PALPEBRAL HYPERAEMIA BY IMAGE ANALYSIS. PRELIMINARY RESULTS

MILLÁN MS[1], PÉREZ-CABRÉ E[1], ABRIL HC[2], VALENCIA E[3]

RESUMEN

Introducción: Las complicaciones oculares producidas por el uso de lentes de contacto (LC) suelen evaluarse por inspección visual directa, pudiendo utilizar series estándar de fotografías o ilustraciones como referencia comparativa.

Objetivo: Definir un método, basado en el procesado de imagen en color, como apoyo para la gradación objetiva de la hiperemia de la conjuntiva tarsal superior.

Material y método: Se usan las imágenes de la escala CCLRU *(Cornea and Contact Lens Research Unit)* para extraer la información que permite discriminar entre los diferentes grados. Se aplica un preprocesado de imágenes que permite comparar áreas similares en todas ellas. Como las imágenes RGB *(Red, Green, Blue)* del estándar CCLRU no están calibradas colorimétricamente, el análisis del contenido de color trata de establecer una metodología inicial de trabajo, más que extraer medidas definitivas.

Resultados y conclusiones: Se han extraído parámetros de la estadística de las imágenes analizadas, en las áreas centrales del interior

SUMMARY

Introduction: Ocular disorders caused by contact lens wear are usually graded by specialists using visual inspection. They usually have standard series of photographs or illustrations as a reference for comparison.

Purpose: In this work, a method for the objective assessment of upper palpebral hyperaemia by applying different colour image processing techniques is described.

Method: In this initial stage, we consider the images that compose the Cornea and Contact Lens Research Unit (CCLRU) grading scale to extract the information on which the different grades of severity can be discriminated. An image preprocessing allows us to compare areas of similar size. Since the RGB images of the CCLRU standard are not colourimetrically calibrated, our analysis of their colour content is addressed to establish an initial methodology of work rather than to obtain ultimate measurements.

Results and conclusions: The features extracted from the statistics of the analysed images, particularly in the central inner area of

Grupo de Óptica Aplicada y Procesado de Imagen (www.goapi.upc.edu).
[1] Doctora en Ciencias Físicas (millan@oo.upc.edu, eperez@oo.upc.edu).
[2] Doctor Ingeniero de Sistemas Informáticos (hector.abril@oo.upc.edu).
[3] Ingeniero Superior y Máster en Ingeniería de Sistemas Informáticos (edison@oo.upc.edu).
Los autores manifiestan que no tienen ningún interés comercial ni económico en ninguno de los productos citados en este texto.

Correspondencia:
Elisabet Pérez-Cabré
Grupo de Óptica Aplicada y Procesado de Imagen
Departamento de Óptica y Optometría
Escuela Universitaria de Óptica y Optometría de Terrassa
Universidad Politécnica de Cataluña
C/. Violinista Vellsolá, 37
08222 Terrassa (Barcelona)
España

del párpado, que presentan un comportamiento diferenciado para los diferentes grados de conjuntivitis, y sobre ellos se puede establecer el método de apoyo para la evaluación objetiva. Disponer de series de imágenes estándar, colorimétricamente calibradas, hubiera permitido un análisis de imagen más preciso.

Palabras clave: Imagen biomédica, análisis de imagen, conjuntivitis papilar, hiperemia de la conjuntiva tarsal superior, escalas de gradación.

the eyelid, show enough variation for the different grades of conjunctivitis, so that an objective evaluation method can be based on them. A new standard series of colourimetrically calibrated images would be convenient for an improved and more precise image analysis..

Key words: Biomedical image, Image analysis, papillary conjunctivitis, upper palpebral, hyperaemia,grading scales.

INTRODUCCIÓN

El uso de lentes de contacto (LC) puede producir complicaciones oculares que requieren ser evaluadas por los contactólogos. Hay cartas estándar, compuestas por series de fotografías o ilustraciones, que establecen escalas de gradación para algunos de estos cuadros clínicos (1-3). Estas cartas son comúnmente utilizadas como una referencia que permite comparar visualmente el ojo del paciente con la escala estándar correspondiente. La inspección por comparación visual da lugar a resultados que pueden diferir de un evaluador a otro por diversas razones, como la apreciación personal, los condicionantes externos, etc., todo lo cual es causa de una alta dispersión y una falta de objetividad en la evaluación del problema ocular.

En la literatura publicada sobre el tema pueden encontrarse algunas propuestas, basadas en el análisis de imagen, para cuantificar de manera objetiva ciertas complicaciones oculares derivadas del uso de LC (4-8). Hasta el momento, sin embargo, la mayoría de estos estudios concentran sus esfuerzos en el análisis de la hiperemia en la conjuntiva bulbar, lo cual realizan aplicando técnicas de procesado de imagen y segmentación sobre imágenes en niveles de gris o binarias. El trabajo de Wolffsohn y Purslow (9) es más amplio, abarca el análisis de cuatro tipos de problemas oculares. Entre las características que considera relacionadas con el color incluye la intensidad relativa de los componentes rojo (R), verde (G) o azul (B) respecto de la intensidad total de la imagen.

En este trabajo se pretende analizar la hiperemia de la conjuntiva tarsal superior a partir de la serie de fotografías de la escala CCLRU (fig. 1). Centraremos la atención en este tipo de problema, para el cual, la información del color de la imagen puede ser determinante a la hora de realizar una estimación correcta del estado de un paciente. Es especialmente oportuno desarrollar este tipo de estudio por cuanto que las propuestas realizadas hasta el momento para analizar el color son escasas y simples, y raramente van más allá del análisis directo de las componentes RGB de la imagen. Las técnicas de análisis de imagen en color deben ser utilizadas para extraer las características más relevantes de este tipo de problema ocular. Por ello, el propósito del trabajo es definir una serie de parámetros que describan la gravedad y evolución del problema y permita aplicar un método de gradación objetiva.

Figura 1.- Escala estándar CCLRU (Cornea and Contact Lens Research Unit) para la gradación de la hiperemia de la conjuntiva tarsal superior (grados de 1 a 4).

MATERIAL Y MÉTODOS

Pre-procesado de imagen

Una evaluación precisa de las escalas estándar requiere asegurar que la extracción de características se realiza sobre regiones similares en área. También implica que las imágenes se han captado en unas condiciones comparables y bajo control colorimétrico. Las imágenes que se utilizarán son fotografías en color digitalizadas, en formato JPEG, de componentes R, G, B, que se han obtenido directamente del portal de CCLRU en Internet (10). En la serie estándar CCLRU se aprecia que las imágenes son de diferente calidad (fig. 1). La iluminación no es uniforme en el plano de la imagen y el área de interés —la conjuntiva tarsal superior— no se muestra de igual modo en todas las fotografías. En alguna imagen se aprecia un ligero desenfoque. Puesto que pretendemos obtener medidas objetivas de la evolución del problema, debemos aplicar un pre-procesado de las imágenes que permita compararlas en condiciones similares para toda la serie de imágenes estándar.

En primer lugar, es necesario determinar la región de interés en la que deben evaluarse los efectos producidos por la LC. En segundo lugar, para asegurar que se analiza la misma área en todas las fotografías de la serie, se aplica una transformación polinomial a cada imagen. Esta operación consiste en aplicar una transformación geométrica por la cual las distancias entre los puntos (píxeles) de una imagen se modifican para asemejarse a los de otra imagen de referencia, al menos en alguna región de interés que ambas imágenes contienen (11).

La carta CCLRU contiene una copia adicional de la fotografía del grado 2 en la que el área comprendida entre el borde palpebral superior y la línea de eversión presenta sobreimpresa una subdivisión en cinco áreas etiquetadas por los números 1...5 (fig. 2a). De ellas, las áreas centrales 1, 2 y 3 son las más relevantes (2). Se ha aplicado un esquema de subdivisión de áreas en todas las imágenes del estándar análogo al de la figura 2a. En cada imagen, los píxeles son interpolados y ajustados de modo que los contornos de la zona de interés (borde palpebral superior y línea de eversión) se hacen coincidir con los de la imagen de grado 2. La figura 2b presenta los puntos que se han considerado para el ajuste. Hay seis puntos centrales (señalados con el símbolo ⊗) distribuidos regularmente en los límites entre las áreas

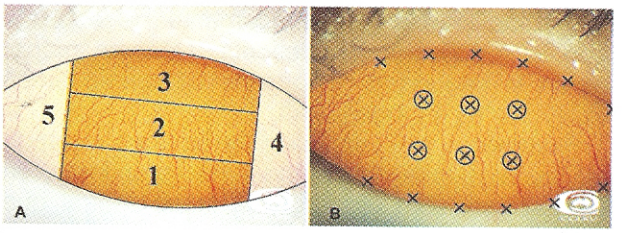

Figura 2.- A: Regiones de interés para la evaluación de la hiperemia de la conjuntiva tarsal superior, mostradas en la carta CCLRU sobre la imagen de grado 2. B: Puntos de ajuste sobre los que se aplica la transformación polinomial.

etiquetadas como 1, 2 y 3 en la figura 2a. Además, hay otros doce puntos (con el símbolo ×) distribuidos sobre el borde palpebral superior y la línea de eversión. Es importante que estos puntos de ajuste puedan marcarse en todas las figuras cuya transformación se pretenda realizar. La forma de ambos contornos (borde del párpado y línea de eversión) puede describirse matemáticamente, con buena aproximación, mediante parábolas. Para calcular estas parábolas, se seleccionan tres puntos sobre cada uno de los contornos superior e inferior de la zona de interés y se realiza el ajuste matemático. Las prolongaciones de las parábolas superior e inferior se cortan en dos puntos de intersección, que permiten definir el eje de inclinación de la zona de interés de la conjuntiva tarsal. Trazando rectas paralelas y perpendiculares a este eje de inclinación, se logra reproducir para cada imagen el esquema de subdivisión de áreas 1... 5 representado en la figura 2a. Salvo en la selección supervisada de los puntos sobre los que se ajustan las parábolas, el proceso de subdivisión de la conjuntiva tarsal en las áreas 1... 5 puede automatizarse por completo, mediante un programa de cálculo que se ejecute sobre la imagen digitalizada del párpado evertido.

La figura 3 muestra el resultado de aplicar la transformación polinomial a la imagen CCLRU de grado 1. El análisis de la serie se realiza sobre las zonas centrales de las imágenes una vez que han

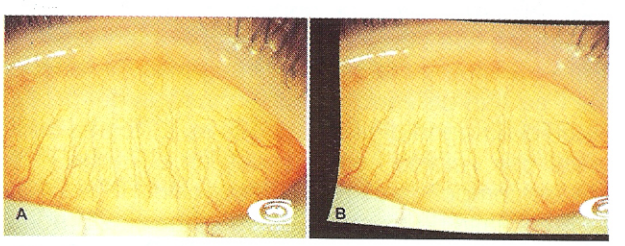

Figura 3.- Ejemplo de la transformación polinomial aplicada al estándar CCLRU de grado 1: A) imagen original; B) imagen transformada.

sido modificadas geométricamente de acuerdo con la transformación descrita. De este modo, existe la seguridad de que se comparan áreas equivalentes en todas ellas.

Finalmente, la iluminación de la zona captada en las imágenes del estándar no es uniforme en ningún caso. Sin embargo, la parte central que incluye las áreas 1, 2 y 3 muestra mayor uniformidad, siendo estas áreas sobre las que se lleva a cabo el estudio.

Análisis del color

Las imágenes RGB de la serie estándar presentan algunas limitaciones importantes que impiden realizar un estudio colorimétrico completo. Así, por ejemplo, no se dispone de la caracterización de la sensibilidad espectral de la cámara utilizada en la adquisición de las imágenes. Tampoco se conocen las condiciones de iluminación, ni la distribución espectral de la energía radiante de la fuente de luz. No obstante, a pesar de estas limitaciones, se utilizarán algunas herramientas de procesado de imagen en color y se aplicarán sobre la información contenida en las imágenes. De este modo podrá determinarse, de manera aproximada, su utilidad potencial. Se trata de extraer aquellos parámetros de las imágenes cuyo valor varía de forma significativa a lo largo de la escala. Esto permitirá establecer una correspondencia entre los valores de dichos parámetros y el grado de hiperemia, lo que podrá facilitar su evaluación objetiva y gradación. Los resultados pueden ser útiles para establecer una metodología de trabajo que se aplicaría, posteriormente, sobre los valores colorimétricos de imágenes correctamente calibradas.

Siguiendo la aproximación descrita, se parte de las imágenes en el espacio RGB (fig. 4a) y se realiza un análisis directo de los componentes rojo (R), verde (G) y azul (B). A continuación, se les aplica una transformación que permite representar las imágenes en el espacio de color perceptual HSI (fig. 4b), cuyas componentes son el tono (H, del inglés hue), la saturación (S) y la intensidad (I). Para transformar la serie de imágenes de la Figura 1 se han utilizado fórmulas clásicas del procesado de imagen digital (12), que se aplican a cada píxel con valores normalizados en el rango [0,1] de los componentes R,G,B (ecuación 1).

En el caso de disponer de imágenes calibradas, la conversión se haría del espacio RGB, dependiente del dispositivo de captura, a un espacio de color perceptualmente uniforme. Es práctica habitual utilizar el espacio CIELAB (CIE *L*a*b**) (fig. 4c) para realizar esta conversión (13,14).

RESULTADOS

Componentes RGB

Se analizarán los componentes RGB de las imágenes estándar en el área central del párpado

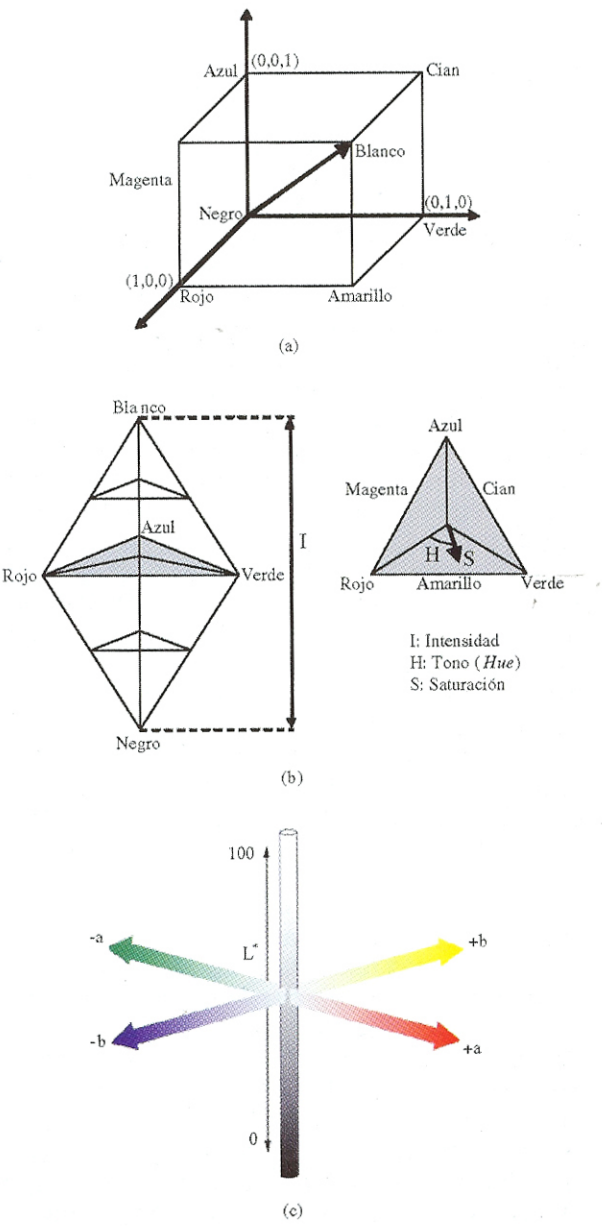

Figura 4.- Espacios de color considerados en el trabajo: a) RGB, b) HSI, c) CIELAB.

$$I = \frac{1}{3}(R = G - B)$$

$$H = \cos^{-1}\left[\frac{\frac{1}{2}[(R-G)+(R-B)]}{\left[(R-G)^2+(R-B)(G-B)\right]^{1/2}}\right]$$

$$S = 1 - \frac{3[min(R,G,B)]}{R+G+B}$$

Ecuación 1.

evertido, concretamente en las zonas marcadas como 1, 2 y 3 en la figura 2a. Todas las zonas de un mismo tipo contienen el mismo número de píxeles en todas las imágenes consideradas. La figura 5 muestra los histogramas RGB de las zonas 1, 2 y 3 de las imágenes, desde el grado 1 hasta el grado 4. La comparación de estos histogramas permite visualizar la evolución en la gravedad del problema. Los resultados obtenidos muestran un comportamiento similar en las tres zonas evaluadas. Las variaciones más relevantes en los histogramas RGB se producen en el valor medio del histograma de la componente verde (G) y en la desviación estándar de la componente azul (B). A medida que el grado aumenta, el valor medio del histograma verde disminuye (el modo del histograma verde se desplaza hacia los valores de gris bajos) y la desviación estándar de la componente azul también disminuye (el modo del histograma azul se hace un pico más estrecho y agudo) (fig. 5). Estas dos magnitudes, adecuadamente combinadas, han de tenerse en cuenta para una evaluación objetiva del grado de hiperemia de la conjuntiva tarsal superior.

Componentes HSI

Se aplica la transformación matemática de la ecuación 1 a los píxeles de los componentes RGB de cada imagen para obtener las nuevas componentes en el espacio HSI. Se utiliza esta transformación como una aproximación que permite redistribuir el contenido de color de la imagen en los componentes de tono (H), saturación (S) e intensidad (I), con un significado claramente más perceptual.

La figura 6 muestra los histogramas normalizados de los componentes HSI de las zonas 1, 2 y 3

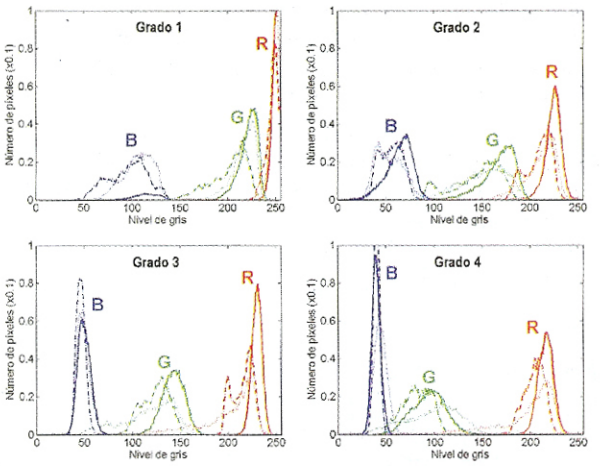

Figura 5.- Histogramas normalizados de las componentes RGB de las regiones 1 (línea punteada), 2 (línea continua) y 3 (línea discontinua) de las imágenes CCLRU (fig. 1).

de las cuatro imágenes estándar de la serie. A primera vista, esta figura no presenta mayor ventaja que la figura 5 construida a partir de los histogramas de las componentes RGB. Sólo la componente de la saturación muestra una variación clara en su histograma desde la imagen de grado 1 a la imagen de grado 4. El valor medio del histograma de la saturación aumenta con el grado, mientras que su desviación estándar disminuye, de modo que el pico del histograma se hace cada vez más estrecho. Se obtiene un comportamiento equivalente para las tres zonas centrales del párpado evertido que se han analizado.

Como la figura 6 no mostraba resultados más esclarecedores que la anterior, se decidió realizar otro tipo de representación de los componentes en el espacio HSI. Teniendo en cuenta que la variación del componente I es relativamente pequeña en las gráficas de la figura 6, puede considerarse menos informativa que los otras dos componentes de tono (H) y saturación (S). Por tanto, se considera I aproximadamente constante para las zonas centrales de las imágenes que componen la serie estándar y se grafica la proyección de los componentes H y S sobre el plano I constante. Para simplificar la figura, se considera exclusivamente la zona 2, si bien podría realizarse análogamente para las restantes zonas centrales. En un diagrama polar (figura 7), se representan los componentes H (angular) y S (radial) de cada píxel perteneciente a la zona 2 de todas las imágenes de la serie. Para un determinado grado, se han representado todos los píxeles de la zona 2,

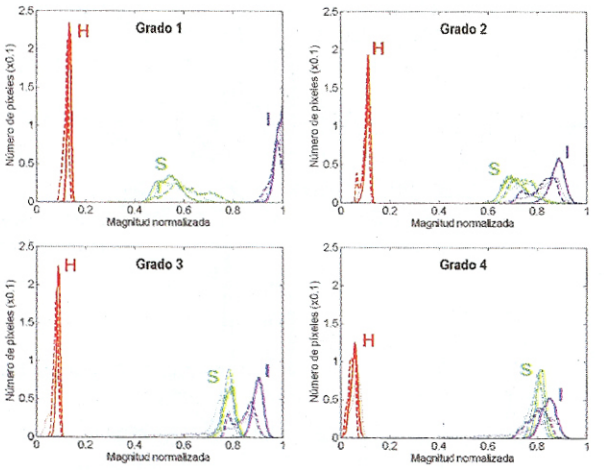

Figura 6.- Histogramas normalizados de las componentes HSI de las regiones 1 (línea punteada), 2 (línea continua) y 3 (línea discontinua) de las imágenes CCLRU (fig. 1).

agrupados en una nube de puntos, en la que el punto en forma de rombo representa los valores medios de H y S para esa nube de puntos. En la figura 7, para facilitar la comprensión de los resultados representados, el fondo del diagrama polar muestra de manera suavizada la distribución aproximada de colores del cuadrante del plano HS considerado. A medida que pasamos del grado 1 al grado 4 sobre la figura 7, se observa que la nube de puntos se desplaza de dos maneras: rota hacia valores bajos del tono (color rojo) y se traslada hacia valores más altos de la saturación. Esta representación permite clarificar y distinguir mejor los diferentes grados en la evolución del contenido de color de las imágenes de la serie que la figura 6. Por ello, la representación de la figura 7 es una representación de gran utilidad en la evaluación objetiva del grado de hiperemia de la conjuntiva tarsal superior.

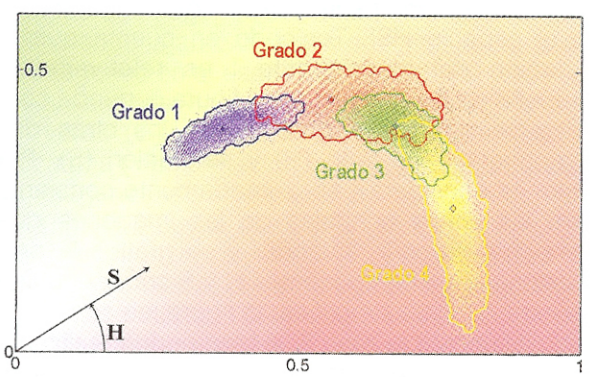

Figura 7.- Diagrama polar HS de los píxeles de la zona 2 de las imágenes CCLRU (fig. 1). Cada grado se representa por una nube de puntos. El punto señalado con un rombo indica los valores medios de H y S. El fondo del diagrama muestra, de manera aproximada y suavizada, la distribución de colores en la región del plano cromático representado.

Si se dispusiese de la información neçesaria sobre la distribución espectral del iluminante, la caracterización de la cámara, y se fijasen condiciones estándar de iluminación, se podrían obtener imágenes colorimétricas. En ese caso propondríamos transformar los valores de los píxeles de las imágenes, del espacio RGB dependiente del dispositivo de captación, a coordenadas CIELAB, siguiendo una práctica generalizada en el tratamiento colorimétrico de las imágenes en color. En tal caso, y admitiendo la condición de intensidad casi constante (o, equivalentemente, coordenada L* ~ constante), se utilizaría la proyección de valores *L*a*b** sobre el plano de cromaticidad *a*b**. Las medidas de las nubes de puntos proyectadas se utilizarían para evaluar la gravedad de la hiperemia de la conjuntiva tarsal superior de modo análogo a como se ha realizado en la figura 7.

CONCLUSIONES

En este trabajo se han estudiado los parámetros sobre los que se puede realizar una evaluación objetiva de la hiperemia de la conjuntiva tarsal superior a partir de un análisis de imagen del párpado evertido. Para extraer los parámetros significativos y estudiar su variación con el grado de gravedad del problema, se han analizado las imágenes de la escala estándar CCLRU.

Se ha propuesto aplicar un pre-procesado de las imágenes, consistente en una transformación geométrica, para asegurar que se comparan áreas equivalentes de la región de interés. Se ha centrado el estudio en las regiones centrales 1, 2 y 3 definidas por la carta CCLRU para este tipo de problema ocular. La estadística de las componentes G y B, concretamente el valor medio del histograma G y la desviación estándar del histograma B, son útiles para representar la evolución de la hiperemia y se pueden utilizar en la estimación objetiva del grado. Tras convertir las imágenes RGB al espacio HSI, la representación de los valores H y S en un diagrama polar permite visualizar la evolución de la hiperemia en la serie de imágenes y puede utilizarse también para la evaluación objetiva de su gravedad.

Finalmente, el estudio realizado permite poner de manifiesto la conveniencia de disponer de nue-

vas series de imágenes estándar, captadas en condiciones colorimétricas bien controladas, mediante dispositivos calibrados y con esta información disponible para un análisis de imagen más amplio y preciso.

AGRADECIMIENTOS

Los autores agradecen la colaboración de los profesores Carme Serés, Lluïsa Quevedo y Genís Cardona, del Departamento de Óptica y Optometría de la Universitat Politècnica de Catalunya. Agradecen asímismo la financiación del Ministerio de Educación y Ciencia y FEDER (proyecto DPI2003-03931) y de la Generalitat de Catalunya (proyecto 2003XT-00081).

BIBLIOGRAFÍA

1. McMonnies CW, Chapman-Davies A. Assessment of conjunctival hyperemia in contact lens wearers. Part I. Am J Optom Physiol Optics 1987; 64: 246-250.
2. Terry RL, Schnider CM, Holden BA, Cornish R, Gran T, Sweeney D, et al. CCLRU standards for success of daily and extended wear contact lenses. Optom Vis Sci 1993; 70: 234-243.
3. Efron N. Grading scales for contact lens complications. Ophthal Physiol Opt 1998; 18: 182-186.
4. Villumsen J, Ringquist J, Alm A. Image analysis of conjunctival hyperemia. Acta Ophthalmologica 1991; 69: 536-539.
5. Willingham FF, Cohen KL, Coggins JM, Tripoli NK, Ogle JW, Goldstein GM. Automatic quantitative measurement of ocular hyperemia. Current Eye Res 1995; 14: 1101-1108.
6. Guillon M, Shah D. Objective measurements of contact lens-induced conjunctival redness. Optom Vis Sci 1996; 73: 595-605.
7. Owen CG, Fitzke FW, Woodward EG. A new computer assisted objective method for quantifying vascular changes of the bulbar conjunctivae. Ophthal Physiol Opt 1996; 16: 430-437.
8. Pérez-Cabré E, Millán MS, Abril HC, Otxoa E. Image processing of standard grading scales for objective assessment of contact lens wear complications. Proc SPIE 2004; 5622: 107-112.
9. Wolffsohn JS, Purslow C. Clinical monitoring of ocular physiology using digital image analysis. Contact Lens Ant Eye 2003; 26: 27-35.
10. http://www.cclru.org/eye_information/grading_scales/DATA/front_page.htm
11. Pratt WK. Digital Image Processing. 2nd edition, Wiley. New York, 1991.
12. González RC, Woods RE, Eddins SL. Digital image processing using MATLAB. Pearson-Prentice Hall. New Jersey, 2004.

Image analysis of contact lens grading scales for objective grade assignment of ocular complications

Opto-Ireland 2005: Photonic Engineering, Proc. SPIE **5827**,
ISBN: 0-8194-5812-0, Bowe, B. W., Byrne, G., Flanagan, A. J., Glynn, T. J.,
Magee, J., O'Connor, G. M., O'Dowd, R. F., O'Sullivan, G. D., Sheridan, J. T. ed.,
418-427, Dublin, Irlanda, 2005.

Image analysis of contact lens grading scales for objective grade assignment of ocular complications

Elisabet Pérez-Cabré, María S. Millán, Héctor C. Abril, Edison Valencia

Optics & Optometry Dept., Technical University of Catalonia, Violinista Vellsolà, 37, 08222 Terrassa (Spain). Email: eperez@oo.upc.edu

ABSTRACT

Ocular complications in contact lens wearers are usually graded by specialists using visual inspection and comparing with a standard reference. The standard grading scales consist of either a set of illustrations or photographs ordered from a normal situation to a severe complication. Usually, visual inspection based on comparison with standards yields results that may differ from one specialist to another due to contour conditions or personal appreciation, causing a lack of objectiveness in the assessment of an ocular disorder.

We aim to develop a method for an objective assessment of two contact lens wear complications: conjunctiva hyperemia and papillary conjunctivitis. In this work, we start by applying different image processing techniques to two standard grading scales (Efron and *Cornea and Contact Lens Research Unit*-CCLRU grading scales). Given a set of standard illustrations or pictures, image pre-processing is needed to compare equivalent areas. Histogram analysis allows segmenting vessel and background pixel populations, which are used to determine features, such as total area of vessels and vessel length, in the measurement of contact lens effects.

In some cases, the colour content of standard series can be crucial to obtain a correct assessment. Thus, colour image analysis techniques are used to extract the most relevant features. The procedure to obtain an automatic grading method by digital image analysis of standard grading scales is described.

Keywords: Biomedical image, Image analysis, Objective assessment, Ocular redness, Contact lens standard grading scales.

1. INTRODUCTION

Inadequate wearing of contact lenses gives rise to ocular complications that need to be assessed by specialists. So far, the most common assessment is based on a visual comparison of the affected eye with standard scaled series of illustrations or photographs.[1-3] Visual inspection based on comparison with standards, either illustrations or photographs, yields results that may differ from one specialist to another due to contour conditions or personal appreciation, causing a lack of objectiveness in the assessment of an ocular disorder. Available standards are difficult to compare between them because the grading scales corresponding to a given effect may not coincide neither in the number of degrees nor in the area of the eye under evaluation, among other reasons. An attempt to overcome these difficulties was made by Nathan Efron.[3] He recommended the use of a set of illustrations instead of still images in order to keep constant some factors (field of view, magnification, etc), to avoid potentially confounding artifacts, and, what is even more important, to depict the effects of one single complication in the illustrations.

Some proposals to objectively quantify ocular hyperemia from image analysis have been introduced in the literature.[4-8] So far, most of the studies (on conjunctiva hyperemia) concentrate their efforts on applying image processing techniques to grey level or binary images. In general, they try to evaluate blood vessel pixel population to compute the area occupied by vessels, assuming that the level of redness is proportional to the presence of vessels. Standard image enhancement techniques were applied by Villumsen *et al.*[4] to increase vessel border contrast so that a threshold value could be easily chosen to binarize an image. Afterwards, a point counting technique was used to estimate the degree of hyperemia. Willingham *et al.*[5] analyzed McMonnies standard[1] along with real images. In their paper, pixels from a group of test images were hand labeled according to the known vessel and non-vessel areas. Guillon and Shah[6] proposed

Opto-Ireland 2005: Photonic Engineering, edited by B. W. Bowe, G. Byrne, A. J. Flanagan, T. J. Glynn, J. Magee, G. M. O'Connor, R. F. O'Dowd, G. D. O'Sullivan, J. T. Sheridan, Proc. of SPIE Vol. 5827 (SPIE, Bellingham, WA, 2005) · 0277-786X/05/$15 · doi: 10.1117/12.610226

a semiautomatic method to detect blood vessels along a set of sampling lines distributed over the limbal and bulbar conjunctiva. They applied their method to real images. Finally, Owen *et al.*[7] also used images captured from real patients and measured the percentage of vessel area after binarizing a monochrome image of the eye. As it was stated in the paper, threshold selection was of critical importance to appropriately determine the degree of vascular representation. Assessment results for different threshold values allowed them to choose the most suitable threshold.

Our aim is to analyze the set of illustrations (Fig. 1a) and photographs (Fig 1b) displaying the conjunctival hyperemia effects by two different standards (Efron and CCLRU grading scales). Another effect, known as papillary conjunctivitis, will be analyzed from the corresponding set of photographs of CCLRU standard (Fig. 1c). This study will permit us to extract the most relevant features for these ocular disorders. Feature extraction and evaluation should allow us to build a model of the visual assessment and establish an objective grading method based on digital image processing. Vessel segmentation from conjunctiva and palpebral background will be achieved by a computer-based procedure. Threshold determination will be based on the probability of pixel misclassification. Vessel area and color information, among other features, will provide information about the degree of severity of the ocular complications.

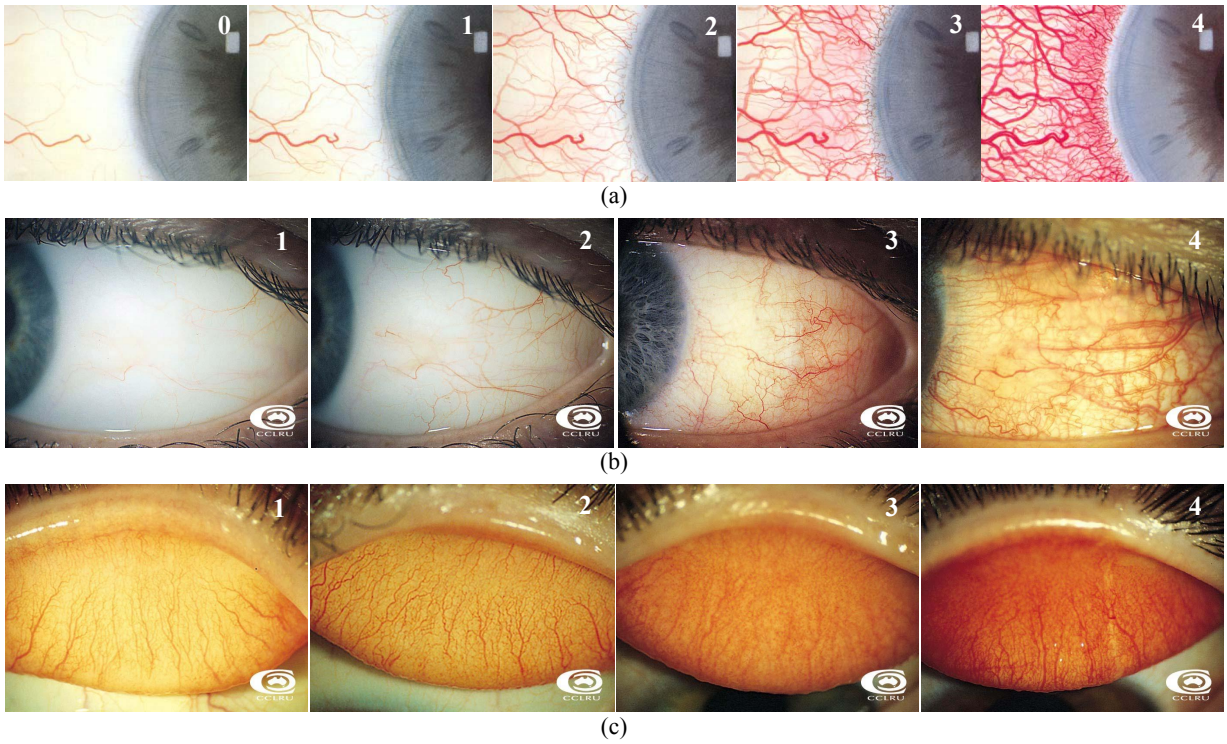

Fig. 1. Standard grading scales. (a) Efron illustrations and (b) CCLRU photographs for conjunctival hyperemia, (c) CCLRU photographs for papillary conjunctivitis.

2. IMAGE PREPROCESSING

Accurate monitoring of the evolution of an ocular complication by using standard grading scales assumes that the feature extraction and evaluation has to be carried out over a similar area imaged under comparable conditions. As it can be seen in Fig. 1, none of the illustrations or photographs belonging to any standard meets this requirement and, consequently, they can not be compared straightforwardly.

For CCLRU photographs differences between pictures belonging to the same grading scale are evident. They do not all possibly correspond to the same patient, and they have been taken under different experimental conditions. Illumination

is not uniform over the whole area depicted in the photograph and the area is not the same in all the pictures. Slight defocusing can be noticed in some images of the set. Provided that we want to obtain an objective measure of the complication evolution, some image preprocessing must be carried out to assure similar feature analysis over the whole set of standard pictures.

Firstly, to ensure that a similar area is analyzed along the different photographs of a given set, a polynomial transformation is applied to pictures of the CCLRU standard. Photographs are adjusted so that the conjunctiva contour or the palpebral edges match those of the pictures corresponding to degree 2 (Fig. 1b and 1c). Fig. 2 displays two examples of the polynomial transformation applied to CCLRU images corresponding to grade 4 for conjunctiva hyperemia and to grade 1 for papillary conjunctivitis, respectively.

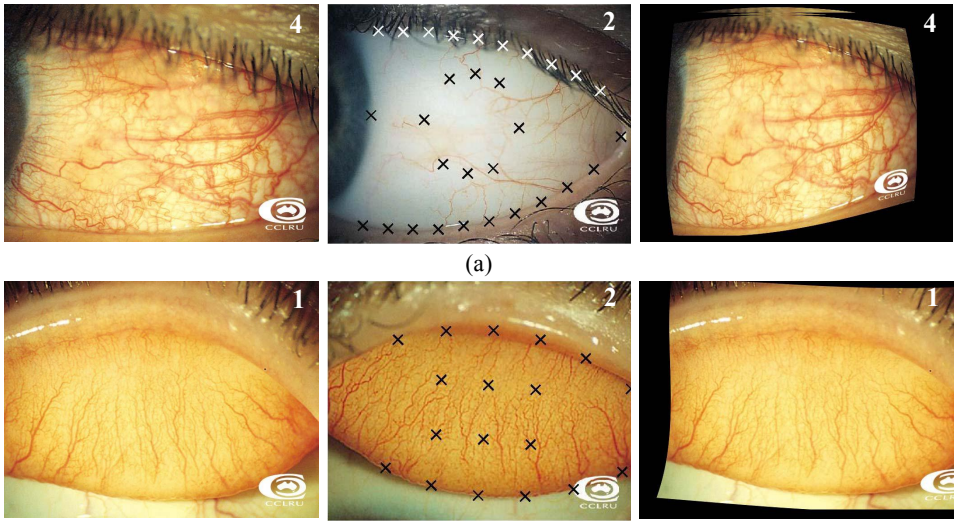

Fig. 2. Example of the polynomial transformation applied to the standard CCLRU photographs to match the contour depicted in the pictures of grade 2 for (a) conjunctiva hyperemia (grade 4) and (b) papillary conjunctivitis (grade 1).

Secondly, it is necessary to determine the region of interest (ROI) where the effects of a contact lens wear complication should be evaluated. Fig. 3 shows the ROI for conjunctiva hyperemia in the case of Efron illustrations (Fig. 3a) and in the case of CCLRU pictures (Fig. 3b). These regions have been chosen by taking into consideration a specialist opinion, and in accordance to the procedure followed by Owen *et al.*[7] Palpebral conjunctiva is divided into five areas to grade redness and roughness (Fig. 3c). According to CCLRU standards, areas 1, 2 and 3 are the most relevant in contact lens wear to evaluate lid redness.

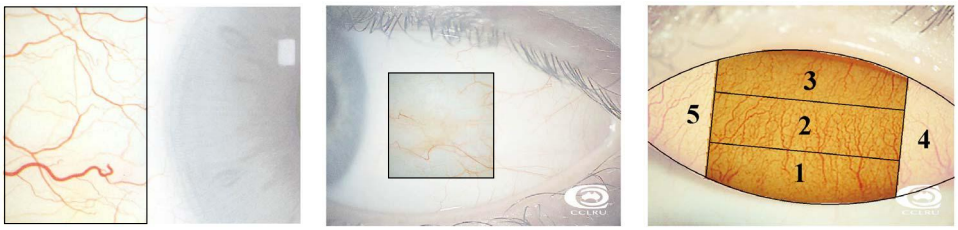

(a) (b) (c)

Fig. 3. Regions of interest (ROI) for ocular effect assessment, in the cases of (a) Efron illustration of conjunctiva hyperemia (grade 2), CCLRU photographs of (b) conjunctiva hyperemia (grade 2), and (c) papillary conjunctivitis (grade 2).

Apart from the polynomial transformation, which was not necessary to apply to the Efron standard, preprocessing of images follows the same steps in both cases, illustrations and still images. A diagram describing the preprocessing steps is shown in Fig. 4. First of all, a ROI selection is carried out from either the original illustration or the transformed photograph. An RGB decomposition is considered to choose the channel with the highest inverted contrast. A morphological operation, called Top-Hat, makes the background energy low and uniform.

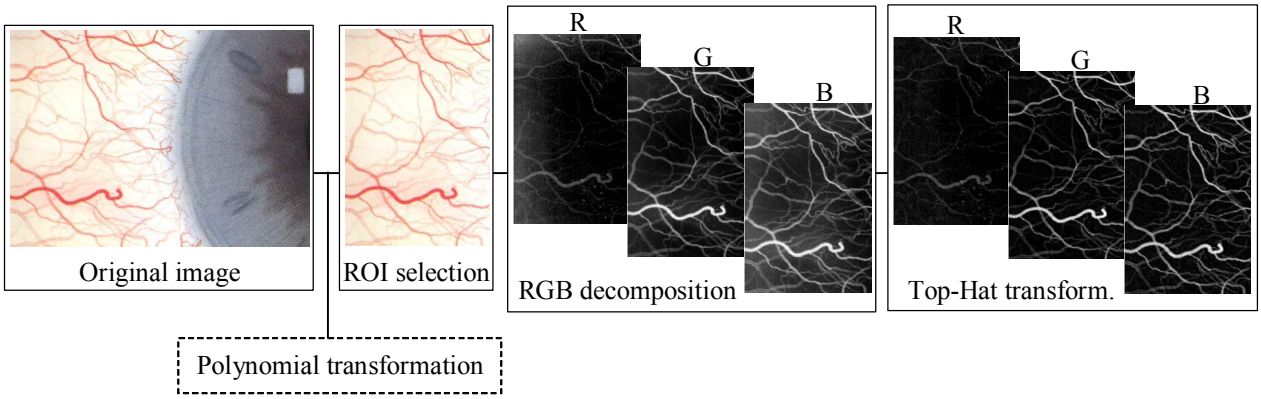

Fig. 4. Diagram of the image preprocessing step. RGB components are displayed as negative images.

3. VESSEL SEGMENTATION FROM BACKGROUND

Once the standard images are preprocessed, the second step consists of segmenting vessel pixel population from the bulbar or palpebral background. A single chromatic channel is chosen to carry out this step. The channel that keeps the vessel information with the highest contrast is selected to determine the image pixels belonging to vessels. Our choice is channel B for conjunctiva hyperemia and channel G for papillary conjunctivitis.

Vessel segmentation can be automatically achieved following the sequence of steps displayed in Fig. 5. First, the histogram of the selected channel is computed. We assume that the background distribution tends to follow a gaussian profile, while the possible asymmetries of the histogram are mainly due to vessel contribution. A criterion of equal probability of misclassification error of vessel and background pixels is considered to establish the threshold level for image binarization. Noise is reduced by applying a size-based threshold on the skeleton of the binary image.

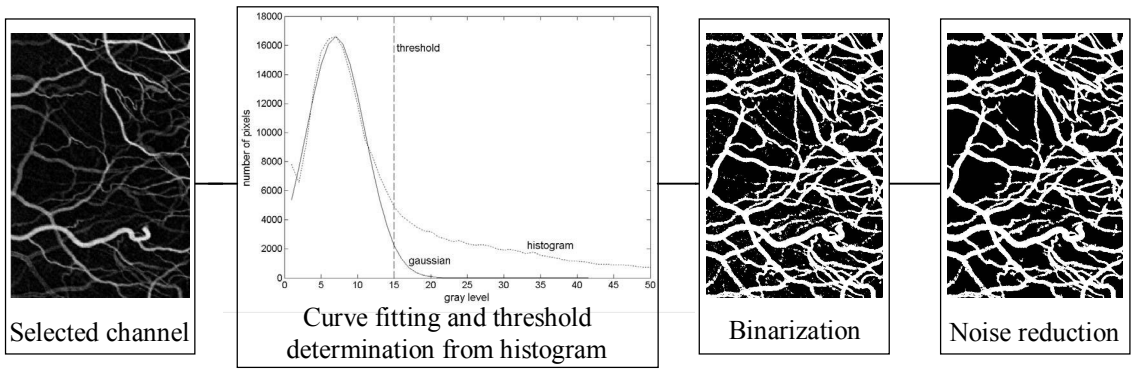

Fig. 5. Diagram for vessel (object) to bulbar background segmentation.

4. FEATURE EXTRACTION

From the noise-reduced binary images of the standards (Fig. 6), the extraction and evaluation of features that best describe the ocular complications is aimed. Conjunctiva hyperemia is analyzed using different parameters, such as percentage of the area occupied by vessels, number of nodes (intersections between vessels) and distribution of vessel segment lengths.

Nodes are detected by following the procedure described by Lin and Zheng.[9] Node location allows us to study segment length variations. The results obtained from the Efron and CCLRU standards will be compared.

For the case of papillary conjunctivitis, the color content of these images appears to be crucial information in order to obtain a correct assessment. Thus, lid redness evolution could be monitored from grade 1 to grade 4 of the CCLRU grading scale by analyzing the color information for both vessel and background pixel populations.

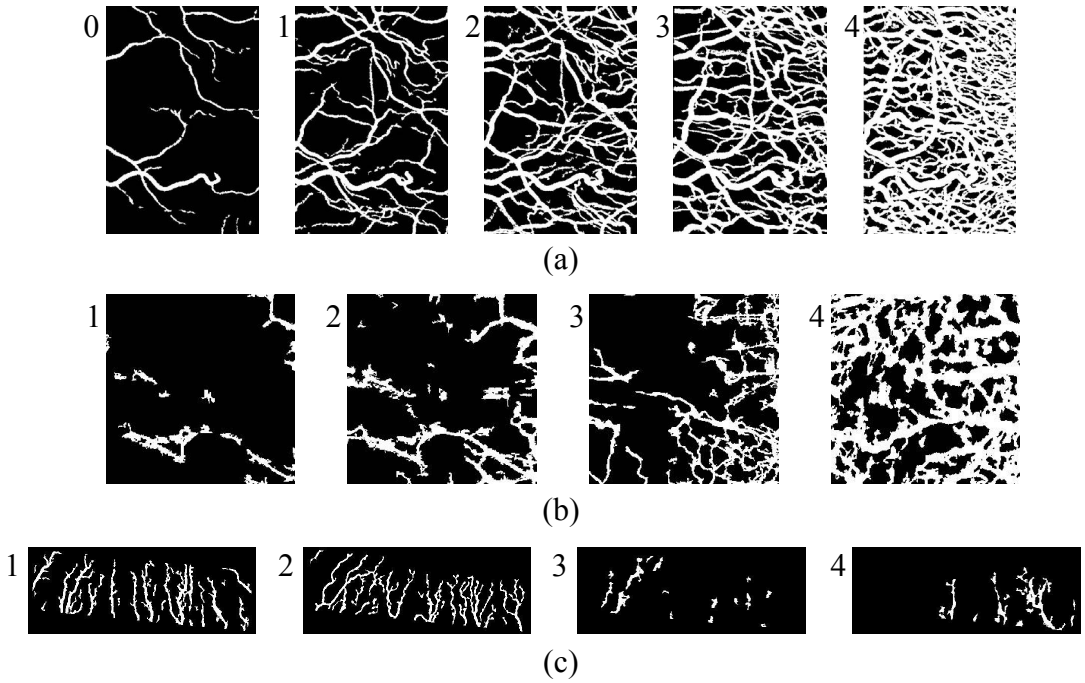

Fig. 6. Noise-reduced binary images of selected ROI for (a) Efron and (b) CCLRU standards describing conjunctiva hyperemia, (c) CCLRU photographs (zone 2) for papillary conjunctivitis.

5. RESULTS

1. Conjunctiva hyperemia

1.1. Efron grading scale (illustrations)

Fig. 7 includes three graphs representing, respectively, the area occupied by vessels, the number of nodes and the distributions of vessel segment lengths. From these plots, both the area in percentage and the number of nodes increase with the severity of ocular hyperemia. The higher degree of this contact lens effect, the larger number of vessels is presented. Number of nodes also increases with the degree of the complication, but at the same time, the vessel length between intersections shortens significantly.

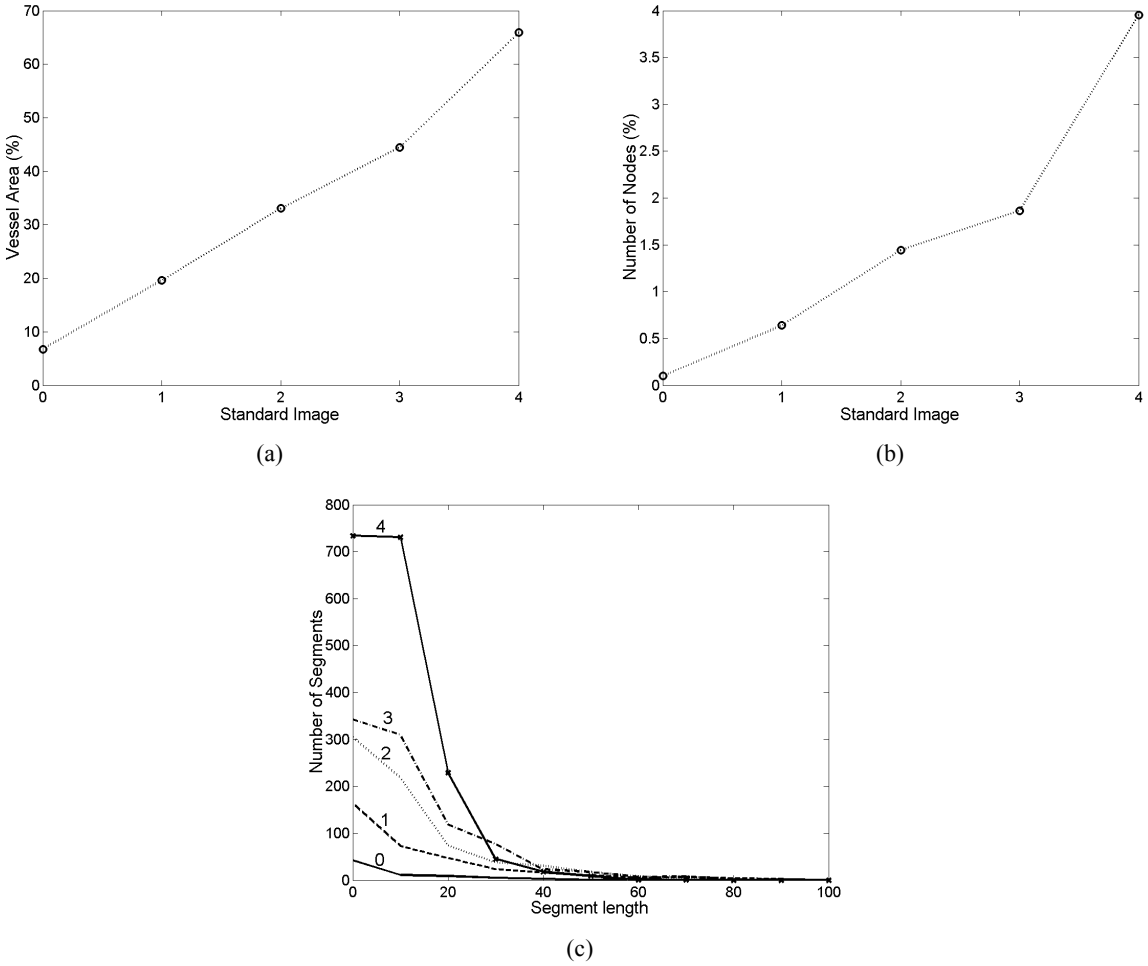

Fig. 7. Feature evaluation for illustrations of conjunctiva hyperemia from Efron grading scale. (a) Vessel area in percentage, (b) Number of nodes in percentage and (c) distributions of vessel segment lengths.

1.2. CCLRU grading scale (photographs)

The same features are evaluated for the four photographs of the CCLRU standard. The results are plotted in Fig. 8. There is an increase of the vessel area (Fig. 8a) and the number of nodes (Fig. 8b) when the ocular complication corresponds to a higher degree. The length distribution of vessel segments (Fig. 8c) shows a result similar to that for the Efron illustrations. The higher the grade of the ocular disorder, the larger the number of segments, particularly short segments.

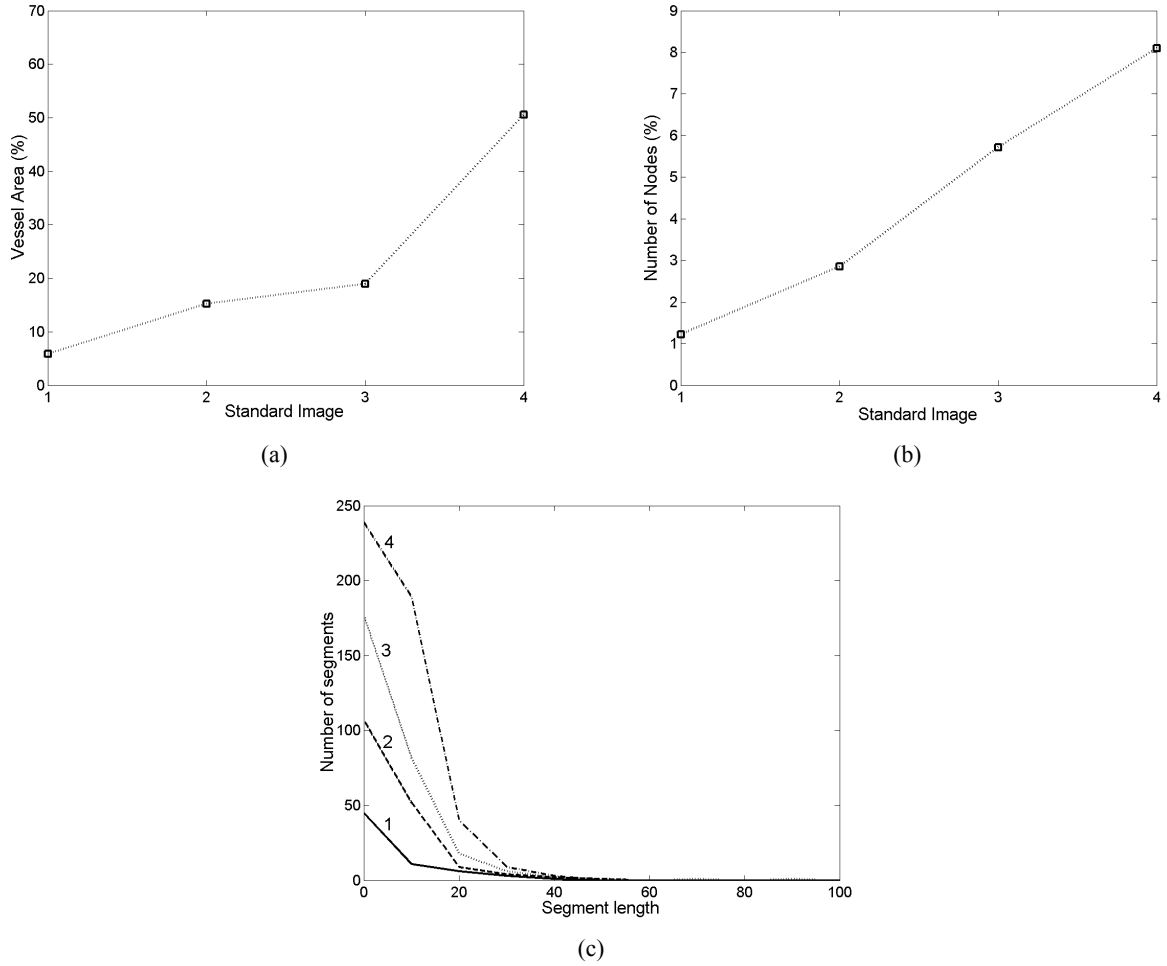

Fig. 8. Feature evaluation for photographs of conjunctiva hyperemia from CCLRU grading scale. (a) Vessel area in percentage, (b) Number of nodes in percentage and (c) distributions of vessel segment lengths.

2. Papillary conjunctivitis

The objective assessment for papillary conjunctivitis (Fig. 1c) is considered in this section. Image preprocessing techniques as well as vessel segmentation from palpebral background are carried out to analyze the CCLRU standard pictures.

Analysis of the RGB components of the color standard images is performed. Fig. 9 depicts the RGB histograms for the zone 2 (Fig. 2c) of each standard image from grade 1 up to 4. The evolution of these histograms permits to monitor the variation of the contact lens wear effect. The most relevant changes in the RGB histograms are the mean value of the green distribution (G histogram), and the standard deviation of the blue distribution (B histogram). Both magnitudes should be taken into account in order to obtain an objective measurement of papillary conjunctivitis. Table 1 contains the mean value of the RGB distributions and their standard deviations. As the degree of this effect increases, the green mean value decreases (the histogram mode shifts to lower grey levels), and the blue standard deviation decreases (the histogram mode drifts to a sharper, narrower curve).

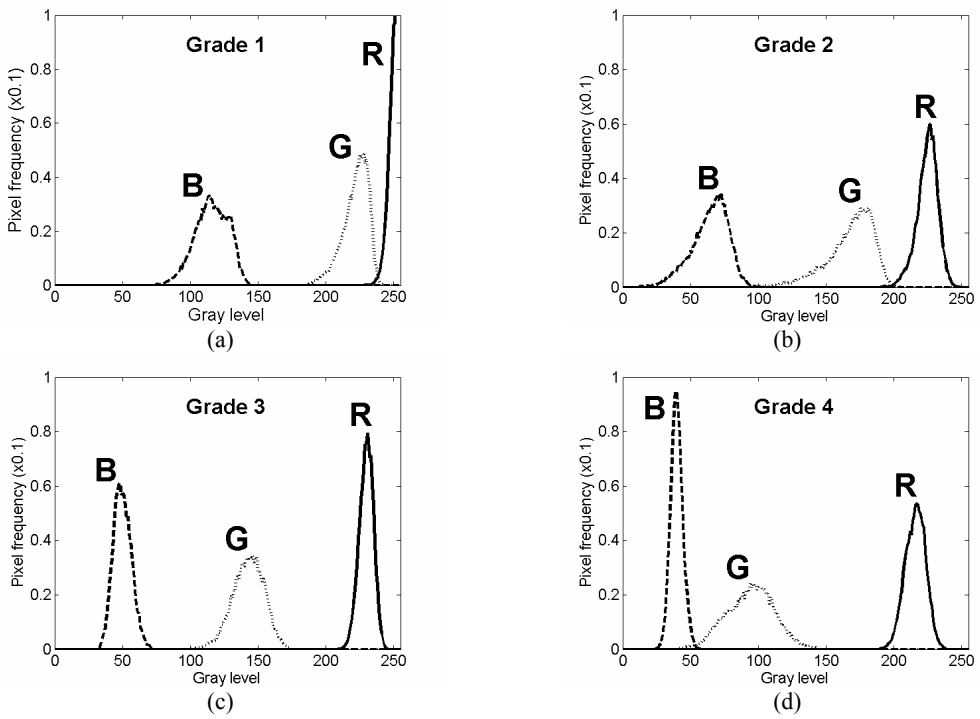

Fig. 9. Normalized histograms of RGB components for CCLRU photographs of papillary conjunctivitis (zone 2).

Table 1. Mean value and standard deviation for the RGB histograms of the 4 grades of papillary conjunctivitis (CCLRU standards) (zone 2).

Mean value	1	2	3	4	Standard deviation	1	2	3	4
R	250.3	224.6	229.7	215.8	R	16.6	234.6	906.3	354.1
G	221.7	167.8	142.7	94.2	G	113.8	577.1	821.6	309.8
B	115.6	64.2	49.9	39.8	B	206.2	286.7	43.6	40.8

The RGB images belonging to the standard series have strong limitations: unavailability of the channel responsivities of the color camera used in the image acquisition, undefined illumination conditions and spectral power distribution of the illumination source. Taking these limitations into account, we convert the RGB images to the HSI color space by applying standard formula in digital image processing.[10] We use this conversion as a tentative approach that will allow us to redistribute the image color content into more perceptually meaningful components.

We represent the hue (H) and saturation (S) components of each pixel belonging to the zone 2 of all the images in a polar diagram (Fig. 10). For a given grade, all the pixels depicted in Fig. 6 appear covering a cloud-shaped area, where the diamond indicates the H and S mean values of the image pixels. As we move from grade 1 up to grade 4 the area also moves in two senses: rotation towards low hue values (red) and shift towards high saturation values.

Some differences can be noticed if two polar diagrams are independently displayed for vessel and background pixel populations (Fig. 11). Fig. 11a corresponds to the polar diagram for pixels of standard images (zone 2) classified as vessels whereas Fig. 11b depicts a similar diagram for pixels corresponding to the background of the eyelid. To make differences clearer between the two graphs, Fig. 11c shows the mean H and S values obtained separately for vessels and backgrounds from grade 1 up to 4.

From Fig. 11, we can observe that vessel pixels have a lower hue, shifting to red, and slightly higher saturation than background pixels of the same picture.

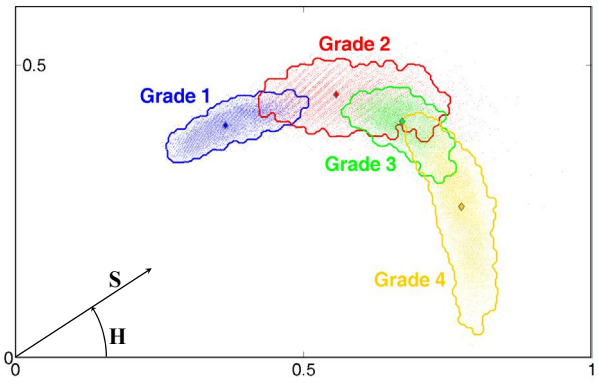

Fig. 10. Polar HS diagram of image pixels (zone 2) of standard series. The diamond indicates the H and S mean values corresponding to each grade.

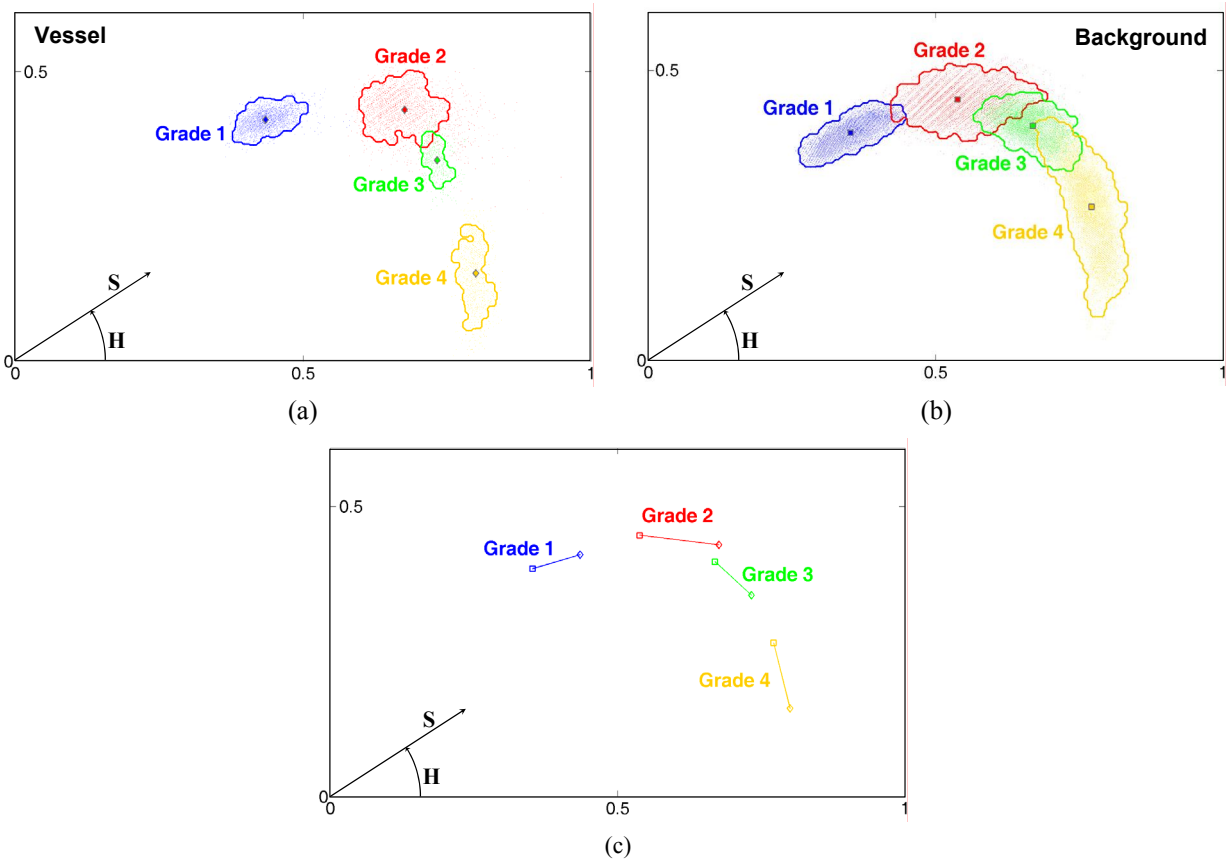

Fig. 11. Polar HS diagram of image pixels (zone 2) of standard series. (a) Diagram for pixels belonging to vessel population. The diamonds indicate the H and S mean values corresponding to each grade. (b) Diagram for pixels corresponding to background population. The squares stand for the H and S mean values obtained for each grade. (c) HS polar diagram of vessel (diamond) and background (square) mean values from grade 1 up to 4.

6. CONCLUSIONS

We have analyzed standard image series of two ocular complications produced by inadequate lens wearing. Pre-processing of the standard images is carried out to assure feature comparison over a similar area (region of interest) with uniform illumination.

The analysis of the conjunctiva hyperemia images that compose the Efron illustration and CCLRU picture standard grading scales has allowed us to extract several features for an objective and automatic assessment. These features are the area of vessels, the number of nodes and the distribution of vessel segment lengths. Although the images of both standards are very different, the results show that they are in good agreement with respect to the features extracted.

Papillary conjunctivitis images of the CCLRU grading scale have been analyzed on the basis of their RGB histogram and the way they vary from the lowest to the most severe degree. The G mean value and the B standard deviation appear to be two good features for grading this disorder. Having been converted from RGB images into HSI images, the distribution of the H and S pixel values of the different images gives relevant information for an objective assessment of the effect severity. Color differences are noticeable for vessel and background pixel populations.

ACKNOWLEDGMENTS

Authors thank the Ministerio de Educación y Ciencia, FEDER (project DPI2003-03931) and the Generalitat of Catalunya (project 2003XT-00081) for financial support.

REFERENCES

1. C. W. McMonnies, *et al.*, "The vascular response to contact lens wear", Am. J. of Optometry & Physiological Optics, **59**, 795-799, 1982.
2. R. L. Terry, *et al.*, "CCLRU standards for success of daily and extended wear contact lenses", Optometry & Vision Science, **70**, 234-243, 1993.
3. N. Efron, "Grading scales for contact lens complications" Ophthal. Physiol. Opt., **18**, 182-186, 1998.
4. J. Villumsen, J. Ringquist, A. Alm, "Image analysis of conjunctival hyperemia", Acta Ophthalmologica, **69**, 536-539, 1991.
5. F. F. Willingham, *et al.*, "Automatic quantitative measurement of ocular hyperemia", Current Eye Research, **14**, 1101-1108, 1995.
6. M. Guillon, D. Shah, "Objective measurements of contact lens-induced conjunctival redness", Optometry & Vision Science, **73**, 595-605, 1996.
7. C. G. Owen *et al.*, "A new computer assisted objective method for quantifying vascular changes of the bulbar conjunctivae", Ophthal. Physiol. Opt., **16**, 430-437, 1996.
8. E. Pérez-Cabré, M. S. Millán, H. C. Abril, E. Otxoa, "Image processing of standard grading scales for objective assessment of contact lens wear complications", Proc. SPIE, **5622**, 107-112, 2004.
9. T. Lin, Y. Zheng, "Node-matching-based pattern recognition method for retinal blood vessel images", Opt. Eng., **42**, 3302-3306, 2003.
10. R. C. Gonzalez, R. E. Woods, S. L. Eddins, "Digital image processing using MATLAB", Pearson-Prentice Hall, Upper Saddle River, NJ, 2004.

Cup to disc ratio of the optic disc by image analysis to assist diagnosis of glaucoma risk and evolution

5th. International Workshop on Information Optics, AIP **CP860**,
ISBN: 978-0-7354-0356-7, Cristóbal, G., Javidi, B., Vallmitjama, S. ed.,
290-299, Toledo, España, 2006.

Cup-To-Disc Ratio Of The Optic Disc By Image Analysis To Assist Diagnosis Of Glaucoma Risk And Evolution

Edison Valencia*, María S. Millán*, and Rafal Kotynski†

*Department of Optics and Optometry, Technical University of Catalonia
C/ Violinista Vellsolà, 37, 08222 Terrassa, Spain. edison@oo.upc.edu, millan@oo.upc.edu
†Instytut Geofizyki, Uniwersytet Warszawski
ul. Pasteura 7, 02-093 Warszawa, Poland

Abstract. This work builds an image analysis algorithm to give assistance in the cup to disc ratio estimation of glaucomatous eyes. Often the contours of both the optic cup and disc are faint and intersected by entangled veins that make it difficult to draw their silhouettes. The algorithm, which takes into account the viewing conditions of the specialist, is based on the information of color, the color differences between neighbor pixels and the geometry of the areas involved.

Keywords: Retinal image, color, color difference, S-CIELAB, segmentation, cup-to-disc ratio.
PACS: 87.57.-s; 87.57.Nk; 87.57.Ra; 42.66.Ne.

INTRODUCTION

The optic disc (optic nerve head) is the entrance region of blood vessels and optic nerves to retina (Figure 1(a)). The examination of the optical disc appearance in retina fundus images is a general practice of ophthalmologists to evaluate the potential risk of glaucoma or to monitor the evolution of glaucomatous eyes. Reductions of the neuroretinal rim may reveal the pathological damage. A common parameter to assess the severity of the damage is the cup-to-disc ratio [1], which gives an idea of the area occupied by the cup in the optic disc. This ratio is useful to evaluate the nerve fiber loss and the structural damage. These symptoms usually come before the detectable alterations in the field of view [2].

In the last years there is an increasing interest to obtain an objective estimation of the cup-to-disc ratio from the analysis of the digital retina images provided by a variety of improved and sophisticated instruments of the ophthalmologic clinic. Greaney et al. [3] used optic nerve head stereophotographs (ONHPs), confocal scanning laser ophthalmoscopy (CSLO), scanning laser polarimetry (SLP), and optical coherence tomography (OCT) to measure different characteristics of glaucomatous optic nerve damage with the goal of diagnosing early to moderate glaucoma in the same population sample. The authors concluded that the quantitative methods CSLO, SLP and OCT were no better than qualitative assessment of disc ONHPs by experienced observers. However, this capability could significantly be improved by a combination of the imaging methods.

CP860, *Information Optics: 5th International Workshop,*
edited by G. Cristóbal, B. Javidi, and S. Vallmitjana

Li and Chutatape [4,5], used principal component analysis and proposed a modified active shape model to detect the disc boundaries in retinal images. They built a point distribution model from a training set and applied an iterative searching procedure to locate instance of such shapes (represented by the position of *n* landmark points) in a new image. Walter et al. [6] have detected the optic disc by means of morphological filtering techniques and the watershed transformation. Pinz et al. [7] presented a prototype software system for automatic map generation of retina. They apply a circular shape approach for the optic disc and used a two-stage gradient-based Hough transform. Zana and Klein [8] present an interesting algorithm based on mathematical morphology and curvature evaluation for the detection of vessel-like patterns in a noisy environment and applied it to the analysis of a variety of retinal images. A method for automated blood vessel detection in the optic disc area that takes into account the axial specular reflection of vessels is described by Vermeer et al. [9].

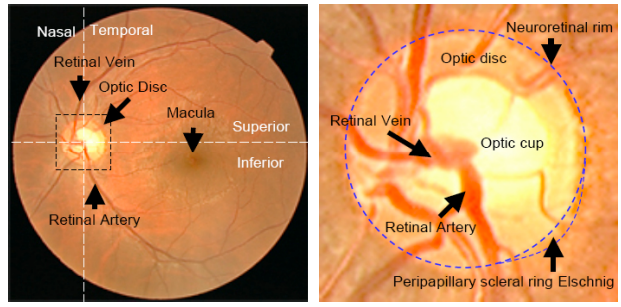

(a) *(b)*

FIGURE 1. (a) Retinal image and (b) optic disc (region of interest).

Although the development of automatic retinal image analysis to assist diagnostic systems has attracted the interests of many researchers, there are difficulties mainly due to noise, uneven illumination and great variation between individuals. The combination of several images of the same eye fundus acquired by different instruments and techniques contributes to improved results. But, on the other hand, the extensive testing to create such combination is expensive, cumbersome and too time consuming to be clinically practical. An automated or semiautomated computer-assisted mass screening for diagnosis and monitoring of glaucomatous eyes is the most important task to which image processing can contribute. As main advantages it could bring a diminution of the necessary resources in terms of specialists and a reduction of the examination time. To this end, we consider single images captured by a non-mydriatic retinal camera [10]. This sort of cameras can be handily used by technicians, not necessarily ophthalmologists, thus saving resources of such specialists.

This work aims to build an algorithm to segment the optic cup inside the optic disc, and the optic disc from the rest of the eye fundus image. The algorithm is intended to give assistance in the cup-to-disc ratio estimation. Note that the contours of both the optic cup and disc are faint and intersected by entangled veins that make it difficult to draw their silhouettes. The algorithm is based on the information of color, color differences between neighbor pixels and geometry of the areas involved.

ALGORITHM OF SEGMENTATION

Retinal Imaging

We consider digital color images of the eye fundus obtained using a non-mydriatic retinal camera that incorporates an infrared focusing system and a white-light flash to register eye fundus with no need of paralyzing the iris diaphragm function. Images can be digitized by computer and displayed on a CRT monitor screen, or printed for visualization. In our case, we use the Topcon TRC-NW6S retinal camera that has a 3CCD Sony DXC-990P camera for imaging and a Xenon flash lamp. Retina fundus images of 30º field are digitized in arrays of 768 x 576 pixels size, where the region of interest corresponding to the optic disc area occupies 100 x 100 pixels approximately. This region, with the optic disc in the center, is segmented from the rest of the image (Figure 1(b)). Since RGB values are device dependent, we perform the color transformations based on devices (camera and display) that conform to the standard color space sRGB. The sRGB color space has been characterized by the International Electrotechnical Commission (IEC) [11].

Preprocessing. LoG Sharpening Inspired By Human Vision Models

In general, the regions of interest of the input images need some preprocessing before applying the algorithm of segmentation. This preprocessing is basically noise smoothing and edge sharpening and it should enhance faint edges without increasing noise. To this end, we apply our recently proposed method for color image sharpening [12] based on the S-CIELAB extension [13]. S-CIELAB involves a series of smoothing spatial filters in the opponent color space that approximate the contrast sensitivity functions of the human vision system. The spatial filters are linear combinations of Gaussian masks. S-CIELAB has been demonstrated to be useful and more realistic than conventional schemes in measuring the color differences between two digital images because it takes into consideration the viewing conditions of the image displayed on a monitor (viewing distance, pixels per inch or ppi). Our method of color image sharpening is a compact combination of S-CIELAB with derivative edge detectors in the opponent color space that considers human vision models and viewing conditions. First, the input images are linearly transformed from the standard color space sRGB to the device independent color representation CIEXYZ and then, to the opponent color space. We combine the spatial filters of the S-CIELAB extension with the Laplacian operator in each opponent channel to obtain the sharpened image. The Laplacian of the smoothed components is simplified by introducing the Laplacian of Gaussian (LoG) operator. The resulting image is subtracted from the original in each opponent channel and then back transformed to the device independent representation space (XYZ) and to sRGB to obtain the final sharpened image. This final image is intended to be displayed on a given monitor to be seen from a given distance by the specialist (with *d* pixels/degree of visual angle). Mathematically, the sharpened image *ShI* to display can be described by the expression

$$ShI_i(x,y) = I_i(x,y) - kLoG\{F_{di}\} * I_i(x,y), \tag{1}$$

where *I(x,y)* is the region of interest of the input image, *i*={0,1,2} represents the opponent color channel {0=A, achromatic; 1=C_1, red-green; 2=C_2, blue-yellow}, parameter *k* controls the sharpening depth, $LoG\{F_{di}\}$ is the Laplacian of Gaussian operator that involves the Gaussian functions of the weighted linear combinations of the spatial filters F_{di}, which are defined for each channel *i* and viewing conditions *d* [12,13], and finally, symbol * indicates convolution. The viewing conditions specified by *d* can be easily related with the ppi number displayed on the monitor and the viewing distance. When the sharpened image displayed on the monitor is seen at a given distance, a smoothed, spatially filtered version of it is perceived. The perceived sharpened image ShI_d can be obtained from the displayed sharpened image *ShI* by convolving with the spatial filters, according to the expression

$$ShI_{di}(x,y) = F_{di}(x,y) * ShI_i(x,y). \tag{2}$$

To realize of the sharpening effect introduced in Eq. 1, the perceived sharpened image ShI_d should be compared with the original image as is it would be perceived in the same viewing conditions I_d, that is, the smoothed and spatially filtered $I_{di}(x,y) = F_{di}(x,y) * I_i(x,y)$. In this work we assume a sRGB monitor with 100 ppi (39 pixels per cm), a viewing distance of L=19.7 inches (50cm), which corresponds to *d*=35 pixels/degree, and two sharpening depths of *k*=1 and *k*=5. We choose a deeper sharpening to segment the optic disc and a lighter to segment the cup. Figure 2 shows the sharpened image *ShI* that can be obtained after applying Eq. 1 to the region of interest (Figure 1(b)). The smoothed spatially filtered version ShI_d of Figure 2, which simulates what the observer sees in the viewing conditions given by *d*, will be used in the calculations through the paper.

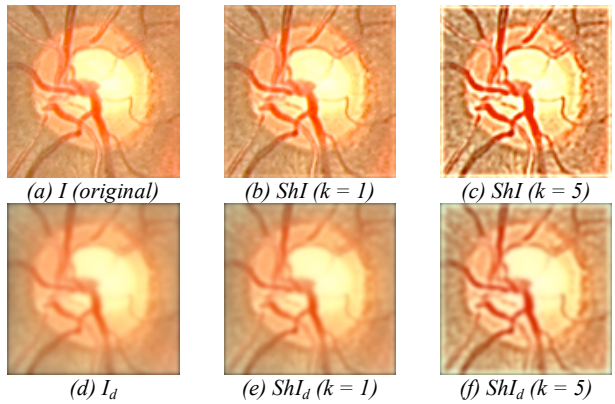

FIGURE 2. (a)-(c) Original and sharpened images as they would be displayed. (d)-(e) Spatially filtered images (as they would be perceived). *L* = 19.7 in., *p* = 100 ppi, and *d*=35 pixels/degree.

Optic Disc

The neuroretinal rim does not appear as a continuous shape with uniform color, but, on the contrary, it is crossed by retinal veins and arteries. For this reason, the algorithm has to approximate the occluded zones of the neuroretinal rim contour. Figure 3 shows a scheme of the process to determine the outer rim contour.

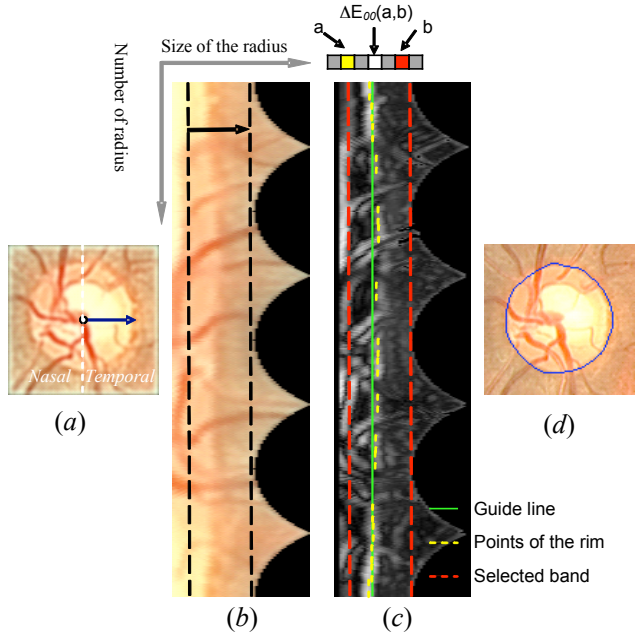

FIGURE 3. Scheme of the algorithm to mark the neuroretinal rim boundary.

From the center of the region of interest, color differences are calculated radially, between neighbor pixels, to find the highest color difference going from the center towards the temporal side (Figure 3(a)). In the standard uniform color space frame of CIELAB, extended to S-CIELAB for color analysis of digital images, we have considered the standard CIEDE2000 color difference formula ΔE_{00}, and related component differences of luminance ΔL, chroma ΔC, and hue Δh [14]. Pixels with the highest color differences ΔE_{00} usually mark points of the rim contour in the temporal side. Taking advantage of the nearly round shape of the optic disc, a new image is generated in polar coordinates (Figure 3(b)). Since the center and the corners of the image in Figure 3(a) are not interesting for our purpose of finding the rim contour, we just pay attention to the band limited by dashed lines in Figure 3(b). The top and bottom rows of this new array correspond to the central part of the temporal side where blood vessels are rare and the contrast between the neuroretinal rim and the rest of the eye fundus appears most sharpened. In the array of Figure 3(b), the contour sought appears close to a right vertical line (not drawn) within the band. This means that a nearly circular geometry for the disc boundary can be assumed in first approach.

The algorithm to segment the disc begins with both extremes of the band, i. e. the top and the bottom rows of the array and looks for the pixel (represented by a white point in the small diagram at the top of Figure 3(c)) whose neighbors *a*, *b*, placed at both sides, several pixels far from it, show the highest color difference $\Delta E_{00}(a,b)$ between them. The maximum difference is estimated to select the initial points (pixels) of the rim contour at the top and bottom rows of the array. These initial points have obviously the same (o nearly the same) position in the top and the bottom rows. We draw an imaginary guide line (in green in Figure 3(c)) along the band that joins both initial points. On the other hand, the color difference $\Delta E_{00}(a,b)$ used to fix the initial points is also considered as to be a reference for selecting subsequent pixels to add to the contour. From the visual perception of a large number of images, we realized that the color difference between the neuroretinal rim and the eye fundus is mainly characterized by noticeable differences in Luminance and Hue, but much lower difference in Chroma. In fact, the next pixels to add to the contour are found among those pixels contained in certain vicinity of the guide line that have some *a*,*b* neighbors in their respective rows whose color difference is close enough to that taken as reference. In this point, not only high $\Delta E_{00}(a,b)$ color differences are sought, but also high differences in Luminance ΔL and Hue ΔH, and low differences in Chroma ΔC. If some pixels of the contour are occluded by a blood vessel (that introduces a big distortion in the local distribution of color), then the algorithm jumps beyond the vessel in the direction of the guide line (Figure 3(c)). Finally, the segments of the contour are linked by interpolation and the neuroretinal rim is completed (Fig 3(d)).

Cup

In general, the area of the optic cup appears very bright inside the optic disc, often near to saturation. This part of the image is usually affected by several sources of noise, variability, and it is difficult to segment even for specialists.

To segment the cup we consider the perceived sharpened image ShI_d with depth of k=1. In this image we cut the region outside the optic disc. Taking the pixel color with the highest value of luminance and minimum chromaticity -usually in the yellowish white region- as a seed (*s*), the color differences $\Delta E_{00}(s, p)$ between this seed color and the color of other pixels (*p*) are calculated within the optic disc. As a general idea the pixels that obtain the smallest color differences from the seed are likely to belong to the cup, but this rough assignation needs to be refined. To this end, we build the image of the color differences from the seed (Figure 4(a)). In this image, each pixel has the value given by $\Delta E_{00}(s, p)$. Pixels with low values of $\Delta E_{00}(s,p)$ are concentrated in the left part of the histogram. We study two possibilities to establish a threshold that may help us to separate the pixels of the cup from the rest of pixels of the optic disc. The histogram of the image of the color differences usually shows a multimodal profile with local maxima and minima (Figure 4(b)). In case of being monomode histogram (with no local maxima) the optic disc is said to have no cup. In case of having two or more modes, we order the maxima in decreasing order starting from the absolute maximum. The local minimum with lowest value existing between the two first maxima (i.e. the absolute maximum and the second maximum) can be a possible good threshold. We call this threshold the local minimum threshold (LM).

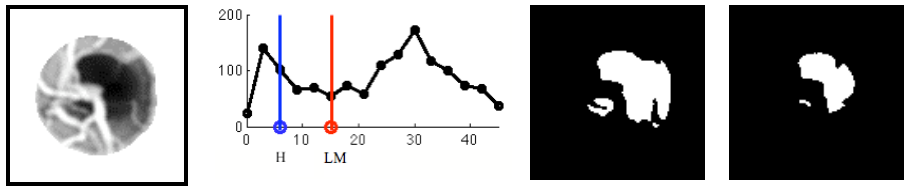

(a) (b) (c) (d)

FIGURE 4. Sequence to segment the cup inside the optic disc: (a) image of the color differences from the seed; (b) histogram with two tentative thresholds: entropy based threshold (H in blue) and local minimum (LM in red); (c) cup determined by highest threshold (LM); (d) cup determined by the lowest threshold (H).

We explore another possibility that takes into account the entropy H [15] as an estimation of the randomness of the various zones of the histogram. The histogram is divided into two sectors 1 and 2 (first level) with 50% of pixels each. We calculate the entropy of each part. Let H_1 and H_2 correspond to the entropies of the histogram sectors with low and high $\Delta E_{00}(s, p)$ values, respectively, and let ε_1 be the ratio of entropies $\varepsilon_1=(H_1/H_2)$. If $\varepsilon_1 > 0.5$, we divide sector 1 into two subsectors, 11 and 12 (second level), with half number of pixels of old sector 1 each, and repeat the estimation of the entropy for each subsector. The procedure is repeated successively and stops when the ratio of entropies of level n satisfies $\varepsilon_n < 0.5$. In such a case, the threshold that divides the former level (n-1) can be taken as a good possibility to separate the pixels of the cup from the rest of pixels of the optic disc. We call it the entropy based threshold (H). The cups segmented by applying both thresholds separately are shown in Figure 4(c,d). The real cup is approximated by these two figures, but it must be taken into consideration that the shape of the cup is close to a round shape in a rough approximation. Let us consider the lowest (most restrictive) threshold. The resultant smallest figure of cup is now framed in a square and the center of the square is determined (Figure 5(a)). From this center we transform again this part of the image in polar coordinates and repeat the procedure already described to determine the optic disc contour. The results are shown in Figure 5 (b) and 5(c).

(a) (b) (c)

FIGURE 5. (a) Cup inside a square, (b) Cup in polar coordinates, (c) Segmented cup (black line) and optic disc (blue line) in the original image.

Feature Extraction

The cup-to-disc ratio is the amount of the entire nerve head that has been cupped out or where glaucoma has caused damage. Readings range from 0 meaning no cupping at all to 1.0 where the entire optic nerve is cupped out (normal eye 0.3 - early glaucoma 0.7- severe glaucoma 0.9). Many people have some cupping, which is normal. Changes in size of the cup-to-disc ratios or a difference between the two eyes lead the eye care specialist to suspect glaucoma.

RESULTS

Figure 6 shows a selection of some original images of the optic disc and their corresponding results after applying the proposed algorithm. A variety of situations concerning dynamic range, noise level, and disc to fundus contrast are shown. A red line segments the cup and the blue line the optic disc. The results are acceptable in general, though the segmentation of the cup needs further improvement in some difficult cases.

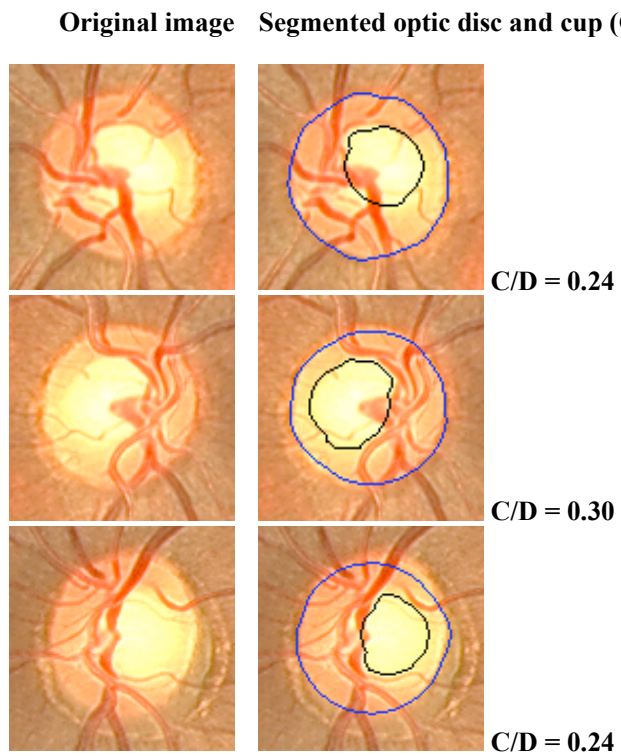

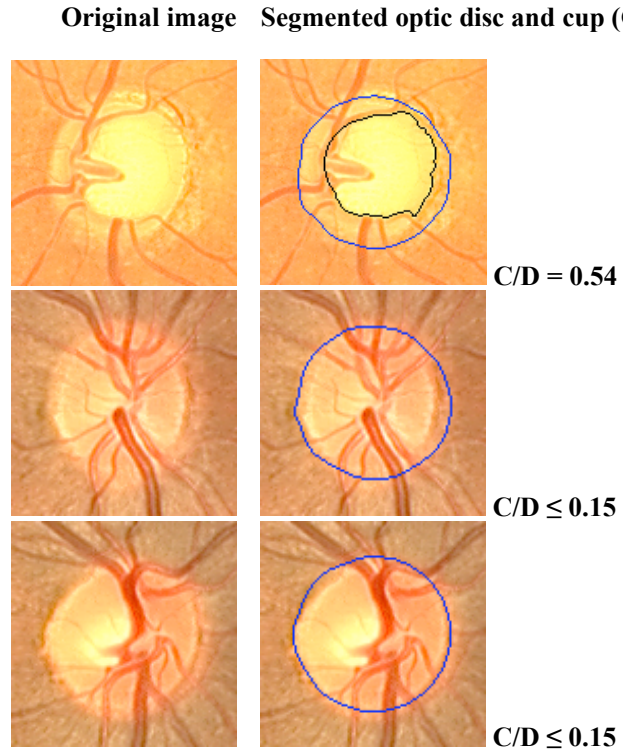

FIGURE 6. Results.

CONCLUSIONS

The algorithms for the automatic segmentation of both cup and disc in the optic nerve head have been developed and applied to a set of real images obtained by using a non-mydriatic retinal camera. They are intended to assist the eye care specialists in the cup-to-disc ratio estimation, which is an important metric for the detection of glaucoma risk. The algorithms are based on the analysis of the color content of the region and the color differences between neighbor pixels. Some considerations about smoothness and round shape of the optic disc boundary have been taken. The method shows a feasible way for complex optic disc image analysis and feature extraction.

ACKNOWLEDGMENTS

The authors acknowledge the financial support of the Spanish Ministerio de Educación y Ciencia and FEDER funds under project DPI2003-03931. We also thank the ophthalmologist Miguel Angel Gil for helping us with the necessary background and for frequent assessments of the results.

REFERENCES

1. M.F. Armaly and R.E. Saydegh, "The cup/disc ratio". *Arch. Ophthalmol.* **82**, 191-196 (1969).
2. A. Sommer, J. Katz, H.A. Quigley, N. R. Miller, A. L. Robin, R.C. Ritcher, and K.A. Witt, "Clinically detectable nerve fiber atrophy precedes the onset of glaucomatous field loss", *Arch. Ophthalmol.* **109**, 77-83 (1991).
3. M. J. Greaney, D. C. Hoffman, D. F. Garway-Heath, M. Nakla, Anne L. Colemna, and Caprioli, "Comparison of Optic Nerve Imaging Methods to Distinguish Normal Eyes from Those with Glaucoma", *Invest. Ophthalmol. Vis. Sci.* **43**, 140-145 (2002).
4. H. Li and O. Chutatape, "Automated Feature Extraction in Color Retinal Images by a Model Besed Approach", *IEEE Transaction on Biomedical Engineering* **51**, 246-254 (2004).
5. H. Li and O. Chutatape, "Boundary detection of optic disk by a modified ASM method", *Pattern Recognition* **36**, 2093-2104 (2003).
6. T. Walter, J. C. Klein, P. Massinm and A. Erginay, "A Contribution of Image Processing to the Diagnosis of Diabetic Retinopathy – Detection of Exudates in Color Fundus Images of the Human Retina", *IEEE Transaction on Medical Imaging* **21**, 1236-1243 (2002).
7. A. Pinz, S. Bernögger, P. Datlinger and A. Kruger, "Mapping the Human Retina", *IEEE Transactions on Medical Imaging* **17**, 606-619 (1998).
8. F. Zana and J. C. Klein, "Segmentation of Vesel-Like Patterns Using Mathematical Morphology and Curvature Evaluation", *IEEE Transactions on Image Processing* **10**, 1010-1019 (2001).
9. K.A. Vermeer, F.M. Vos, H.G. Lemij, A.M. Vossepoel, "A model based method for retinal blood vessel detection", *Computer in Biology and Medicine* **34**, 209-219 (2004).
10. P. J. Saine and M. E. Tyler, *Ophthalmic photography: retinal photography, angiography, and electronic imaging*, 2nd ed., Boston: Butterworth-Heinemann, 2002.
11. IEC 61966-2-1 and "Basic sRGB Math"at http://www.srgb.com/basicsofsrgb.htm (online).
12. M. S. Millán, E. Valencia, "Color image sharpening inspired by human vision models", accepted to be published in Applied Optics (2006).
13. X. Zhang and B. A. Wandell, "A spatial extension to CIELAB for digital color image reproduction," *Soc. for Info. Disp. Symp. Tech. Digest* **27**, 731-734 (1996).
14. G. M. Johnson, M. D. Fairchild, "A top down description of S-CIELAB and CIEDE2000", *Color Res. Appl.* **28**, 425-435 (2003).
15. R. C. Gonzalez, R. E. Woods, and S. L. Eddins, *Digital Image Processing using Matlab*, New Jersey: Pearson Education Inc., 2004.